

UC Berkeley

UC Berkeley Electronic Theses and Dissertations

Title

Thermal Transport and Mechanical Properties of Carbon Nanotube Arrays

Permalink

<https://escholarship.org/uc/item/2mk6g8b6>

Author

Chu, Rong-Shiuan

Publication Date

2012

Peer reviewed|Thesis/dissertation

Thermal Transport and Mechanical Properties of Carbon Nanotube Arrays

by

Rong-Shiuan Chu

A dissertation submitted in partial satisfaction of the

requirements for the degree of

Doctor of Philosophy

in

Applied Science & Technology

in the

Graduate Division

of the

UNIVERSITY OF CALIFORNIA, BERKELEY

Committee in charge:

Professor Arunava Majumdar, Co-Chair

Professor Oscar Dubon, Co-Chair

Professor Costas Grigoropoulos

Professor Liwei Lin

Fall 2012

Thermal Transport and Mechanical Properties of Carbon Nanotube Arrays

Copyright 2012

by

Rong-Shiuan Chu

Abstract

Thermal Transport and Mechanical Properties of Carbon Nanotube Arrays

by

Rong-Shiuan Chu

Doctor of Philosophy in Applied Science & Technology

University of California, Berkeley

Professor Arunava Majumdar, Co-Chair

Professor Oscar Dubon, Co-Chair

Electronic Chip cooling has become an important issue with the ever increasing transistor densities and computing power demands. One of the crucial components of the thermal management system is high-performance thermal interface materials (TIMs), the materials connecting various solid-solid interfaces in packaged electronic devices. Ideal TIMs have the characteristics of high mechanical compliance and high intrinsic thermal conductivity. Vertically Aligned Carbon Nanotube (CNT) arrays are promising for advanced TIMs since they possess both characters yet poor contact to the target surface can limit the overall performance. Recently, indium-assisted bonding has been found to enhance the contact conductance by a factor of 10, which inspires a comprehensive study of the CNT-array thermal transport properties. This thesis presents a systematic study on the thermal transport and mechanical properties of CNT arrays. The CNT array density and length are controlled via the thermal annealing duration and ethylene exposure duration in water-assisted chemical vapor deposition synthesis. The thermal transport properties are measured accurately by phase-sensitive photo thermal reflectance thermometry. The thermal contact conductance between CNT array and Glass increased close to linearly by increasing the volume fraction of the CNT array. The increase of volume fraction can potentially increase the number of contacting tubes which further enhance the contact area. In addition, the effective thermal conductivity increases monotonically with the increase of volume fraction of the CNT array. Quantitatively, it has been found that the increasing trend of thermal conductivity is larger than the increasing trend of volume fraction. The strain and buckling behavior of CNT arrays under compressive stress were systematically studied. It has been verified both experimentally and analytically that buckling in lower density CNT array results in a further decrease of thermal conductivity. The thermal conductivity of CNT array decreases as the structure changes from vertically aligned to buckled, while the thermal conductivity rises back as the buckling structure becomes more compact. The rise of thermal conductivity with the buckling structure is attributed to the rise of the thermal contact conductance between tubes. The thermal contact conductance between CNT array and glass increases as the compressive stress increases to certain degree, while further increase of stress causes fatigue at the contacts, which decreases the contact conductance. These results demonstrate how thermal transport properties vary as a function of CNT array density and as a function of the strain of CNT array. With such

trends, the thermal properties can be further increased by understanding the underlying mechanisms for such trends.

Table of Contents

| | |
|---|----|
| Table of Contents | i |
| List of Figures | ii |
| List of Tables | v |
| Acknowledgment | vi |
| 1 Introduction..... | 1 |
| 1.1 Thermal Interface Materials in Electronic Packaging | 1 |
| 1.2 Fundamentals of Carbon Nanotube | 4 |
| 1.2.1 Mechanical Properties | 6 |
| 1.2.2 Thermal Transport Properties..... | 7 |
| 1.3 Overview of the dissertation | 9 |
| 2 Carbon Nanotube Synthesis..... | 10 |
| 2.1 Growth Mechanism of Carbon Nanotube Array by Chemical Vapor Deposition..... | 10 |
| 2.1.1 Formation of Catalyst Nanoparticles..... | 11 |
| 2.1.2 Water-Assisted Growth..... | 12 |
| 2.2 Carbon Nanotube Array Density Control | 13 |
| 2.3 Carbon Nanotube Array Length Control | 18 |
| 2.4 Summary | 21 |
| 3 Experimental Technique for Thermal Characterization of Carbon Nanotube Array | 22 |
| 3.1 Thermal Measurement Technique for Thin-Film Materials | 22 |
| 3.2 Phase Sensitive Photo Thermal Reflectance Thermometry..... | 23 |
| 3.3 Thermal Properties Measurement | 27 |
| 3.4 Summary | 34 |
| 4 Thermal Transport Properties and Buckling Behavior of Carbon Nanotube Array | 35 |
| 4.1 Effect of Surface Roughness on Thermal Contact Conductance of Copper-Carbon Nanotube Array Interfaces | 35 |
| 4.2 Density Dependent Thermal Transport Properties of Carbon Nanotube Array | 41 |
| 4.3 Buckling Behavior of Carbon Nanotube Array | 49 |
| 4.4 Effect of Buckling on Thermal Transport Properties of Carbon Nanotube Array | 55 |
| 4.5 Summary | 61 |
| 5 Conclusions and Future Works..... | 63 |
| References..... | 64 |
| Appendix A Temperature Field Derivation..... | 69 |
| Appendix B Load Cell Calibration..... | 72 |

List of Figures

| | |
|---|----|
| Figure 1.1. Schematic of an electronic packaging structure. | 2 |
| Figure 1.2. Schematic showing (a) the poor contacts at the solid-solid interface which causes large temperature jump between chip and heat spreader and (b) the solid-solid interface with TIMs which decreases the temperature jump. | 3 |
| Figure 1.3. Schematic diagram showing the degree of compliance and thermal conductance of various TIMs. The red arrow shows how a CNT array can potentially overcome all the shortcomings of commercially-used-TIMs. | 4 |
| Figure 1.4. Structure of (a) a single-walled CNT and (b) a multi-walled CNT. (c) TEM image of a typical multi-walled CNT showing the interlayer distance of approximately 3.4 angstrom. Figure (a) and (b) are from Ref 15, ¹⁸ and (c) is from Ref 14. ¹⁷ | 5 |
| Figure 1.5. SEM image of a vertically aligned CNT array. Figure 1.5 is taken from Ref 3. ³ | 5 |
| Figure 1.6. The buckling behavior of a CNT array under axial compression. Figure 1.6. is taken from Ref 3. ³ | 7 |
| Figure 1.7. The thermal conductivity of an individual multi-walled carbon nanotube measured as a function of temperature. The thermal conductivity reaches 3000 W/m-K at room temperature. Figure 1.7 is from Ref 11. ¹¹ | 8 |
| Figure 2.1. Schematic illustration of a CVD setup. | 11 |
| Figure 2.2. Schematic image of the catalytic growth mechanism of carbon nanotube. | 11 |
| Figure 2.3. Schematic diagram of the formation of catalyst. | 12 |
| Figure 2.4. Schematic diagram describing (a) Ostwald ripening and (b) hydroxyl stabilization. The diagram is taken from Ref 64. ⁶⁵ | 13 |
| Figure 2.5. CVD process diagram for the growth of CNT arrays. The furnace is ramped from room temperature to 750°C. The annealing time is varied from 0, 2, to 7 minutes. H ₂ , H ₂ O and Ar are introduced from room temperature till the end of the process. C ₂ H ₄ is introduced to initiate CNT array growth. | 14 |
| Figure 2.6. SEM image of the CNT array side view. | 14 |
| Figure 2.7. (a)-(c) SEM images of the catalyst nanoparticles and (d)-(f) the corresponding TEM images of the carbon nanotubes. Before CNT-array growth, the catalysts were annealed in H ₂ : 80 sccm for (a) and (d) 7 minutes, (b) and (e) 2 minutes, (c) and (f) 0 minutes. | 15 |
| Figure 2.8. (a) and (b) SEM images of the catalyst nanoparticles and the corresponding (c) and (d) TEM images of the carbon nanotubes formed on (a) and (c) sputtered Al ₂ O ₃ and (b) and (d) ALD Al ₂ O ₃ | 16 |
| Figure 2.9. The CNT array volume fraction measured as a function of annealing duration. The volume fraction increases as the annealing duration decreases and reaches to maximum by increasing the H ₂ flow rate to 110 sccm with ALD Al ₂ O ₃ support layer. | 18 |
| Figure 2.10. Volume fraction and length of CNT array measured as a function of H ₂ flow rate. | 19 |
| Figure 2.11. The length of CNT array measured as a function of growth time. | 20 |
| Figure 2.12. The volume fraction of CNT array measured as a function of growth time. | 20 |
| Figure 3.1. Schematic diagram of pump and probe beam intensity plotted as a function of time. | 24 |
| Figure 3.2. Schematic of the experimental setup of Phase Sensitive Photo Thermal Reflectance Thermometry. | 25 |
| Figure 3.3. The image of the (a) pump and (b) probe beam spots under CCD camera. | 25 |

| | |
|--|----|
| Figure 3.4. Schematic of the heat conduction system estimated by the pump beam radius, r_{pump} , and the thermal penetration depth, L_p . The heat conduction system is close to (a) 3 dimensional when $r_{\text{pump}} \ll L_p$, and (b) 1 dimensional when $r_{\text{pump}} \gg L_p$ | 26 |
| Figure 3.5. Schematic illustration of two kinds of sample substrates resulting in different pump and probe beam paths. (a) The substrate is opaque, and the pump and probe beams can only be focused on top of the substrate. (b) The substrate is transparent and the pump and probe beams penetrate through the substrate and focused on top of the film. | 27 |
| Figure 3.6. Schematic of the heat conduction model for the glass substrate. | 28 |
| Figure 3.7. Phase response (circles) of the glass sample and the phase solution calculated from the heat conduction model (solid line). | 29 |
| Figure 3.8. Schematic of the heat conduction model for the glass-indium-CNT array three-layer structure. | 30 |
| Figure 3.9. Phase response (circles) of the glass-indium-CNT array, three-layer structure and the corresponding best-fit solution solved from the heat conduction model (solid line). | 32 |
| Figure 3.10. Phase response (circles) and the corresponding best-fit solutions with CNT array in 90 microns in length and 1.1% in volume fraction (green solid line) and with CNT array 45 microns in length and 2.2% in volume fraction (blue solid line). | 34 |
| Figure 4.1. (a) Top view of the sputtered Cu surface. The rms roughness is 0.005 microns. (b) Top view of the Cu surface scratched by 3-micron grit. The rms roughness is 0.024 microns.... | 36 |
| Figure 4.2. Top view SEM image of the CNT array sequentially coated with 10 nm-Cr and 150-nm Au. | 36 |
| Figure 4.3. AFM topographic profile of the CNT array top surface sequentially coated with 10 nm-Cr and 150-nm Au. | 37 |
| Figure 4.4. The sample structure and the pump and probe beam path. | 38 |
| Figure 4.5. Measured phase responses and their standard deviations (circles) for various Cu surface roughness samples along with their best-fit solutions (solid lines). | 40 |
| Figure 4.6. Cu-CNT array contact conductance and effective thermal conductivity of CNT array as a function of Cu surface roughness. | 41 |
| Figure 4.7. Phase responses with error bars (circles) with the corresponding best fit curve (solid lines) for each volume fraction (%) of CNT array. | 42 |
| Figure 4.8. $G_{\text{Glass-CNT array}}$ and $k_{\text{CNT array}}$ versus volume fraction (%) of CNT arrays. Both $G_{\text{Glass-CNT array}}$ and $k_{\text{CNT array}}$ increase monotonically as the volume fraction increases. | 43 |
| Figure 4.9. Side views SEM images of the CNT array with (a) 1.84% and (b) 0.87% in volume fraction before compression. Both the CNT arrays are ~ 130 microns in length. After compression, the CNT array with initially (c) 1.84% in volume fraction decreases 30 microns in length while the CNT array with initially (d) 0.87% in volume fraction decreases 100 microns in length. The scale bar in image (a)-(d) is 40 microns. | 45 |
| Figure 4.10. Schematic cross view of (a) the vertically aligned CNT array and (b) the CNT array with layered structure. Both the CNT arrays in (a) and (b) include N number of tubes. While the CNT array with (b) layered structure has n number of layers and $2n-1$ number of packets. Schematic (c) shows the single packet between two tubes. | 46 |
| Figure 4.11. Thermal resistance network modeling the heat conduction in the CNT array with layered structure. | 46 |
| Figure 4.12. Measurement system for compressive test. | 50 |
| Figure 4.13. Stress-strain diagram of 0.6% volume fraction CNT arrays. | 51 |
| Figure 4.14. Turning points in the stress-strain diagram of 0.6% volume fraction CNT array. | 52 |

| | |
|---|----|
| Figure 4.15. SEM images of the 0.6% volume fraction CNT array after compression, where the compressions were stopped at (a) 42 kPa, (b) 58 kPa, (c) 73 kPa, and (d) 189 kPa. Image (e) shows the higher resolution of image (d). | 53 |
| Figure 4.16. Stress relaxation curve of the 0.6% volume fraction CNT array corresponding to the initial stress. | 54 |
| Figure 4.17. The stress-strain diagram of the 0.6% volume fraction CNT array under cyclic compression. Figure (a) shows the cyclic compression is within first region (1 st and 2 nd cycle) and (b) shows the cyclic compression is at the turning point (1 st cycle), within the second region (2 nd cycle), and at the end of the third region (3 rd cycle). | 54 |
| Figure 4.18. The stress strain diagram corresponds to the CNT array with 0.4%, 0.6%, and 0.8% in volume fraction. | 55 |
| Figure 4.19. The stress-strain diagram of the 165-micron CNT array and the 290-micron CNT array. Both the CNT arrays are initially 0.6% in volume fraction. | 56 |
| Figure 4.20. Thermal conductivity of CNT array and glass-CNT array contact conductance plotted as a function of applied compressive stress. | 57 |
| Figure 4.21. Thermal conductivity of CNT array and glass-CNT array contact conductance plotted as a function of strain of the CNT array. | 58 |
| Figure 4.22. $k_{CNT\ array}$, $k_{CNT\ array_k}$, and $k_{CNT\ array_G}$ plotted as a function of strain of the CNT array. | 61 |
| Figure B.1. Image of power supply and voltmeter. | 72 |
| Figure B.2. Image of (a) a load cell and (b) weights on top of the load cell. | 73 |
| Figure B.3. Output voltage plotted as a function of load. | 73 |

List of Tables

| | |
|---|----|
| Table 2.1. Catalyst densities, averaged tube outer diameters, mass densities and volume fractions of CNT arrays corresponding to growth conditions. | 17 |
| Table 3.1. The length, the thermal conductivity, and the volumetric heat capacity of each layer. | 32 |
| Table 3.2. The parameters for the best-fit solution solved from the heat conduction model. | 33 |
| Table 4.1. The length, the thermal conductivity, and volumetric heat capacity of glass, Cu, and the CNT array. | 38 |
| Table 4.2. The best fit solutions of $G_{Cu-CNT\ array}$ and $k_{CNT\ array}$ corresponding to the Cu surface roughness. | 40 |
| Table 4.3. The best-fit-solution fitting parameters corresponding to the volume fraction of CNT arrays. | 42 |
| Table 4.4. The best fit solutions of $k_{CNT\ array}$, $G_{In-CNT\ array}$ corresponding to the compressive stress and strain of the CNT array. | 57 |
| Table 4.5. $k_{CNT\ array}$, $k_{CNT\ array_k}$, $k_{CNT\ array_G}$, and G_{Van_i} with the corresponding structure and strain of the CNT array. | 60 |

Acknowledgment

First and for most, completing this work would not have been possible without the help of numerous individuals, and I would like to sincerely acknowledge all of them.

I would like to thank my advisors, professor Arun Majumdar, professor Oscar Dubon, and professor Costas Grigoropoulos. I appreciate them for giving me insights, guiding me being a researcher, and moreover, giving me encouragements and supports as I struggle through school works and even personal life. I feel fortunate and am truly grateful to have such a wonderful opportunity to work with them. In addition, I would like to thank professor Liwei Lin for agreeing to serve in my dissertation committee.

I would also like to thank my senior co-worker, Yang Zhao. I've been working with her on this project ever since the beginning of my graduate study; I appreciate her for sharing me all the experiences and knowledge she has. Our discussions and debates give me inspirations. Working with her is a very precious experience.

Throughout the years of my graduate study, I have obtained a lot of helps from lab members from various groups. I would like to thank Renkun Chen, Suzanne Singer, Yusra Dogan, and Ming-Tsang Lee for training me on my preliminary exam; I have learned from them not just the skills of answering questions in front of black boards, but the fundamental sciences behind the questions. I would like to thank Jayakanth Ravichandran, Kedar Hippalgaonkar, Dusan Coso, and Zhijie (James) Wang for helping me out on course works and even research. I would like to thank Dongyan Xu, Antje Rey, Chuanhua Duan, Ming-Chang Lu, and Ya-Mei Chen for giving me encouragements as friends and as mentors. I would like to thank Joe Feser for training me on my qualifying exam which makes me think deeper about my works. I would like to thank Jonathan Malen, Jae Hun Seol, Vinod Srinivasan, David J. Hwang, Sang-Gil Ryu, Eunpa Kim, Jungbin In, Jae-Hyuk Yoo for helping me out on my experiments. I would also like to thank members from Dubon's group, Petra Specht, Douglas Detert, Alejandro Levander, Alex Luce, Grant Buchowicz, Joe Wofford, and other members from Majumdar's group, Shannon Yee, Cheng Zheng, Bauling Huang, Robert Wang, Digvijay Raorane, Kanhayalal Baheti, Chris Zueger, Justyn Jaworski, Keisuke Yokoyama, Sanjiv Sinha, Marta Cerruti, for providing me inputs to this work.

Next, I would like to thank the staffs from UC Berkeley Microlab, Xiaofan Meng, Matt Wasilik, Danny Pestal, and the staffs from Molecular Foundry at LBL, Tev Kuykendall, Tracy Mattox, for training me and taking good care on the critical tools which I have used in this work.

I would like to acknowledge financial support from Office of Naval Research through a MURI grant (Grant No. N00014-07-1-0723, Program Manager Mark Spector). I would also like to thank the program head principle investigator, Professor Pam Norris, and her student, Justin Smoyer from University of Virginia for giving helpful comments to this work.

Last but not least, I would like to thank my family members, my parents, my brother, my sister-in law, and my husband, Hsan-Yin Hsu. They are always by my side no matter what, and I am truly grateful for their endless love and selfless support.

1 Introduction

Inadequate heat dissipation in electronics, photovoltaics, or thermoelectric devices can cause overheating, which can shorten device lifetime. One of the limiting components of the heat transfer process in such solid-state devices is the solid-solid interface. Thermal interface materials (TIMs) connect solids and enhance interfacial thermal conductance. To be effective, TIMs need to not only have high intrinsic thermal conductivity, which ensures high volumetric thermal conductance,¹ but also high mechanical compliance, which enhances contact area and prevents fatigue failure of the bond driven by thermal expansion mismatch. Traditionally, TIMs are made of a silicone-based matrix loaded with thermally conductive particles. The highest thermal conductivity with such TIMs is only around 8 W/m-K.² Carbon nanotubes (CNTs) represent a new and potentially attractive material to be used as TIMs since they exhibit not only high mechanical compliance,^{3,4,5,6,7} but also high thermal conductivity along their axial direction at room temperature.^{8,9,10,11} By bridging two surfaces with vertically aligned CNT array, one may achieve high thermal conductance while not losing mechanical compliance. The purpose of this study is to understand the thermal transport and mechanical behavior of CNT array. This chapter first presents the role of TIMs in thermal packaging. Literature reviews on the fundamentals of CNTs including thermal transport properties and mechanical properties are introduced in the second part of this chapter.

1.1 Thermal Interface Materials in Electronic Packaging

On-chip power density, P , is generally estimated as the number of devices per chip, N , the capacitance of the logic element, C , the square of the operating voltage, V , and the operating frequency, f :¹²

$$P \approx NCV^2 f \quad (1.1)$$

The increases in the number of devices per chip and the operating frequency have driven power per chip into very high level, ~ 200 W;¹² that is to say, the averaged power density is close to 2 MW/cm² for a chip area of 1 cm². Therefore, chips require thermal control systems to maintain a suitable operating temperature: Otherwise, high temperatures could adversely affect device performance, lifetime and reliability.

Thermal packaging requires multiple tasks. Consider an electronic package illustrated in Figure 1.1. The front side of the chip is attached to the package substrate with metal solder bumps, and the back side of the chip is attached to the heat sink with a heat spreader to maintain the device within its operating temperature. The heat generation at the chip will be dissipated to the environment towards the direction of heat sink. The packaging structure indicates that there are multiple solid-solid interfaces.

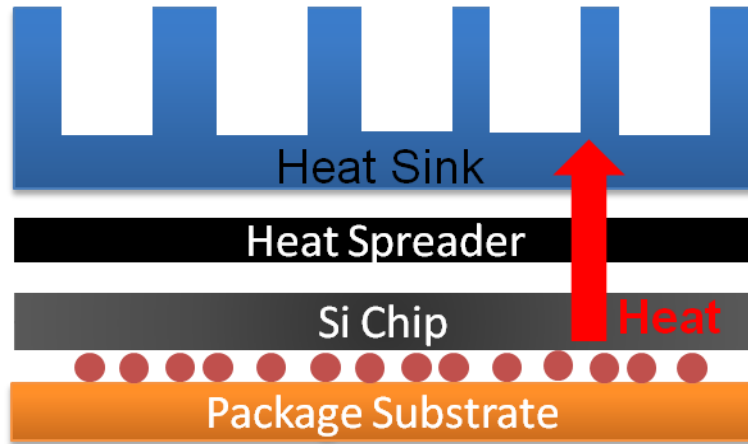


Figure 1.1. Schematic of an electronic packaging structure.

As shown in Figure 1.2 (a), the actual contact area between the two surfaces, i.e., between the heat spreader and chip, is much less than the apparent contact area when they join with little pressure.¹ Therefore, there is a contact resistance, R_c'' , that causes temperature difference between the two surfaces. If the heat flux generated on the chip is 2MW/m^2 , the contact conductance, G_c (the inverse of R_c''), at the interface is $\sim 0.01 \text{ MW/m}^2\text{K}$,¹³ and the heat spreader is kept at 35°C , then the chip temperature is 235°C . Such a temperature is much higher than the device operating temperature, 85°C .¹⁴ This indicates that a thermally conductive TIMs needs to be applied at the interface in order to enhance heat transfer and decrease the temperature difference between heat spreader and chip (Figure 1.2 (b)). Once the TIM is applied, there is still an overall thermal resistance between the heat spreader and chip which can be expressed as

$$R_{overall}'' = R_{bulk}'' + R_{c1}'' + R_{c2}'' \quad (1.2)$$

and

$$R_{bulk}'' = \frac{L}{k_{TIMs}} \quad (1.3)$$

where L is the bulk length of the TIM, k_{TIMs} is the cross-plane thermal conductivity of the TIM, and R_{c1}'' and R_{c2}'' are the contact resistances between the TIM and heat spreader and the TIM and chip. From equation (1.2) and (1.3), it is evident that not only high thermal conductivity, but also the bulk length and the contact resistances are key factors to reduce the overall resistance.

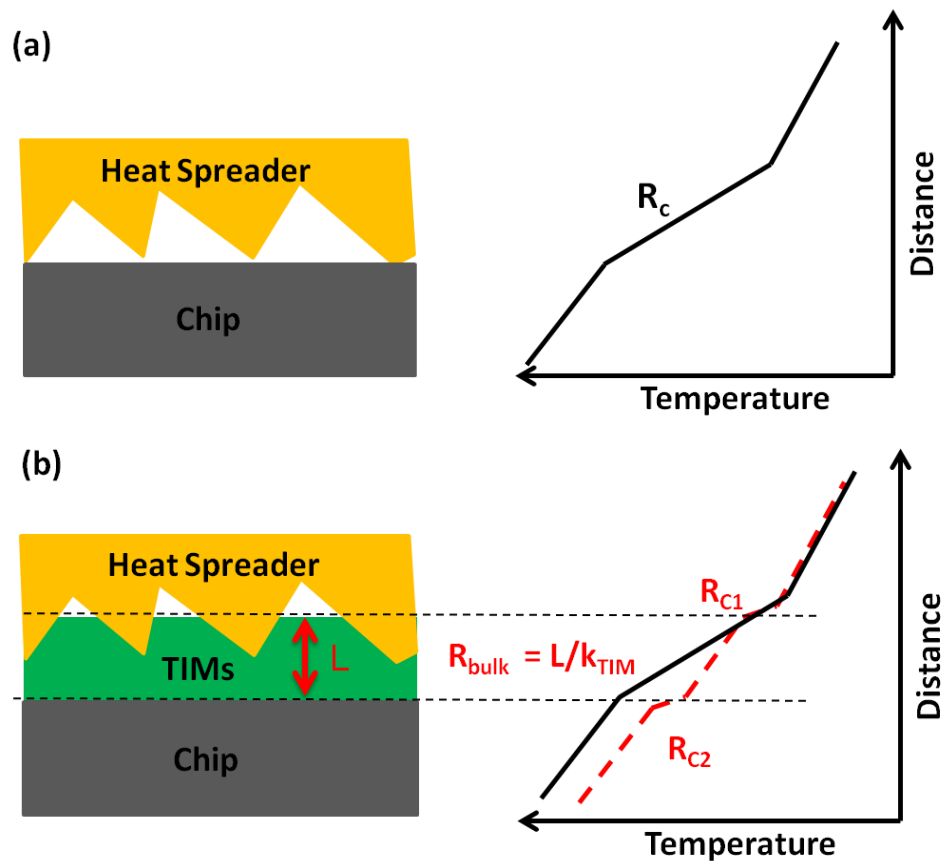


Figure 1.2. Schematic showing (a) the poor contacts at the solid-solid interface which causes large temperature jump between chip and heat spreader and (b) the solid-solid interface with TIMs which decreases the temperature jump.

Intuitively, adding a fluid with high thermal conductivity, such as Hg, can meet all the requirements of being thin, thermally conductive and mechanically compliant. However, the components in the electronic packaging (shown in Figure 1.1) have different coefficients of thermal expansion; when the chip temperature changes, each component expands or contracts at a different rate, which causes mechanical stress such as cyclic tensile, compressive stress or shear stress. The contact conductance between TIMs to spreader and between TIMs to chip may decrease if TIMs cannot sustain the mechanical stress. A fluid does not sustain mechanical stress; one needs a solid material with lower elastic modulus (compared to the modulus of packaging components) with high ultimate strength to prevent fatigue failure caused by the thermal stress. The most common commercial TIMs are greases, phase change material, adhesives and indium solder. Thermal greases are made of silicone-based matrix with thermally conductive particle such as silver particles. The thermal conductivity is around 8 W/m-K ,² and it has low viscosity, which enables matrix material to fill the cavity at the interface. Similar to a fluid, the disadvantage of grease is that it may be pump-out with applied stress; the overall thermal conductance of thermal grease is around $0.1 \text{ MW/m}^2\text{-K}$.¹ Phase change materials (PCMs) and adhesives have relatively lower thermal conductivity than thermal greases, besides, phase change materials requires attach pressure which can lead to mechanical stress, while adhesives has high post-cured elastic modulus and low ultimate strength which could have fatigue failure from

thermal expansion mismatch; the overall thermal conductance is around $0.1 \text{ MW/m}^2\text{-K}$.¹ Metal solders have highest thermal conductivity among all with the thermal conductivity around $20\text{-}90 \text{ W/m-K}$.¹⁵ It has low viscosity when molten; however, the solidified solder has high elastic modulus while low ultimate strength compared to a copper heat spreader and silicon chip; the overall thermal conductance is around $0.1 \text{ MW/m}^2\text{-K}$ ¹⁵ for still.

Figure 1.3 shows the degree of compliance and thermal conductance for the various TIMs. The degree of thermal conductance is evaluated from the overall thermal conductance, while the degree of compliance is the ability to fill the cavity while sustain mechanical stress caused by thermal expansions. A novel material, a CNT array, is proposed in this work to achieve ultra-high overall thermal conductance. It could potentially overcome all the shortcomings of the commercial TIMs for its exceptional mechanical compliance and thermal transport ability. The fundamental structure of CNTs and the thermal and mechanical properties will be introduced in the following section.

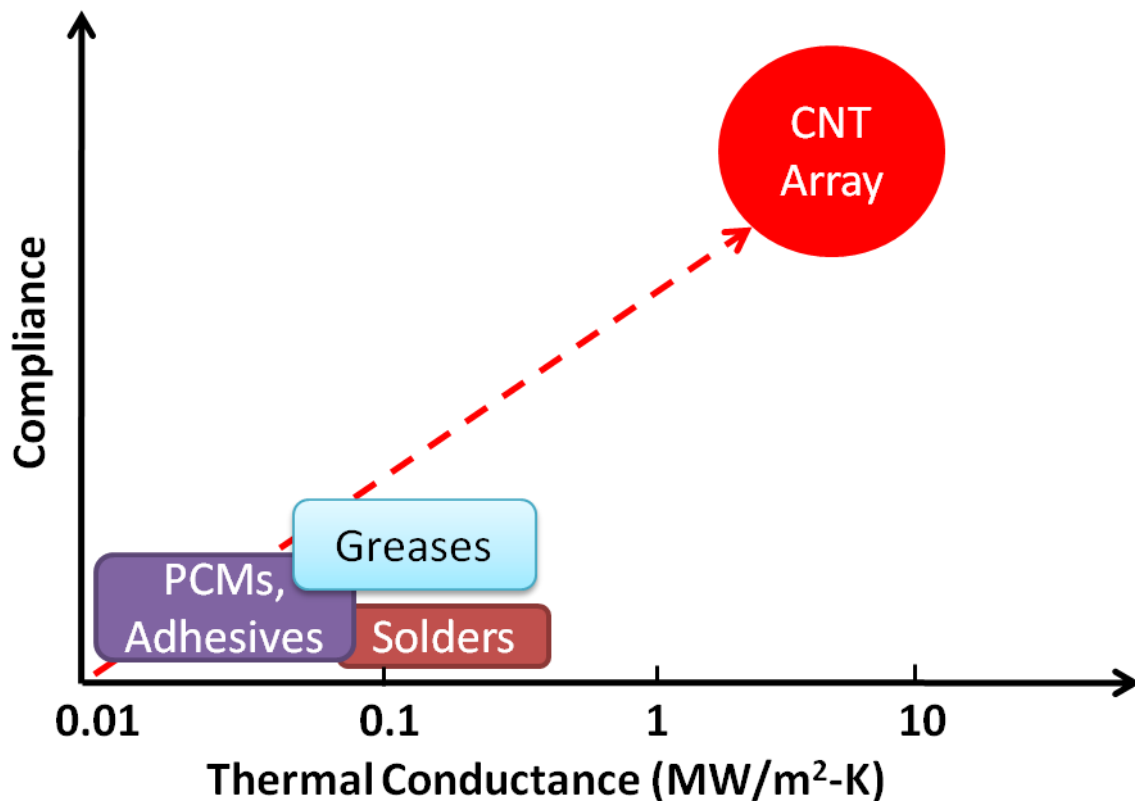


Figure 1.3. Schematic diagram showing the degree of compliance and thermal conductance of various TIMs. The red arrow shows how a CNT array can potentially overcome all the shortcomings of commercially-used-TIMs.

1.2 Fundamentals of Carbon Nanotube

Carbon Nanotubes were first discovered by Iijima in 1991.¹⁶ A single-walled CNT (shown in figure 1.4(a)) has a hollowed cylindrical structure with one layer of rolled-up graphene, where the graphene has a honeycomb structure with strong C-C sp^2 bonding. A multi-walled CNT (shown in Figure 1.4(b)) consists of multiple layers of rolled-up graphene, where the van der

Waals bonding induces the layers to be concentrically aligned with each other; and the distance between layers is approximately 3.4 Å (shown in Figure 1.4(c)).¹⁷

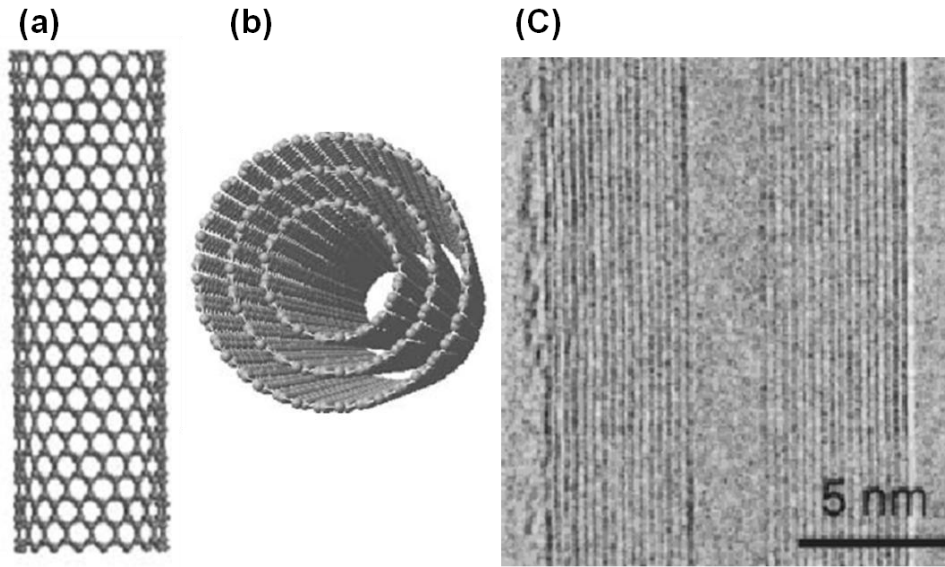


Figure 1.4. Structure of (a) a single-walled CNT and (b) a multi-walled CNT. (c) TEM image of a typical multi-walled CNT showing the interlayer distance of approximately 3.4 angstrom. Figure (a) and (b) are from Ref 15,¹⁸ and (c) is from Ref 14.¹⁷

When carbon nanotubes are grown closely packed with each other, they are able to align themselves along the perpendicular direction due to the van der Waals interaction between the tubes.¹⁹ A vertically aligned CNT array is illustrated by an SEM image in Figure 1.5, where the tube density typically ranges from $\sim 10^{10}$ - 10^{11} tubes/cm².^{20,21,22}

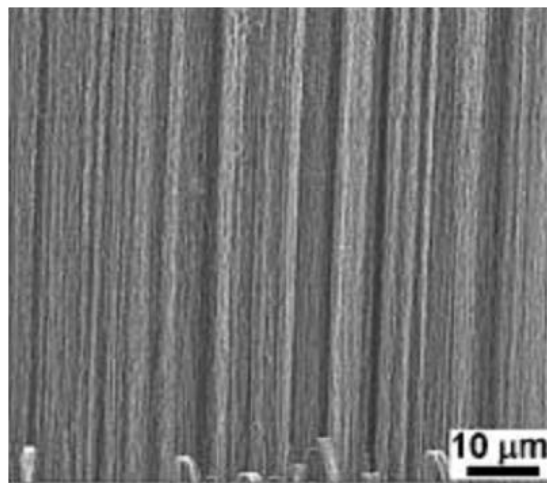


Figure 1.5. SEM image of a vertically aligned CNT array. Figure 1.5 is taken from Ref 3.³

1.2.1 Mechanical Properties

Carbon nanotubes are expected to possess exceptional mechanical properties similar to graphene and graphite. As early as 1993, the tensile modulus of an individual single-walled CNT was calculated to be ~ 1 TPa.²³ The first experimental measurement was performed by Treacy *et al.* in 1996; they measured the tensile modulus of multi-walled CNT in a range 0.41-4.15 TPa.²⁴ The compressive modulus was found to be ~ 425 GPa.²⁵ The lower elastic modulus is due to the high aspect ratio of CNT, which induces buckling behavior. However, it was found that CNT is flexible and strong, a cyclic compression test was applied on a multi-walled CNT, and the multi-walled CNT can buckle and straighten reversibly up to a yield strength of 1.7 GPa,²⁵ such yield strength is higher than the ultimate strength of most material except for diamond.

Compared to individual CNTs along axial direction, ropes of CNTs are rather soft along radial direction. It was found that they can be easily deformed in radial direction by van der Waals force,²⁶ and the degree of deformation is affected by the number of walls where single-walled CNT has the highest degree of deformation.²⁷ It was reported in 1999 that the transverse mechanical behavior of single-walled CNT ropes is dominated by the inter-tube slippage, and the shear modulus was measured to be 1 GPa.²⁸

The soft behavior of CNT ropes in the radial direction can influence the mechanical behavior of CNT array. From mid 2000 until now, researchers have focused on measuring the elastic modulus of CNT arrays, where the effective compressive modulus, 92-820 MPa,^{3,29} still remain to be lower than the effective tensile modulus(corrected by the actual tubes area), 34 GPa.²⁹ The buckling behavior of CNT array under axial compression has been studied by several groups,^{3,7,30,31} it was examined by scanning electron microscopy (SEM) image and found out that the buckling is coordinated under uniform compression (as shown in Figure 1.6),^{3,31} and the wavelength of the buckling structure could affect the compressive modulus.⁷ To compare the modulus of a CNT array with the modulus of electronic components, such as copper or silicon chip (~ 100 GPa), one needs to consider a CNT array as a bulk film and calculate the stress by the film area. In this case, the tensile modulus is 0.1 GPa, and the compressive modulus is 2.5-12 MPa, where the CNTs occupies $\sim 13\%$ of the film for 12 MPa and 0.3% of the film for 2.5MPa. In 2012, Zhang *et al.* showed that the compressive modulus of a CNT array increased close to linearly from 250MPa to 2GPa as the filled fraction of CNT array increased from 25% to 76%.³²

From the reported analysis, several factors can affect the modulus of a CNT array: inter-tube interaction, filled fraction of CNT array, and the buckling behavior. It is important to understand the correlation among them for the best performance of CNT arrays as a TIM.

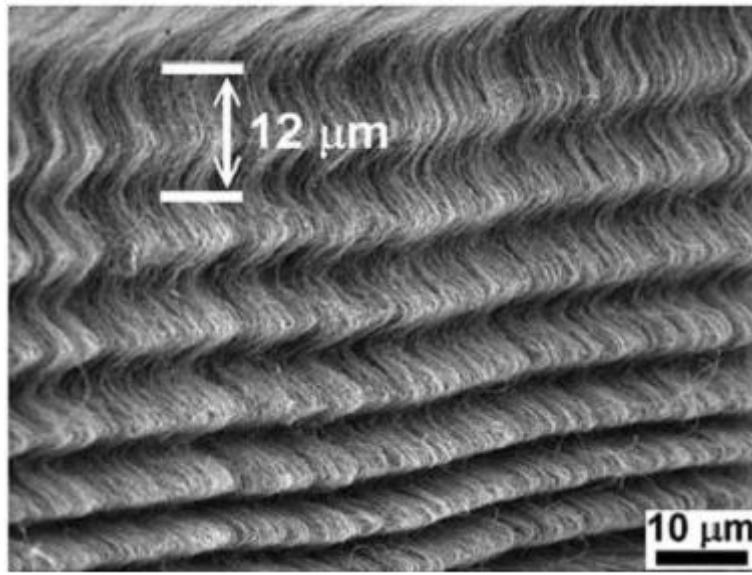


Figure 1.6. The buckling behavior of a CNT array under axial compression. Figure 1.6. is taken from Ref 3.³

1.2.2 Thermal Transport Properties

An unusually high thermal conductivity should be expected in carbon nanotubes as a result of the strong sp^2 bonds and the periodic arrangement of carbon atoms in the graphitic cylinder.³³ Followed by the discovery of CNTs in 1991,¹⁶ few measurements were done on single-walled and multi-walled CNT ropes; the thermal conductivity has been measured in a range 2.3-200 W/m-K at room temperature,^{34,35} which is much lower than the in-plane thermal conductivity of graphite, ~ 1000 W/m-K.³⁶ An isolated individual carbon nanotube should be highly thermally conductive without defects or softening of phonon modes by the inter-tube van der Waals interaction or by the embedded materials.⁸ Theoretical calculation on the thermal conductivity of single-walled CNTs are predicted to be 3000-6000 W/m-K.^{8,37,38} Due to the difficulty of separating CNT ropes into individual CNT, the experiments were done later on, where the thermal conductivity of the defect free individual single-walled CNT (SWCNT) and multi-walled CNT (MWCNT) were measured to be in the range of 2000-3500 W/m-K^{9,10} and ~ 3000 W/m-K¹¹ at room temperature (as shown in Figure 1.7), respectively, which is close to theoretical predictions.

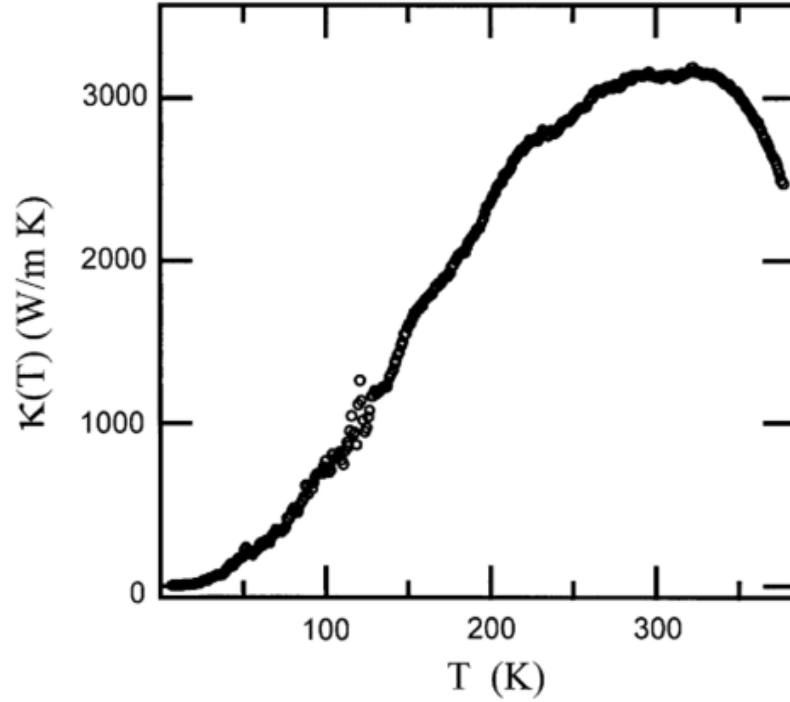


Figure 1.7. The thermal conductivity of an individual multi-walled carbon nanotube measured as a function of temperature. The thermal conductivity reaches 3000 W/m-K at room temperature. Figure 1.7 is from Ref 11.¹¹

Previous studies have embedded randomly oriented CNTs into composite materials for the application of TIMs, and the effective thermal conductivity of the CNTs composite only reached on the order of 1 W/m-k.^{39,40,41,42} An estimate of the thermal conductivity of CNTs composite is used to explain this: the cross-plane effective thermal conductivity of CNTs composite materials can be expressed as

$$k_{effective} = k_{CNT}\phi_{CNTs} + k_{base}(1 - \phi_{CNTs}) \quad (1.4)$$

where k_{CNT} is the intrinsic thermal conductivity of the individual tube, ϕ_{CNTs} is the volume fraction of CNTs, and k_{base} is the thermal conductivity of the polymer composite.⁴³ For a thermal conductivity of individual CNT of 3000 W/m-K, volume fraction of CNTs of 1%, and thermal conductivity of polymer composite of 0.2 W/m-K, the effective thermal conductivity of CNTs composite should be ~30 W/m-K. There are several possible reasons for the difference between this value and the reported data, namely: (a) less than 1% volume fraction of CNTs is embedded in the matrix; (b) the thermal contact resistances formed between CNTs and between CNTs and the base materials impede thermal transport along the main path;^{44,45} (c) the CNT-CNT and CNT-base material contacts degrade the thermal conductivity of individual CNT due to the increase of phonon scattering.⁴³ Subsequent research used dense vertically aligned CNT arrays (up to 17% in volume fraction) embedded in polymer materials to reduce the CNT-CNT contact resistance and CNT-matrix contact resistance along the main path; the cross-plane thermal conductivity of the composite is lower than expectation for still (~5 W/m-K).⁴⁶ This suggests that the matrix material could have a negative impact on the thermal conductivity of individual CNT.

Ideally, if the CNTs were vertically aligned along the cross-plane direction, one could potentially achieve high thermal conductivity in the cross-plane direction while not losing the mechanical compliance. By using vertically aligned CNT arrays bridging two surfaces without matrix materials, negative impacts of CNT-matrix contacts on the thermal conductivity of CNT arrays may be eliminated. However, the reported thermal conductance, including the contact conductance between vertically aligned CNT arrays and various materials (0.02-3 MW/m²-K^{47,48,49}) and the effective thermal conductivity of CNT array (8-250 W/m-K^{49,50,51}), were measured into a wide range of values. To explain this, it has been suggested that the low thermal performance was mainly due to the incomplete contacts between the CNT array and the target substrate.⁴⁹ Therefore, increasing the number and area of the contact of CNTs to the substrate can potentially enhance the thermal performance.^{49,52} In 2007, indium-assisted bonding has been found to enhance the CNT array to boundary contact conductance by a factor of 10 (~ 3 MW/m²-K) due to the reflow ability of indium.⁴⁷ However, there is no clear analysis explaining the thermal transport behavior of CNT arrays, which is an important issue to be addressed for further enhancing the thermal performance of CNT array.

1.3 Overview of the dissertation

The dissertation addresses the thermal transport and mechanical behavior of CNT arrays. In Chapter 2, the synthesis of CNT arrays is introduced. This topic is important since the thermal performance of a CNT array could be affected by length, packing density, and defect density of CNT array. The mechanism of growing impurity free densely-packed CNT arrays is discussed. Length control and density control of CNT array are presented in the last part of this chapter.

Chapter 3 is focused on thermal measurement thermometry. Several thermal measurement methods for investigating the thin film thermal properties are introduced, and the reason for choosing phase sensitive thermal reflectance thermometry in this dissertation is discussed. This is important since one needs a suitable thermometry which has resolution measuring the lowest possible thermal resistance of a CNT array.

In chapter 4, the optimization of CNT-array thermal performance is discussed. The fundamental of thermal transport behavior of CNTs is introduced first. The effects of surface roughness, array length, and the array density on the thermal performance of CNT array are demonstrated from the experimental measurement results. The buckling behavior of CNT array and their effect on the thermal conduction is measured; analysis based on the measurement results is presented at the end of this chapter.

In the final chapter, ideas for future research are discussed. This includes the proposed method for growing thin but dense CNT array, and a better way to attach the CNT array to the target surface in order to improve the thermal contact conductance.

2 Carbon Nanotube Synthesis

The most commonly used techniques to grow CNTs are (1) arc discharge;¹⁶ (2) laser ablation;⁵³ (3) chemical vapor deposition (CVD).⁵⁴ The arc-discharge technique is carried out by the generation of plasma between two closely spaced graphite electrodes (< 1mm apart) with inert gas (He, Ar) under vacuum,⁵⁵ and the anode graphite is consumed and sublimed into carbon source material which condensed partly to form CNTs on the cathode graphite. CNTs were first discovered using arc-discharge method,¹⁶ and it is the most established technique to date. Laser ablation uses a laser to raise the temperature of graphite target to its sublimation point; carbon evaporates from the graphite target which is rapidly cooled by inert gas (He) to form CNTs.⁵³ In CVD, hydrocarbon gas decomposes over a transition metal catalyst at high temperature (~ 750°C-1200°C) and atmospheric pressure to form CNTs.⁵⁶ The CVD method can result in lower degree of crystallinity or higher degree of defect density compared to the arc-discharge⁵⁷ and laser-ablation techniques;⁵³ however, CVD can also be used to readily grow large quantities of CNTs, including highly packed vertically aligned CNT arrays. In 2004, Hata *et al.*²⁰ added a small amount of water vapor into a CVD process (water-assisted CVD) and created a massive growth of highly dense vertically aligned single-walled carbon nanotube with high purity. The water-assisted CVD method is conducted in this work for the growth of vertically aligned CNT arrays; further details of the growth mechanism of CNT array used by water-assisted CVD will be introduced in the following sections. The experimental results of density control and length control of CNT array will be introduced at the end of this chapter.

2.1 Growth Mechanism of Carbon Nanotube Array by Chemical Vapor Deposition

The CVD process usually consists of several steps:⁵⁸ (1) a sample substrate is prepared by the deposition of a support layer (e.g. Al₂O₃, SiO₂) and a catalyst film using transition metal (e.g. Fe, Ni), the support layer often has lower surface energy compared to the metal film which helps the catalyst film transform into nanoparticles upon heating; (2) the substrate then annealed upon heating under H₂ with Ar as a carrier gas in a quartz tube furnace (as illustrated in Figure 2.1), transforming the catalyst film into supported nanoparticles; H₂ is used to impede the oxidation of metal catalyst, which keeps the catalyst at higher surface energy state compared to the support layer; (3) the hydrocarbon source (e.g. C₂H₄) is introduced and decomposed into carbon at ~ 500-1000°C; (4) the carbon interacts with the catalyst which forms CNT.

In the catalytic growth of CNTs, the reaction between 3d electrons of the transition metal catalyst and π electron of carbon plays an important role.⁵⁹ It was proposed that a nanoparticle has very high surface energy per atom, and that the excessive carbon produced in the CVD process can balance the surface energy by assembling a graphene cap on the metal catalyst (as shown in left hand side of Figure 2.2), with its edge strongly chemisorbed on the metal catalyst.⁶⁰ The graphene cap lifts off from the catalyst and additional C continuously adds to the edge of catalyst which forms into hollow tube with constant diameter (as shown in the right hand side of Figure 2.2).⁶¹ The lift off force is possibly due to the release of free energy from the chemical reaction between C and transition metal.⁶²

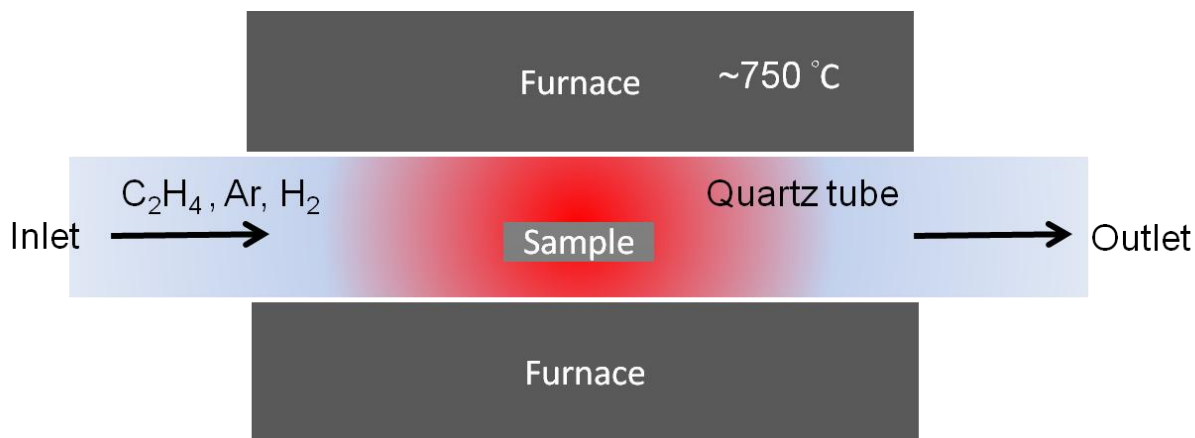


Figure 2.1. Schematic illustration of a CVD setup.

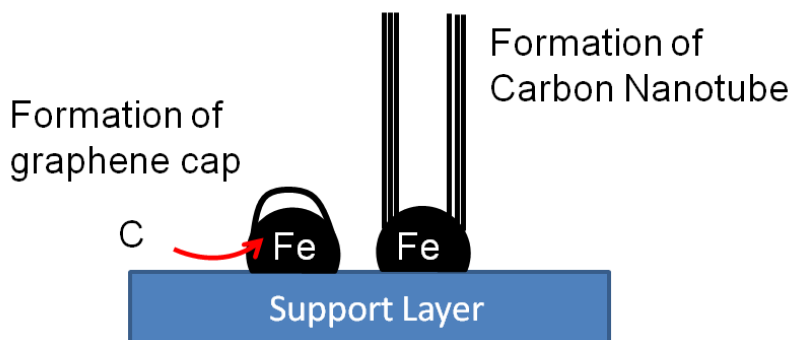


Figure 2.2. Schematic image of the catalytic growth mechanism of carbon nanotube.

2.1.1 Formation of Catalyst Nanoparticles

Both the annealing process and the support layer are critical determinants of the formation of catalyst nanoparticles. In this dissertation, Fe is used as the catalyst and Al₂O₃ is used as the support layer. As shown in Figure 2.3, the Al₂O₃ support layer is located between the Si substrate and the Fe catalyst film. The Fe film is oxidized into Fe₂O₃ while being exposed to air after substrate preparation. The annealing process, which is accompanied by the introduction of H₂ upon heating up the sample, reduces Fe₂O₃ to Fe. The equilibrium shape of the catalyst is determined by the surface energy of the films relative to the gas in the furnace and the interface energy between films.⁵⁸ Since the surface energy of Al₂O₃ is lower than the Fe-Al₂O₃ interface energy plus the surface energy of Fe, the Fe film effectively de-wets the surface and breaks up into nanoparticles. It has been reported that the size of the particles is directly related to the thickness of catalyst film, $d \sim 6h$,^{63,64} where d is the diameter of the particles and h is the thickness of the film.

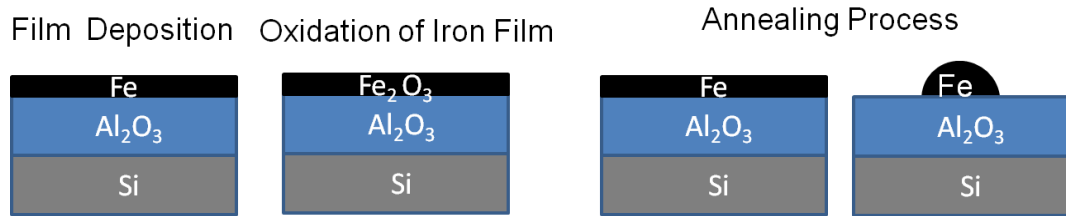


Figure 2.3. Schematic diagram of the formation of catalyst.

However, Nessim *et al*²² and Amama *et al*⁶⁵ have shown that continued annealing in the presence of H_2 leads to coarsening of Fe particles and eventually results in a decrease of catalyst density. It is explained that the Fe atoms diffuse on the Al_2O_3 layer, smaller particle has higher surface energy, and their atoms diffuse to the larger Fe particle due to surface energy minimization. In this case, the larger particles become increasing in size while the smaller particles eventually disappear which results in a decrease in the total number of particle density.

2.1.2 Water-Assisted Growth

The sintering of catalyst is called Ostwald ripening, a schematic diagram describing this phenomenon is shown in Figure 2.4 (a).⁶⁵ The smaller Fe particle shrinks due to the diffusion of Fe atoms; the disappearing Fe particle terminates the growth of CNT. This process can be blocked by adding a small amount of water vapor to annealing.⁶⁵ The combination of H_2 and H_2O creates oxygen and hydroxyl species, which stick on the Al_2O_3 layer and reduce the diffusion of the catalyst atoms (as shown in Figure 2.4 (b)).⁶⁵

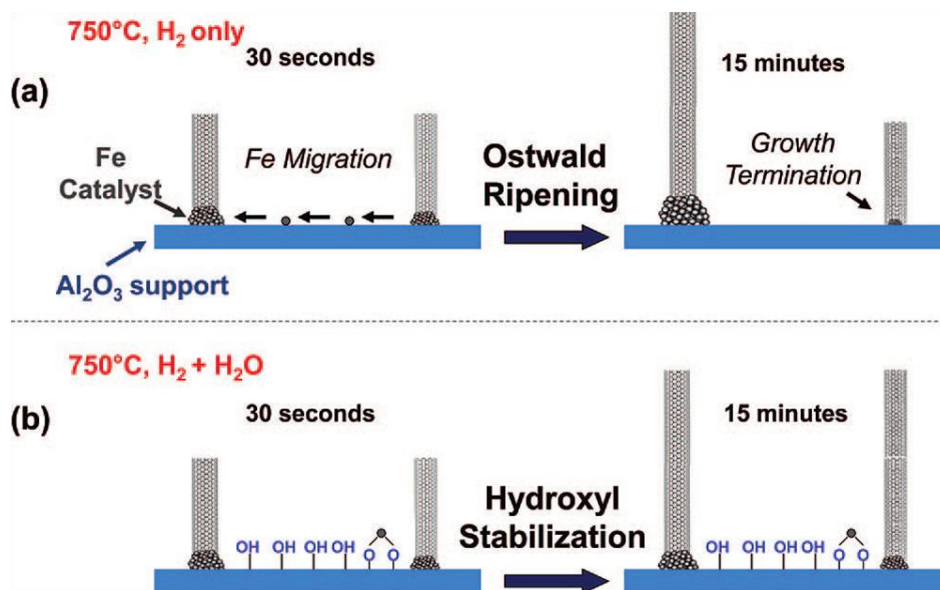


Figure 2.4. Schematic diagram describing (a) Ostwald ripening and (b) hydroxyl stabilization. The diagram is taken from Ref 64.⁶⁵

In addition to reducing Ostwald ripening of catalyst particles, water vapor etches amorphous carbon both coating on the catalyst and CNT. The catalyst produced under water-assisted CVD has higher activity and lifetime.²¹ Moreover, such catalyst particles are able to promote the growth of highly dense vertically aligned single-walled CNT arrays with carbon purity above 99.98%.²⁰ In the following sections, the experiments of density and length control of CNT arrays using the water-assisted CVD method are presented.

2.2 Carbon Nanotube Array Density Control

A series of aligned CNT arrays with controlled mass density are grown on Si chips by chemical vapor deposition. A 20-nm thick Al₂O₃ film is deposited on a Si wafer, and a ~1 nm-thick Fe catalyst layer is thermally evaporated on the Al₂O₃ film. Al₂O₃ support layers have been deposited by two methods: atomic layer deposition (ALD) and sputtering. Since the ALD Al₂O₃ has better film quality compared to the sputtered Al₂O₃,⁶⁶ the two different deposition methods can result in different catalyst density. The volume fractions of the CNT arrays are controlled by H₂ flow rate and the annealing duration using water-assisted CVD method.

The CNT arrays are grown at 750°C under atmospheric pressure. The CVD process diagram for the growth of CNT arrays is shown in Figure 2.5. During CNT synthesis, Ar (150 sccm), H₂, and H₂O (<100 ppm) are introduced from the beginning to the end of the process while C₂H₄ is introduced during the growth process. For the CNTs grown on the substrate with the sputtered Al₂O₃ layer, the flow rate of H₂/C₂H₄ has been varied from 80/80 to 110/120 sccm. For the CNTs grown on the substrate with the ALD Al₂O₃ layer, the flow rate of H₂/C₂H₄ is kept at 110/120 sccm. Once the furnace reaches 750°C, the Fe catalyst on the sputtered Al₂O₃ layer is annealed in H₂ (80 sccm) for 0, 2, or 7 minutes while the Fe catalyst on the ALD Al₂O₃ layer is annealed in H₂ (110 sccm) for 0 minutes. After the annealing process, CNT array growth is

initiated by introducing C_2H_4 , and the growth is continued for 4 minutes. The CNT arrays grow $100\pm 30\ \mu m$ in length under these growth conditions. Figure 2.6 shows an SEM image of the CNT array side view. The annealing time is 0 minute, and the CNT array is grown on a Si substrate with sputtered Al_2O_3 layer.

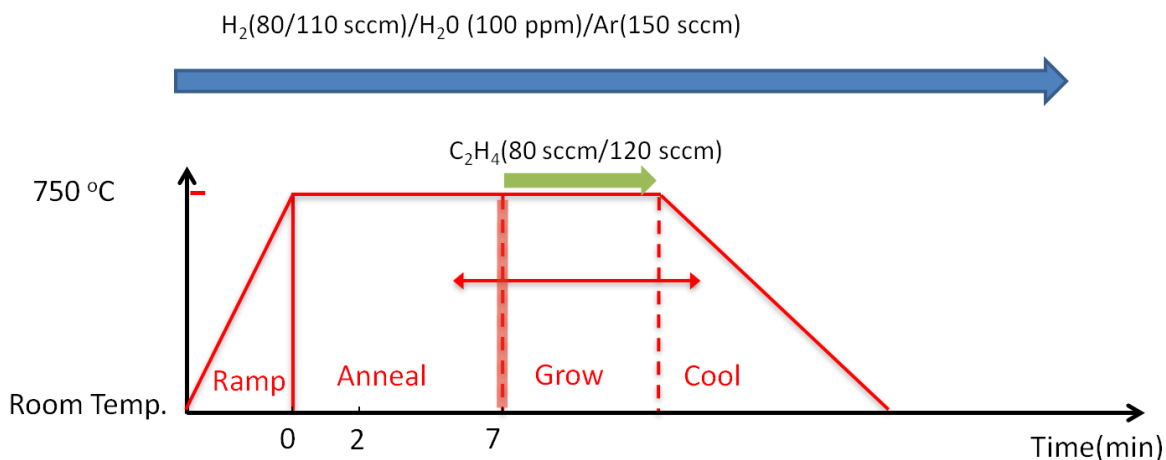


Figure 2.5. CVD process diagram for the growth of CNT arrays. The furnace is ramped from room temperature to $750^\circ C$. The annealing time is varied from 0, 2, to 7 minutes. H_2 , H_2O and Ar are introduced from room temperature till the end of the process. C_2H_4 is introduced to initiate CNT array growth.

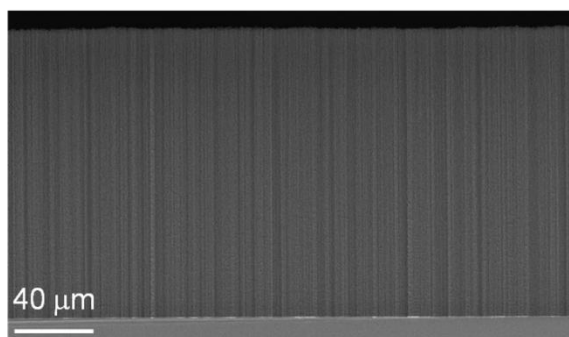


Figure 2.6. SEM image of the CNT array side view.

To allow examination of the catalyst after CNT-array growth, CNT array is burned with oxygen plasma, which exposes the catalyst particles. Top views of the exposed catalyst particles on the substrates are shown in Figures 2.7 (a)-(c) and Figure 2.8 (a) and (b). The number density of catalyst particles increases from 2.4×10^{10} to 4.8×10^{10} to 5.4×10^{10} particles/ cm^2 as the annealing time decreased from 7 to 2 to 0 minutes, keeping a H_2 flow rate of 80 sccm during growth. The particle density can be further increased to 7.8×10^{10} particles/ cm^2 when the H_2 flow rate is increased to 110 sccm with 0 minute annealing time. On the other hand, the roughness of the Al_2O_3 underlayer plays an important role in nanoparticle formation. Compared to the sputtered Al_2O_3 film, the ALD deposited film can yield an even higher particle density ($9.8 \times$

10^{10} particles/cm²). The average tube diameters for each CNT array are measured in TEM images (see Figure 2.7 (d)-(f) and Figure 2.8 (c) and (d)). The statistical results of catalyst particle density and tube diameters are listed in Table 1. Even though the five different growth conditions yield distinct variations of catalyst particle density, the TEM examination of the CNTs indicates that there is no significant difference in the tube diameters. A possible reason for the decrease of catalyst density without changing tube diameter as the annealing duration increases is, instead of sintering with the larger Fe particles, the smaller Fe particles evaporates and eventually disappears.

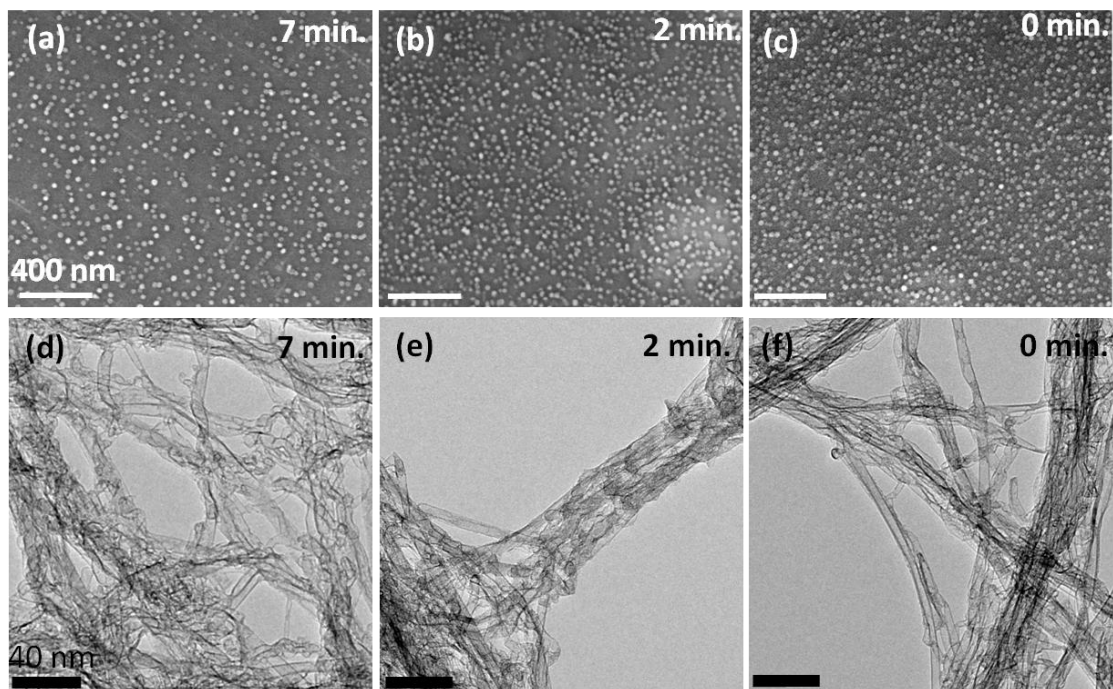


Figure 2.7. (a)-(c) SEM images of the catalyst nanoparticles and (d)-(f) the corresponding TEM images of the carbon nanotubes. Before CNT-array growth, the catalysts were annealed in H₂: 80 sccm for (a) and (d) 7 minutes, (b) and (e) 2 minutes, (c) and (f) 0 minutes.

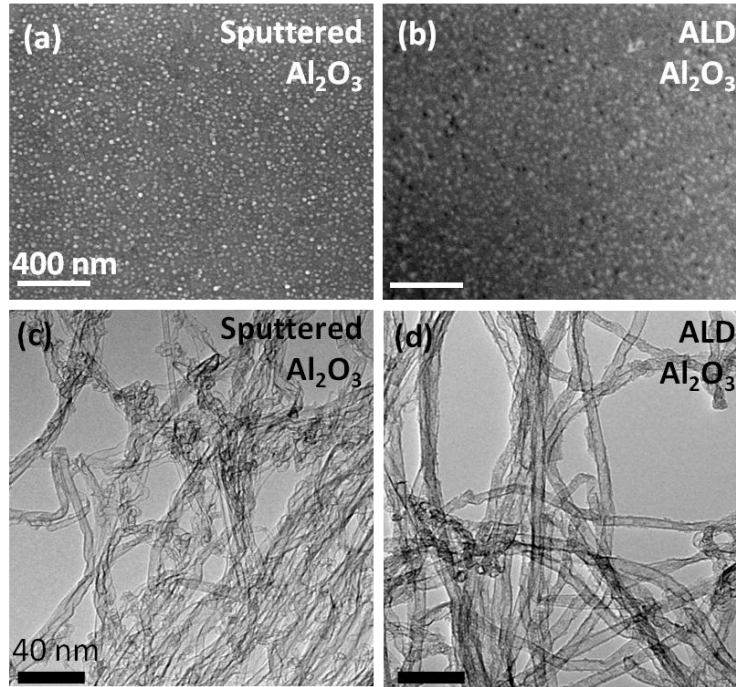


Figure 2.8. (a) and (b) SEM images of the catalyst nanoparticles and the corresponding (c) and (d) TEM images of the carbon nanotubes formed on (a) and (c) sputtered Al_2O_3 and (b) and (d) ALD Al_2O_3 .

The mass density of the CNT array is determined by the measured mass of the CNT array divided by the apparent volume of the CNT array,

$$\rho_{CNTarray} = \frac{M_{CNTarray}}{V_{CNTarray_apparent}} \quad (2.1)$$

where the mass of the CNT array is measured using microbalance (METTLER TOLEDO XS 205) with sensitivity of 0.001 mg, and the apparent volume of the CNT array is determined from the substrate area (1 cm^2) times the length of the as-grown CNT array.

The volume fraction of CNT array is the actual volume of the CNT array divided by the apparent volume of the CNT array,

$$\phi_{CNTarray} = \frac{V_{CNTarray_actual}}{V_{CNTarray_apparent}}. \quad (2.2)$$

Assume that the mass density of an individual CNT equals to the mass of the CNT array divided by the actual volume of CNT array,

$$\rho_{CNT} = \frac{M_{CNT}}{V_{CNT}} = \frac{M_{CNTarray}}{V_{CNTarray_actual}}. \quad (2.3)$$

The volume fraction of the CNT array is determined by the ratio of CNT array mass density to the mass density of an individual tube by combining equation (2.1) and (2.3) with equation (2.2),

$$\phi_{CNTarray} = \frac{\rho_{CNTarray}}{\rho_{CNT}} \quad (2.4)$$

where the mass density of individual multi-walled CNT is $\sim 2.1 \text{ g/cm}^3$.⁶⁷

The averaged mass density and the volume fraction of CNT array increases monotonically as the catalyst density increases (listed in Table 2.1). Plotted against the annealing time (see Figure 2.9), the volume fraction of the CNT array increases monotonically as the annealing time decreases and further increases by increasing the H₂ flow rate to 110 sccm, and finally, the volume fraction reaches a maximum point at around 1.84% with ALD Al₂O₃ underlayer and H₂ flow rate 110 sccm.

Table 2.1. Catalyst densities, averaged tube outer diameters, mass densities and volume fractions of CNT arrays corresponding to growth conditions.

| Al ₂ O ₃ | Sputtered | Sputtered | Sputtered | Sputtered | ALD |
|---|----------------------|----------------------|----------------------|----------------------|----------------------|
| H ₂ (sccm) | 80 | 80 | 80 | 110 | 110 |
| Annealed (min.) | 7 | 2 | 0 | 0 | 0 |
| Catalyst Density (cm ⁻²) | 2.4x10 ¹⁰ | 4.8x10 ¹⁰ | 5.4x10 ¹⁰ | 7.8x10 ¹⁰ | 9.8x10 ¹⁰ |
| Tube outer diameter (nm) | 5.92±1.38 | 5.00±0.67 | 5.14±0.63 | 5.75±1.09 | 5.46±0.63 |
| CNT array mass density (g/cm ³) | 0.018±0.003 | 0.023±0.005 | 0.035±0.007 | 0.036±0.004 | 0.039±0.003 |
| CNT array volume fraction (%) | 0.87±0.15 | 1.10±0.25 | 1.68±0.34 | 1.73±0.19 | 1.84±0.14 |

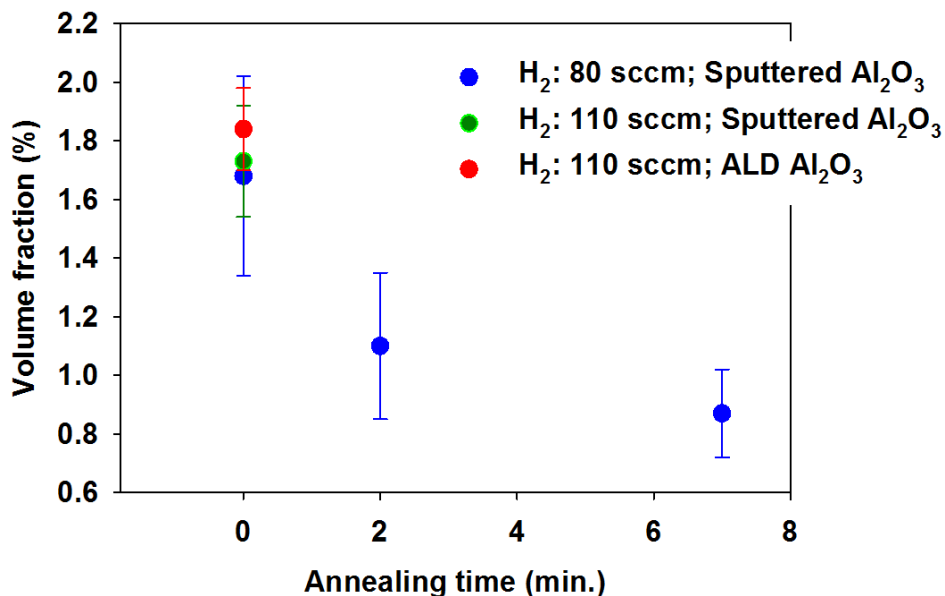


Figure 2.9. The CNT array volume fraction measured as a function of annealing duration. The volume fraction increases as the annealing duration decreases and reaches to maximum by increasing the H₂ flow rate to 110 sccm with ALD Al₂O₃ support layer.

2.3 Carbon Nanotube Array Length Control

To control the length of CNT arrays with a constant volume fraction, an optimized H₂ flow rate should be determined by measuring the volume fraction and length of CNT array as a function of H₂ flow rate. The H₂ flow rate increases from 80 sccm to 250 sccm. The annealing duration keeps at 0 minute, the growth time keeps at 4 minutes, and the flow rates of C₂H₄/H₂O/Ar keep at 120 sccm/100 ppm/ 100 sccm. As shown in Figure 2.10, the volume fraction of the CNT array increases from 0.7% to 1.2% as the H₂ flow rate increases from 80 sccm to 110 sccm while further increase of H₂ flow rate causes a drop of volume fraction; the volume fraction sharply decreases from 1.2% to 0.47% as the H₂ flow rate increases from 110 sccm to 130 sccm and slowly decreases from 0.47% to 0.44% as the H₂ flow rate increases from 130 sccm to 250 sccm. It has been shown in Figure 2.7 and Figure 2.8 that the increase of H₂ flow rate from 80 sccm to 120 sccm causes an increase of the catalyst density, which indicates that the drop of volume fraction of CNT array by further increasing the H₂ flow rate is possibly due to the drop in catalyst density. To explain this, H₂ has the ability to transform oxidized iron thin film to iron catalyst particles, however, exceeding amount of H₂ could possibly causes higher sintering rate of the catalyst particles which results in the drop of the number of catalyst. It is also interesting to measure the CNT array length as a function of H₂ flow rate. In Figure 2.10, the length of the CNT array keeps at ~ 190 μm as the H₂ flow rate increases from 80 sccm to 110 sccm, while the array length drops monotonically from 190 μm to 90 μm as the H₂ flow rate increases from 110 sccm to 250 sccm. Since it is possible that the coarsening rate of catalyst particles increases as H₂ increases to certain amount of flow rate, there are more catalysts disappearing, and the growth of CNTs is limited by the disappearing catalyst which results in a decrease of CNT array length.

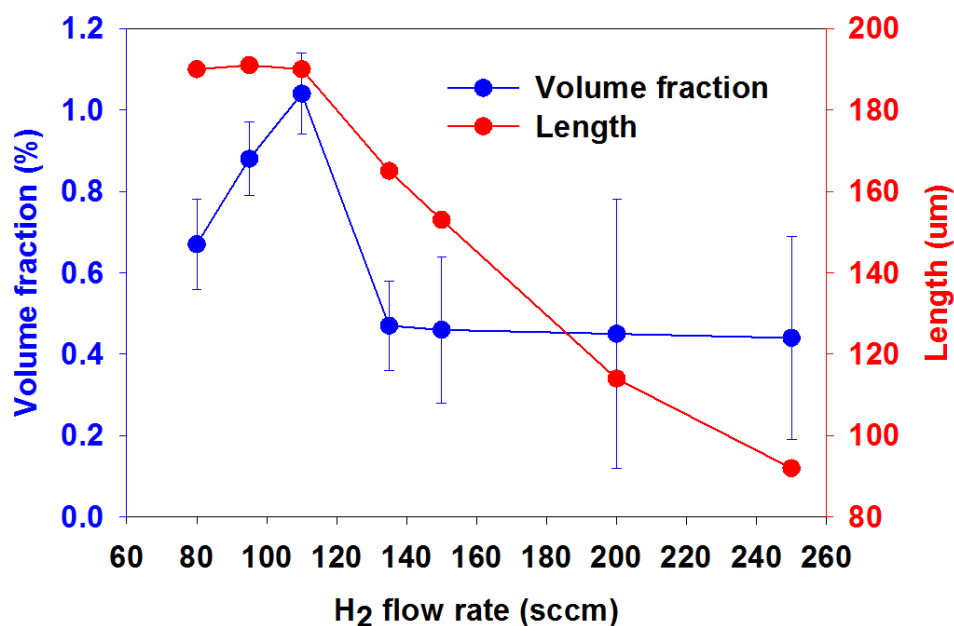


Figure 2.10. Volume fraction and length of CNT array measured as a function of H₂ flow rate.

The length of a CNT array is controlled by the exposure time of C₂H₄. The annealing duration is kept at 0 minute with the flow rates of C₂H₄/H₂/H₂O/Ar at 120 sccm/110 sccm/100 ppm/ 100 sccm. As shown in Figure 2.11, the length of the CNT array increases close to linearly with a growth rate ~96.7 μm/minute. To test whether the CNT array density is stable, the volume fraction of CNT array is also measured as a function of growth time. As shown in Figure 2.12, the volume fraction of CNT array keeps at ~ 2% as the growth time increases. This indicates that water-assisted CVD method is able to create a stable growth at the certain annealing duration and H₂ flow rate. Such stable growth of the CNT array is possibly due to the long catalyst lifetime and constant number of catalyst density.

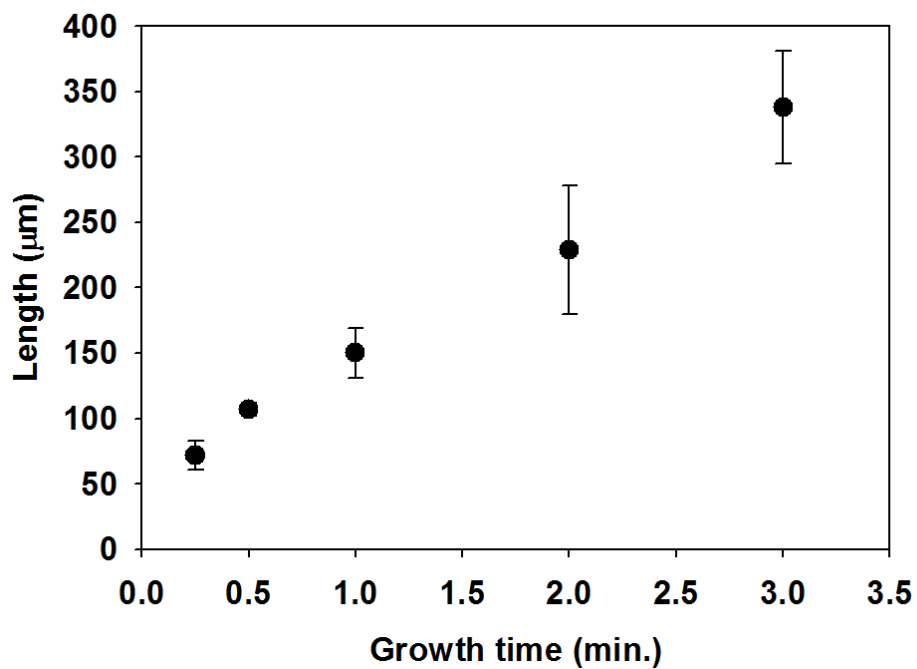


Figure 2.11. The length of CNT array measured as a function of growth time.

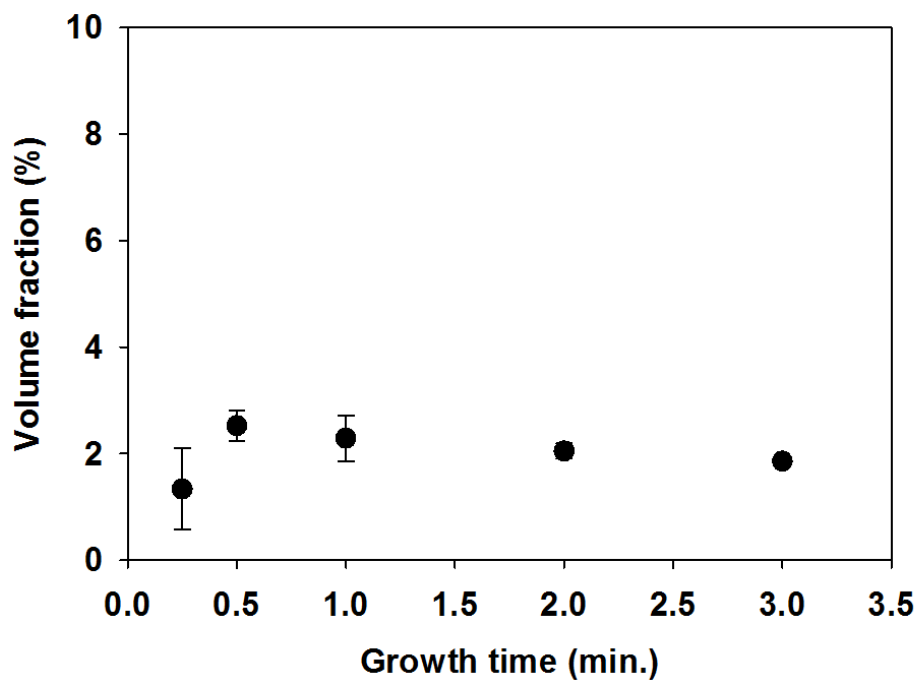


Figure 2.12. The volume fraction of CNT array measured as a function of growth time.

2.4 Summary

This work shows that varying the annealing duration using water-assisted CVD method tunes the catalyst particle density which controls the mass density of CNT array. The density of catalysts increases as the annealing duration decreases while the tube diameter is not affected by the annealing duration. The constant tube diameter is possibly due the reduction of Ostwald ripening by water vapor, and the decrease of number of catalyst density is possibly due to the evaporation of smaller catalyst particles over the time. The greater the catalyst particle density, the higher the mass density of CNT array. And due to the constant tube diameter of the CNT array, the volume fraction of CNT array increases proportionally with the mass density of CNT array. The highest volume fraction of CNT array is at 0 annealing duration. Further enhancement of CNT array volume fraction was achieved by changing the deposition method of Al_2O_3 into ALD and increasing the H_2 flow rate from 80 sccm to 120 sccm.

Investigation on the effect of H_2 was achieved by measuring the length and the volume fraction of CNT array as a function of H_2 flow rate. Both the CNT-array volume fraction and the length drop as the H_2 flow rate increases to more than 120 sccm. Such decrease of length and volume fraction could have resulted from the Ostwald ripening of catalyst. The length of a CNT array was controlled by the exposure time of C_2H_4 with constant H_2 flow rate: 120 sccm. A linear increasing trend is found with the increase of the C_2H_4 exposure time, and the growth rate is $\sim 96 \mu\text{m}/\text{minute}$. The volume fraction of a CNT array is not affected by the C_2H_4 exposure time, which means length control of CNT array with constant density can be conducted under an optimized H_2 flow rate.

3 Experimental Technique for Thermal Characterization of Carbon Nanotube Array

The experimental technique used for measuring the thermal properties of CNT array is discussed in this chapter. As a thermal interface material, CNT arrays and the contact surfaces form a multilayer structure, and thermal characterization on such structure is a challenging task. To simplify the problem, one can consider each layer, including the CNT array, as a film material. However, in electronic packaging, the cross-plane surface roughness of each component is on the order of $0.1 \mu\text{m}^{68}$ which makes the thickness of interface materials to be as thin as $0.1 \mu\text{m}$. In this case, thermal characterization of thin-film materials becomes a challenging issue. In the first part of this chapter, the principles of several thin-film thermal measurement techniques are described, giving the reason for choosing phase sensitive photo thermal reflectance thermometry as the main measurement technique. In the second part of the chapter, the principle of phase sensitive photo thermal reflectance thermometry is introduced, the experimental setup and sample preparation are discussed. In the last section, the extraction of thermal properties from the phase signal is explained based on the heat conduction model, and finally, the thermal measurement results for a bench mark case and for a carbon nanotube array are illustrated.

3.1 Thermal Measurement Technique for Thin-Film Materials

Thermal measurement of the cross-plane thermal properties of a thin film and of the contact conductance between multiple thin films structure remain challenging tasks. Direct measurement on the thermal conductivity across the film requires the determination of the absolute value of heat flux and the temperature profile across the film according to Fourier's law,

$$\dot{q}'' = k \frac{|\Delta T|}{|\Delta z|}. \quad (3.1)$$

The thickness across the thin film usually varies from several nanometers to several micrometers. The absolute amount of temperature difference across such small distance is difficult to detect. For a generated heat flux of 2 MW/m^2 , and a $0.1\text{-}\mu\text{m}$ film with thermal conductivity of 200 W/m-K , the absolute temperature difference across the film is only 0.001 K . Such temperature difference is much smaller than the resolution of the temperature detector used in DC heating system such as thermal couples and infrared camera ($\sim 0.1 \text{ K}$).^{13,69} Another issue is the heat loss to the surrounding, which makes it difficult to measure the actual amount of heat.

Instead of applying DC heat source and measuring the absolute amount of heat and the absolute temperature in space domain, one can apply a pulsed heat source at the sample surface and measure the temperature change at the sample surface in time domain. Photo thermal reflectance thermometry uses a high-power pump laser to generate the pulsed heat source and a low-power probe laser to detect the temperature at the surface, this technique is based on the temperature dependence of reflectivity. The experiments can be performed at room temperature in the atmosphere. The temperature of the whole sample changes due to the heat absorption

which causes modulation in the intensity of the reflected probe beam. The sample surface is often coated with a thin metal layer to increase the intensity of the reflected probe beam. It has been experimentally shown that the reflectivity of metal is linearly proportional to temperature,⁷⁰

$$R(T) \propto C_{TR} R_0 T \quad (3.2)$$

where R_0 is the reflectivity at the reference temperature, and C_{TR} is the coefficient of thermal reflectance which is approximately constant for most metal $\sim 10^{-5} \text{ K}^{-1}$.⁷⁰ The temperature is linearly proportional to the intensity of the reflected probe beam according to equation (3.2),

$$I_{\text{reflected_probe}} = I_{\text{incident_probe}} R(T) \propto I_{\text{incident_probe}} C_{TR} R_0 T \quad (3.3)$$

where $I_{\text{incident_probe}}$ is the intensity of the incident probe beam which is a constant.

In the diffusion region, measurement of the thermal properties of thin films is conducted using a nanosecond pump laser, and the amplitude decay of the temporal temperature response is measured as a function of time in the microsecond region. For most materials, a microsecond time scale is in the diffusion region where Fourier's law is applicable. The thermal properties can be extracted by solving the amplitude decay from the heat conduction model and fitting with the measured amplitude decay of the probe beam intensity. Since the temperature response is measured as a function of time, this technique is also called time-domain photo thermal reflectance thermometry. However, the significant drawback of this technique is that the heating source generated by the nanosecond pump laser is too high in power⁴⁹ which can result in the melting of metal films.

Similar to the time-domain photo thermal reflectance thermometry, frequency-domain photo thermal reflectance thermometry is based on the linear temperature dependence of reflectivity; however, the technique uses a continuous wave pump laser as heat source. The continuous wave pump laser is modulated at low frequency, $\sim 100 \text{ Hz}$ - 10000 Hz , and thus the heat source has lower power compared to the nanosecond pump laser. The thermal properties of the CNT array are measured via frequency-domain Photo Thermal Reflectance Thermometry in this dissertation. In the next section, more details of this technique will be described.

3.2 Phase Sensitive Photo Thermal Reflectance Thermometry

The frequency-domain photo thermal reflectance thermometry is often called phase sensitive photo thermal reflectance thermometry since it uses the phase difference between the intensity of the reflected probe beam and the intensity of the pump beam to extract the thermal properties. As shown in Figure 3.1, the pump intensity is a wave function oscillating at the modulation frequency and the reflected probe intensity is also a wave function oscillating at the same frequency while having a phase lag and amplitude decay compared to the pump intensity.

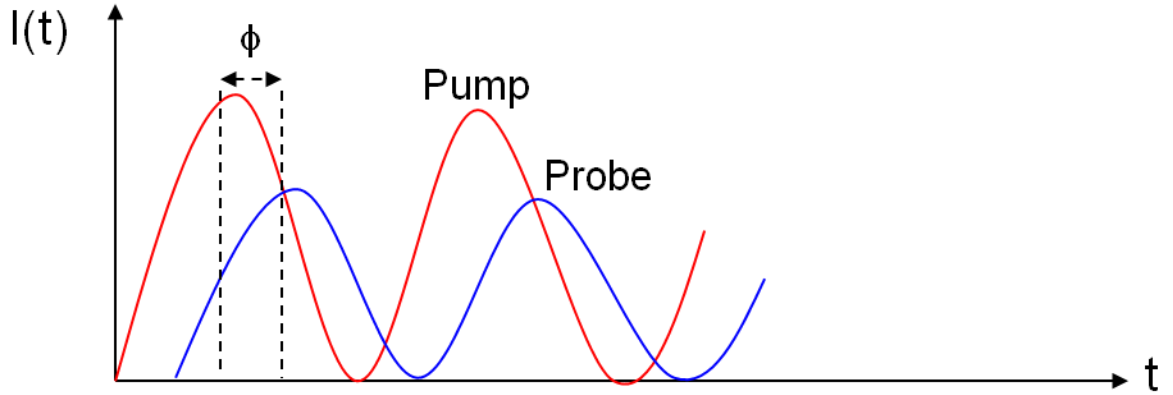


Figure 3.1. Schematic diagram of pump and probe beam intensity plotted as a function of time.

Such phase lag and amplitude decay of the reflected probe intensity is due to the thermal inertia of the material, which is a function of thermal properties of the sample. To explain this, one can regard the correlation between the pump and the reflected probe intensity to the correlation between the heating source and the temperature. Assume that the oscillatory component of the pump intensity is a wave function at frequency ω with amplitude A ,

$$I_{pump}(t) = A \exp(-i\omega t), \quad (3.4)$$

and that the reflected probe intensity is another wave function oscillating at frequency ω with amplitude B but with a phase lag compare to the pump intensity,

$$I_{reflected_probe}(t) = B \exp(-i(\omega t - phase)), \quad (3.5)$$

the heating source Q is the intensity of the incident pump beam times the absorptivity at the sample surface,

$$Q(t) = \alpha I_{pump}(t) = \alpha A \exp(-i\omega t). \quad (3.6)$$

The temperature can be linearly transformed from the reflected intensity of the probe beam according to equation (3.3),

$$T(t) \propto (I_{incident_probe} C_{TR} R_0)^{-1} I_{reflected_probe} = C \exp(-i(\omega t - phase)) \quad (3.7)$$

where C is the amplitude of the wave function. The above equation indicates that the temperature wave has the same phase lag relates to the heating wave as the phase lag of probe intensity relates to the pump intensity. One can extract the thermal properties purely from the phase lag by building a heat conduction model and fitting the phase solved from the model to the measured phase.

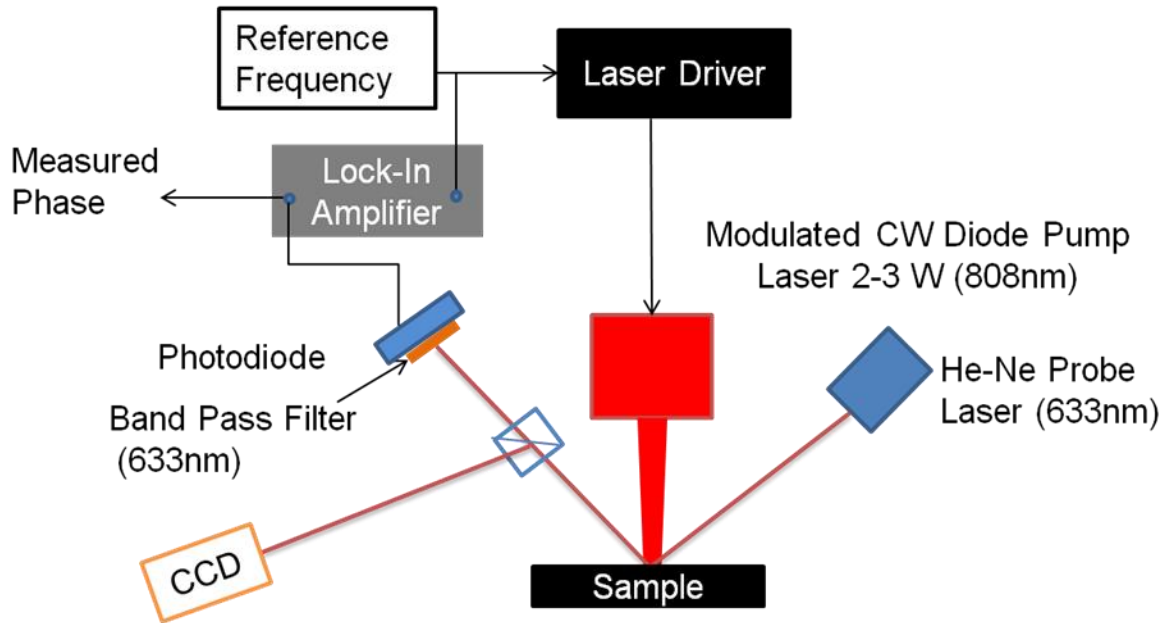


Figure 3.2. Schematic of the experimental setup of Phase Sensitive Photo Thermal Reflectance Thermometry.

The thermal measurement is conducted under atmosphere at room temperature. The experimental setup of Phase Sensitive Photo Thermal Reflectance Thermometry is shown in Figure 3.2. The system includes a high power diode pump laser (RPMC, LDX-3315-808 with wave length 808 nm and output power up to 3 W) acting as a heating source and a low power probe laser (HeNe laser with wavelength 632.8 nm and output power 5 mW) acting as the temperature detector. The pump and probe beam are concentrically focused onto the top of the sample surface. A function generator sends a modulation frequency to the driver of pump laser. The photo diode measures the intensity of the reflected probe beam and translates the photo signal into electrical signal to a lock-in amplifier which measures the phase lag and amplitude at the modulation frequency. A beam splitter is used to send the reflected image on the sample surface to a CCD camera. The CCD camera is used to ensure the alignment of the pump and probe laser spot and to measure the spot size. The diameter of the pump and probe beam spots are measured approximately to be 1 mm and 200 μm (as shown in Figure 3.3).

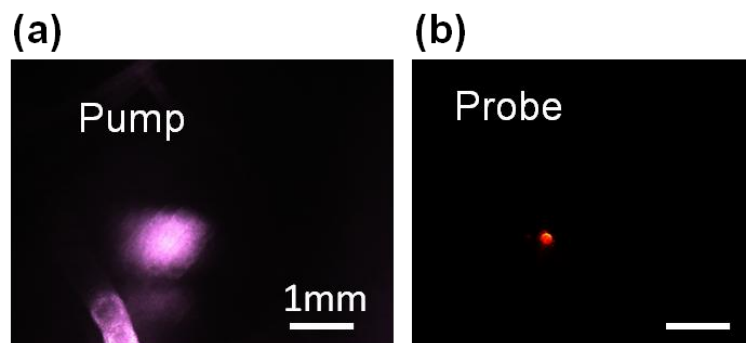


Figure 3.3. The image of the (a) pump and (b) probe beam spots under CCD camera.

Before building the heat conduction model, one needs to determine whether the heat conduction system is close to one dimensional or three dimensional. Since the heating source is a wave function, the temperature is also a wave function. However, the amplitude of the temperature wave has an exponential decay over a distance.⁴⁹ Thermal penetration depth is defined to be the distance for the amplitude of temperature wave decays to e^{-1} of the initial amplitude.⁷¹ The thermal penetration depth is a function of thermal diffusivity, α , and the modulation frequency, ω , it can be expressed as⁷²

$$L_p = \sqrt{\frac{2\alpha}{\omega}}. \quad (3.8)$$

It has been experimentally shown that the heat conduction system with an oscillating heating source depends strongly on the spot size of the pump beam relative to the thermal penetration depth.⁷² As shown in Figure 3.4, when the thermal penetration depth, L_p , is much larger than the radius of the pump beam, r_{pump} , the heat conduction system is close to 3 dimensional. In this case, one needs to consider if there is any temperature change along the radial direction when the probe beam is not perfectly aligned with the pump beam. When L_p is much smaller than r_{pump} , the system is close to 1 dimensional, and one only needs to solve the temperature along cross-plane direction. Since it is more significant to find out the thermal properties along cross-plane direction for TIMs, building a 1 dimensional heat conduction model can simplify the problem and reduce the unknown parameters such as the anisotropic ratio of the material. One can determine the frequency range for using one dimensional heat conduction model according to equation (3.8), where the higher the frequency, the closer the heat conduction system to be one dimensional.

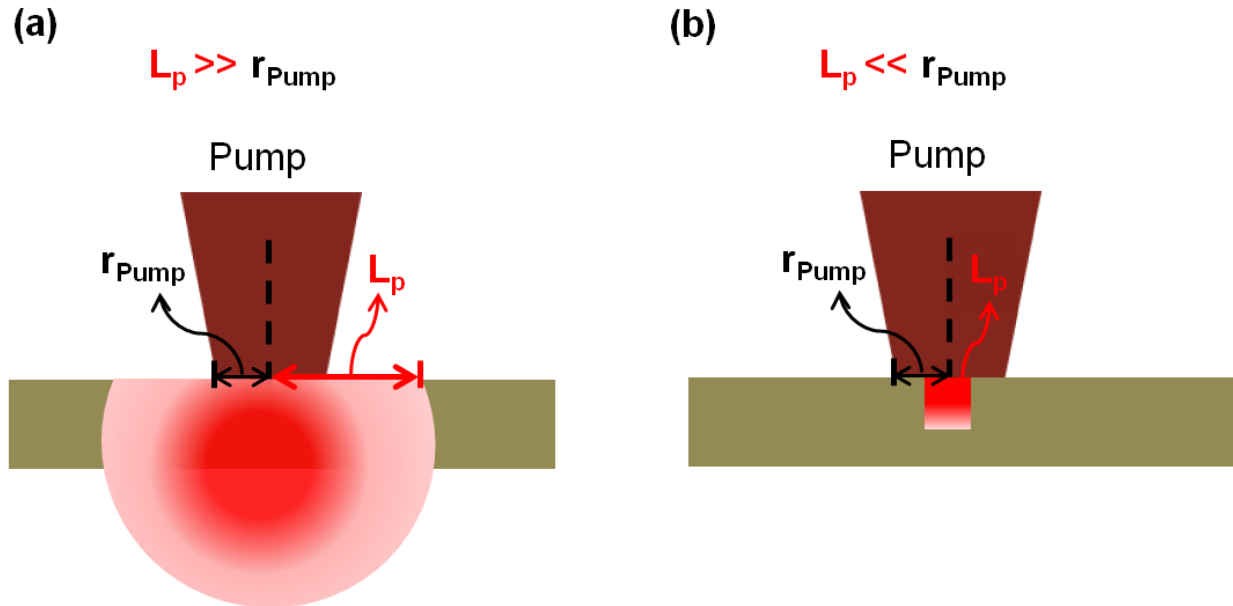


Figure 3.4. Schematic of the heat conduction system estimated by the pump beam radius, r_{pump} , and the thermal penetration depth, L_p . The heat conduction system is close to (a) 3 dimensional when $r_{pump} \ll L_p$, and (b) 1 dimensional when $r_{pump} \gg L_p$.

The sample configuration is also a significant factor in determining whether the system is measuring the thermal properties of the film. The sample configuration also determines the measurable frequency range, which indirectly determines the dimensionality of the heat conduction system. If the film is a porous structure like a CNT array, one needs to apply a flat substrate on top of the film for better reflection. As shown in Figure 3.5 (a), when the pump and probe beams are focused on top of the substrate, the thermal penetration depth may reach only within the substrate at the higher frequency range; in this case, the temperature wave does not reach to the film so that one cannot measure the thermal properties of the film. One can solve this problem by moving the pump and probe beams to the bottom of the substrate as shown in Figure 3.5 (b); in this case, the thermal penetration depth has higher chance to penetrate the film even at high frequency region so that the thermal properties of the film can be measured as a one-dimensional heating system. In the next section, measurements on the thermal properties are described based on the sample configuration in Figure 3.5 (b).

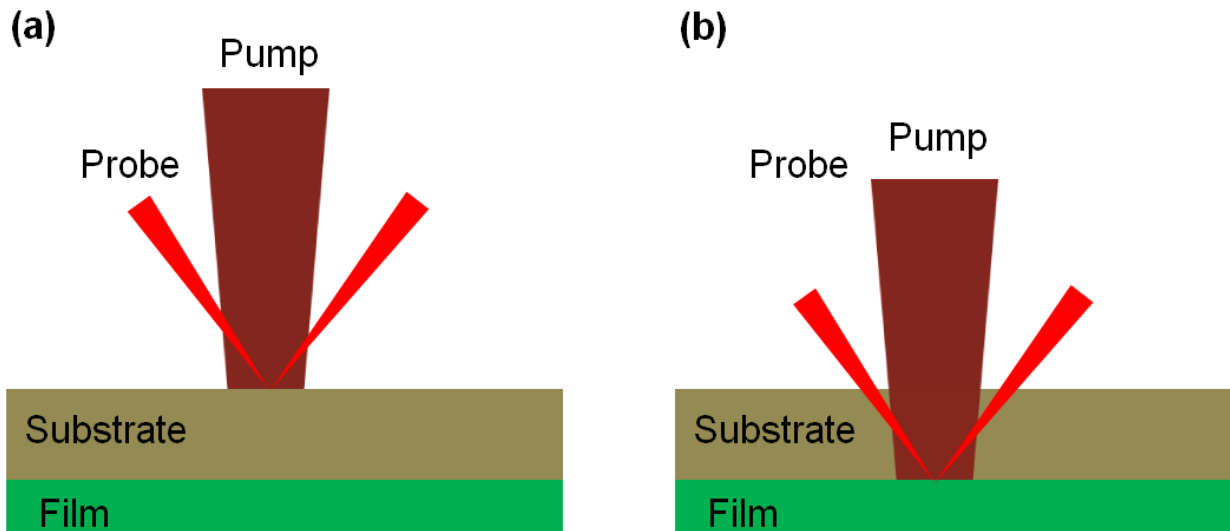


Figure 3.5. Schematic illustration of two kinds of sample substrates resulting in different pump and probe beam paths. (a) The substrate is opaque, and the pump and probe beams can only be focused on top of the substrate. (b) The substrate is transparent and the pump and probe beams penetrate through the substrate and focused on top of the film.

3.3 Thermal Properties Measurement

The 500- μm thick glass substrate is first tested as the benchmark case to verify the measurement system. As shown in Figure 3.6, two thin metal layers, 10-nm Cr and 150-nm Au, are sequentially thermally evaporated at the bottom of the glass substrate. The pump and probe beams are concentrically focused on the metal layers, where the Au film is used as the reflective layer and the Cr film is used as both an absorptive layer and an adhesion layer.

The thermal penetration depth of glass is estimated to be much smaller than the pump beam radius for frequencies higher than 1000 Hz. The pump beam radius is 500 μm . According

to equation 3.8, the thermal penetration depth of glass is $\sim 26 \mu\text{m}$ at 1000 Hz with thermal diffusivity of glass of $3.4 \times 10^{-7} \text{ m}^2/\text{s}$. Therefore, the heat conduction system is close to one-dimensional above 1000 Hz. The frequency of the pump beam is modulated from 200 Hz- 20000 Hz, the upper bound of the modulation frequency is determined by the smallest detectable signal of the reflected probe beam.

A one dimensional transient heat conduction model is used for the sample structure in Figure 3.6. The thickness of the glass is b_{Glass} . The pump beam generates an oscillating heating source at $z_{\text{Glass}}=0$, and the probe beam detects the temperature also at $z_{\text{Glass}}=0$. Since the Cr-Au metal layer is much thinner than the glass layer, the sample structure is considered to be one layer. The governing equation is

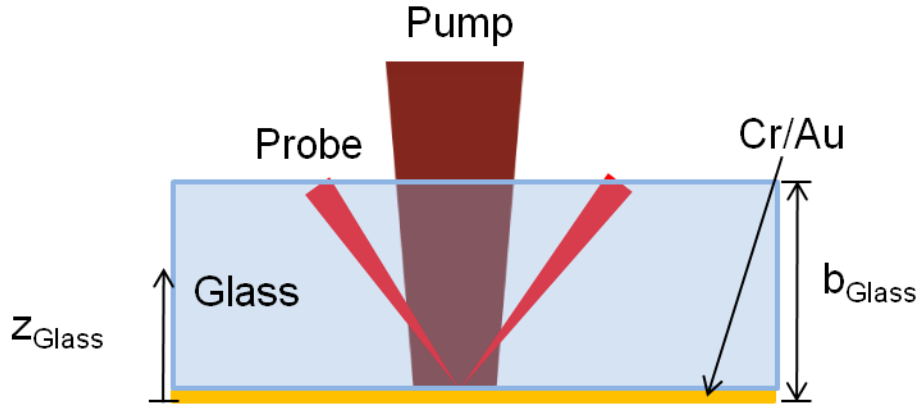


Figure 3.6. Schematic of the heat conduction model for the glass substrate.

$$\frac{\partial T_{\text{Glass}}(z_{\text{Glass}}, t)}{\partial t} = \frac{k_{\text{Glass}}}{C_{\text{Glass}}} \frac{\partial^2 T_{\text{Glass}}(z_{\text{Glass}}, t)}{\partial z_{\text{Glass}}^2} \quad (3.9)$$

where T , k , and C represent temperature, thermal conductivity, and the volumetric heat capacity of glass, respectively. If the heating source is a wave function oscillating at frequency ω with an amplitude of uniform heat flux, q'' , the boundary condition at $z_{\text{Glass}}=0$ is

$$q'' \exp(-i\omega t) = -k_{\text{Glass}} \left. \frac{\partial T_{\text{Glass}}}{\partial z_{\text{Glass}}} \right|_{z_{\text{Glass}}=0} \quad (3.10)$$

Assume that at $z_{\text{Glass}}=b_{\text{Glass}}$, the boundary is thermally insulating,

$$\left. \frac{\partial T_{\text{Glass}}}{\partial z_{\text{Glass}}} \right|_{z_{\text{Glass}}=b_{\text{Glass}}} = 0, \quad (3.11)$$

The temperature at $z_{\text{Glass}}=0$ can be solved from the above governing equation and the boundary conditions

$$T_{Glass}(0,t) = \frac{q'' L_p}{\sqrt{2k_{Glass}}} \exp(-i(\omega t - \frac{\pi}{4})) . \quad (3.12)$$

The temperature solution indicates that the phase lag is 45 degree at $z_{Glass}=0$, and the phase lag is independent to ω and the thermal properties of glass.

The measured phase response and the phase lag solved from the heat conduction model are plotted as a function of frequency in Figure 3.7. The measured phase response is 1-2 degrees off from 45 degrees before 15000 Hz. To explain this, it is possible that the thermal penetration depth, L_p , is dominated by the thermal penetration depth of Au along the radial direction. According to equation (3.8), the thermal penetration depth of Au is around 130 μm at 15000 Hz with thermal diffusivity of Au $1.27 \times 10^{-4} \text{ m}^2/\text{s}$, which is not yet an order of magnitude smaller than the radius of pump beam, 500 μm . In the 3 dimensional heat conduction system, the phase lag could be off from 45 degrees if the heating beam is not uniform and if there is any misalignment of probe and pump beam.⁴⁷

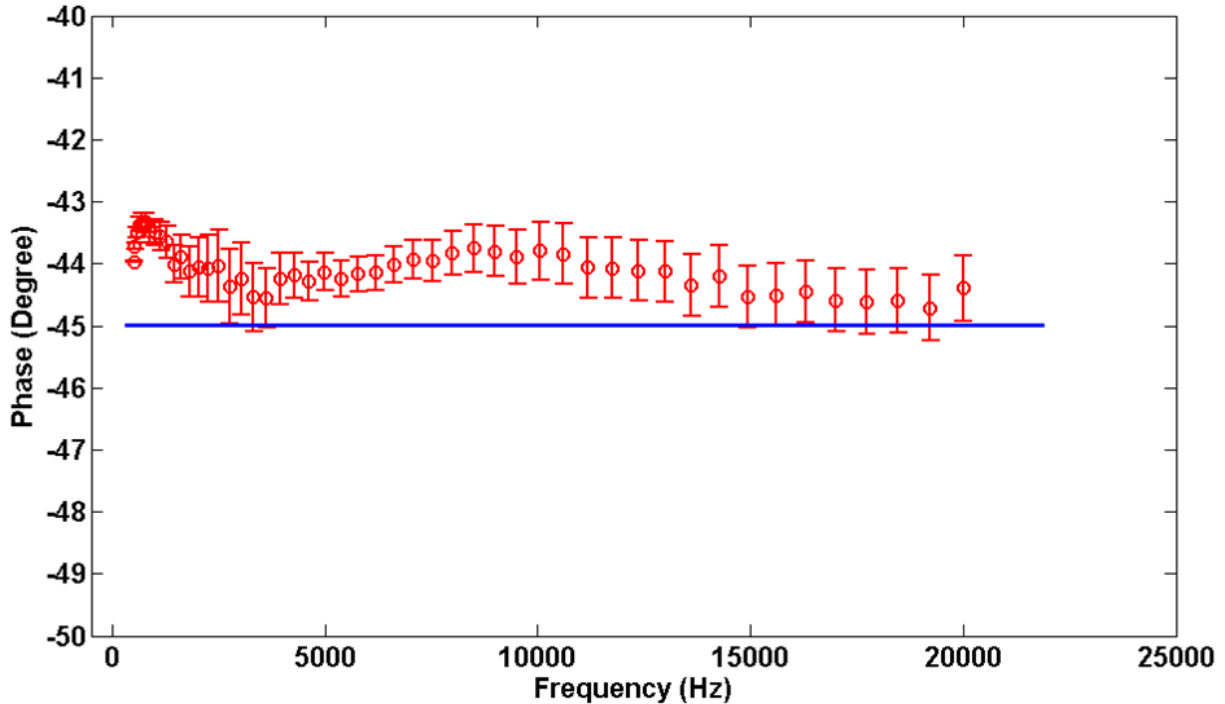


Figure 3.7. Phase response (circles) of the glass sample and the phase solution calculated from the heat conduction model (solid line).

To measure the cross-plane thermal conductivity of a CNT array and the contact conductance between the CNT array and the glass substrate, the test sample is prepared by bonding the free-ends of a 100- μm thick CNT array to a piece of 500- μm thick glass using ~2- μm thick In film as a bonding material. Both the free ends of the CNT array and the bonding side of the glass are sequentially coated with a 10-nm thick Cr film followed by a 150-nm thick Au film. The Cr and Au on the CNTs are used as adhesion layers, and the Cr and Au on glass are used as both heat absorption and thermal reflectance layer. The In film is deposited on the Cr-Au

coated glass substrate. The substrate is heated to 350°C, and the CNT array with Cr-Au coated on the CNTs tips is bonded to Cr-Au-In coated glass under a nominal compressive stress of 196 kPa; the nominal compressive stress is calculated using a loading of 19.6 N divided by the CNT-array apparent area of 1 cm². The Si substrate is then removed from the CNT growth ends after the bonding process in order to focus on measuring the CNT array cross-plane thermal conductivity and the CNT array-glass contact conductance. The Glass-In-CNT array three-layer structure along with the pump and probe beam paths are shown in Figure 3.8, where the glass is considered as the first layer, Cr-Au-In is considered as the second layer, and Cr-Au-CNT array is considered as the third layer. Since the thickness of Cr and Au is much smaller than the thickness of glass, In, and CNT array, it is assumed that Cr and Au layers are negligible.

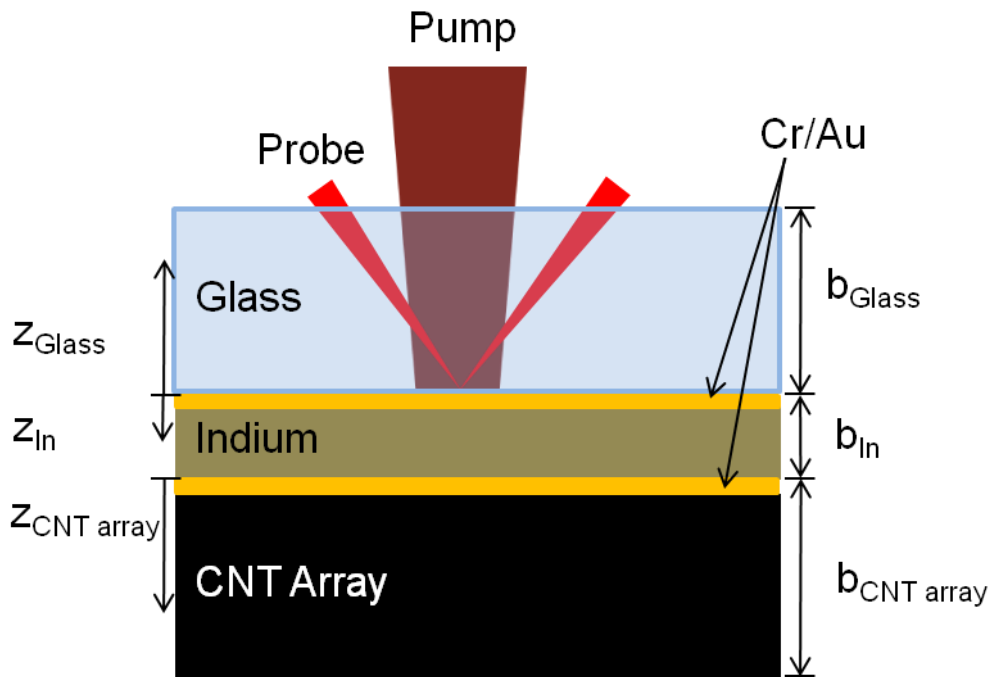


Figure 3.8. Schematic of the heat conduction model for the glass-indium-CNT array three-layer structure.

A three-layer transient heat conduction model is used to obtain the thermal properties according to the sample structure in Figure 3.8. The temperature variation is assumed to be 1 dimensional with the assumption of uniformly distributed heating beam and with the estimation of a larger pump-beam radius compared to the thermal penetration depth propagating through the sample structure. Since the length of In, 2µm, is much smaller than the thermal penetration depth of In at 20000 Hz, ~69 µm, the thermal wave reaches the CNT array, and the thermal penetration depth is determined by the diffusivity of the CNT array,

$$L_p = \sqrt{\frac{2\alpha_{CNTarray}}{\omega}} \quad (3.13)$$

where $\alpha_{CNT\ array}$ is the thermal diffusivity of CNT array which is reported to be $\sim 6 \times 10^{-4} \text{ m}^2/\text{s}$,⁴⁷ then L_p is $\sim 300 \text{ }\mu\text{m}$ at 10000 Hz which is slightly smaller than the r_{pump} . The governing equation for the three layer structure is

$$\frac{\partial T_j(z_j, t)}{\partial t} = \frac{k_j}{C_j} \frac{\partial^2 T_j(z_j, t)}{\partial z_j^2} \quad (3.14)$$

where T_j , k_j , and C_j represent temperature, thermal conductivity, and volumetric heat capacity of j^{th} layer, and the subscript j represents glass, in, and CNT array layers. The boundary conditions are:

$$-k_{Glass} \left. \frac{\partial T_{Glass}}{\partial z_{Glass}} \right|_{z_{Glass}=0} = G_{Glass-In} (T_{In}(0) - T_{Glass}(0)) \quad (3.15)$$

$$q'' \exp(-i\omega t) = -k_{In} \left. \frac{\partial T_{In}}{\partial z_{In}} \right|_{z_{In}=0} + G_{Glass-In} (T_{In}(0) - T_{Glass}(0)) \quad (3.16)$$

$$-k_{In} \left. \frac{\partial T_{In}}{\partial z_{In}} \right|_{z_{In}=b_{In}} = G_{In-CNTarray} (T_{In}(b_{In}) - T_{CNTarray}(0)) = -k_{CNTarray} \left. \frac{\partial T_{CNTarray}}{\partial z_{CNTarray}} \right|_{z_{CNTarray}=0} \quad (3.17)$$

$$\left. \frac{\partial T_{Glass}}{\partial z_{Glass}} \right|_{z_{Glass}=b_{Glass}} = 0; \quad \left. \frac{\partial T_{CNTarray}}{\partial z_{CNTarray}} \right|_{z_{CNTarray}=b_{CNTarray}} = 0 \quad (3.18)$$

where G represents contact conductance and b represents length. The temperature at $z_{In}=0$ can be analytically solved as a complex number which is a function of t and simply written as

$$T_{In}(0, t) = |T_{In}| \exp[-i(\omega t - \theta)] \quad (3.19)$$

where θ is the phase lag, and

$$\theta = f(\omega, k_j, C_j, b_j, G_{Glass-In}, G_{In-CNTarray}) \quad (3.20)$$

θ is plotted against ω to fit with the measured phase response. More details of the derivation of temperature can be found in Appendix A. Table 3.1 lists the length, b , the thermal conductivity, k , and the volumetric heat capacity, C , of each layer, where the length of each layer is referred from the thickness in sample preparation, and the thermal conductivity and volumetric heat capacity of glass and indium are well known.

Table 3.1. The length, the thermal conductivity, and the volumetric heat capacity of each layer.

| | b (μm) | k (W/m-K) | C ($\text{kJ/m}^3\text{-K}$) |
|-----------|-----------------------|--------------|----------------------------------|
| Glass | 500 | 1.4 | 1625.0 |
| In | ~ 2 | 82 | 1708.3 |
| CNT array | ~ 100 | undetermined | undetermined |

There are several undetermined parameters in the phase function which are: $G_{\text{Glass-In}}$, $G_{\text{In-CNT array}}$, $C_{\text{CNT array}}$, $k_{\text{CNT array}}$, b_{In} and $b_{\text{CNT array}}$. $G_{\text{Glass-In}}$ can be set at 10^8 W/m²-K according to the reported dielectric-metal thermal contact conductance;⁷³ $C_{\text{CNT array}}$ is

$$C_{\text{CNT array}} = \phi_{\text{CNT array}} \rho_{\text{CNT}} C_{p_CNT} \quad (3.21)$$

where $\phi_{\text{CNT array}}$ is the volume fraction of the CNT array, ρ_{CNT} is the mass density of an individual multi-walled CNT, and C_{p_CNT} is the heat capacity of an individual multi-walled CNT. $\phi_{\text{CNT array}}$ is estimated to be 1.1% since the CNT array was grown with a batch of samples measured ~ 100 μm in length and 1.1% in volume fraction; ρ_{CNT} and C_{p_CNT} are set to be 2.1 g/cm³ and 700 J/kg-K according to the literature data;^{67,74} thus, $C_{\text{CNT array}}$ is 16.2 kJ/m³-K; $b_{\text{CNT array}}$ is put into fitting parameter since the length of the CNT array may vary within the sample; b_{In} is also put into the fitting parameter, although the length of In film, b_{In} , is initially 2 μm , it could decrease after the bonding process. Summarized from the above description, the four undetermined parameters are $G_{\text{In-CNT array}}$, $k_{\text{CNT array}}$, $b_{\text{CNT array}}$, and b_{In} . Figure 3.9 shows the measured phase responses (circles) and the corresponding best fit solution (solid line).

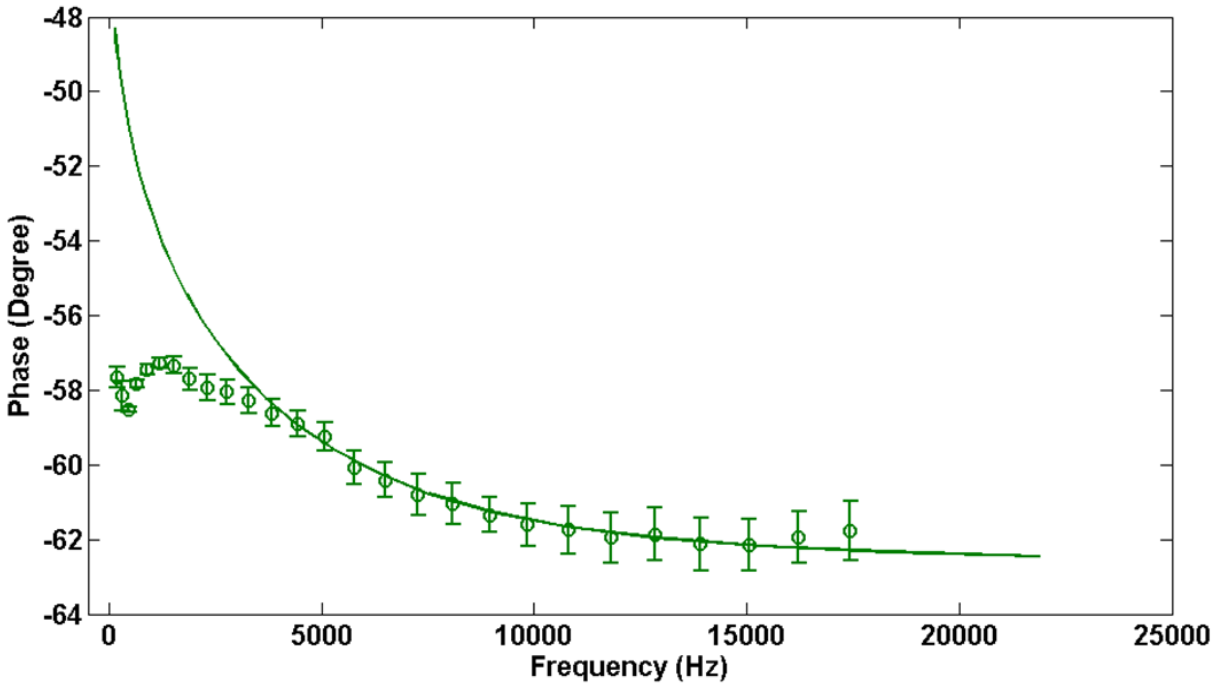


Figure 3.9. Phase response (circles) of the glass-indium-CNT array, three-layer structure and the corresponding best-fit solution solved from the heat conduction model (solid line).

The mismatches between the best-fit solution and the phase response in the low-frequency region ($\omega < 5000$ Hz) may be due to the non-uniformity of the heating beam and certain degree of misalignment between the pump and probe beams. However, the solutions fit well to the measured phase responses in high frequency region ($\omega \geq 5000$ Hz) which provides a range for using 1-D heat conduction model. The parameters of the best fit solution are listed in Table 3.2. The error bar of each parameter is expressed as

$$\Delta\beta = \sqrt{\sum_i \left[\left(\frac{\partial\theta}{\partial\beta} \right)_i^{-1} \Delta\theta_i \right]^2} \quad (3.22)$$

where β is the parameter, and $\Delta\theta$ is the error bar of the measured phase data point, the subscript i indicates the data point at certain ω ; note that the calculation of error bar only applies for the data point at $\omega \geq 5000$ Hz. Here, we only show the error bars of $G_{In-CNT\ array}$ and $k_{CNT\ array}$ since they are the two factors affecting the thermal performance.

Table 3.2. The parameters for the best-fit solution solved from the heat conduction model.

| $G_{Glass-In}$ (MW/m ² K) | $k_{CNT\ array}$ (W/mK) | b_{In} (μm) | $b_{CNT\ array}$ (μm) |
|---|----------------------------|-------------------------------|---------------------------------------|
| 1.0 \pm 0.4 | 12 \pm 2 | 1.5 | 90 |

One may argue that $b_{CNT\ array}$ and $\phi_{CNT\ array}$ should be the apparent length and the volume fraction after bonding process; the apparent length of the CNT array could decrease after compression bonding. If the CNT array has the same mass, and if the apparent length decreases in half, the volume fraction of the film should increase by a factor of 2. In this case, the phase lag calculated from the heat conduction model could be changed, and one needs to vary $G_{In-CNT\ array}$ and $k_{CNT\ array}$ in order to fit the data. To verify this argument, the curve fitting is done by cutting down $b_{CNT\ array}$ into 45 μm and increasing $\phi_{CNT\ array}$ into 2.2 %, and the phase lag solved from the heat conduction model does not vary much from the curve shown in Figure 3.9 by fixing the rest of the parameters including the thermal conductivity and the thermal contact conductance (see Figure 3.10). The phase fitting is further verified by decreasing or increasing $b_{CNT\ array}$ several factors and respectively increasing or decreasing $\phi_{CNT\ array}$ the inverse factors.

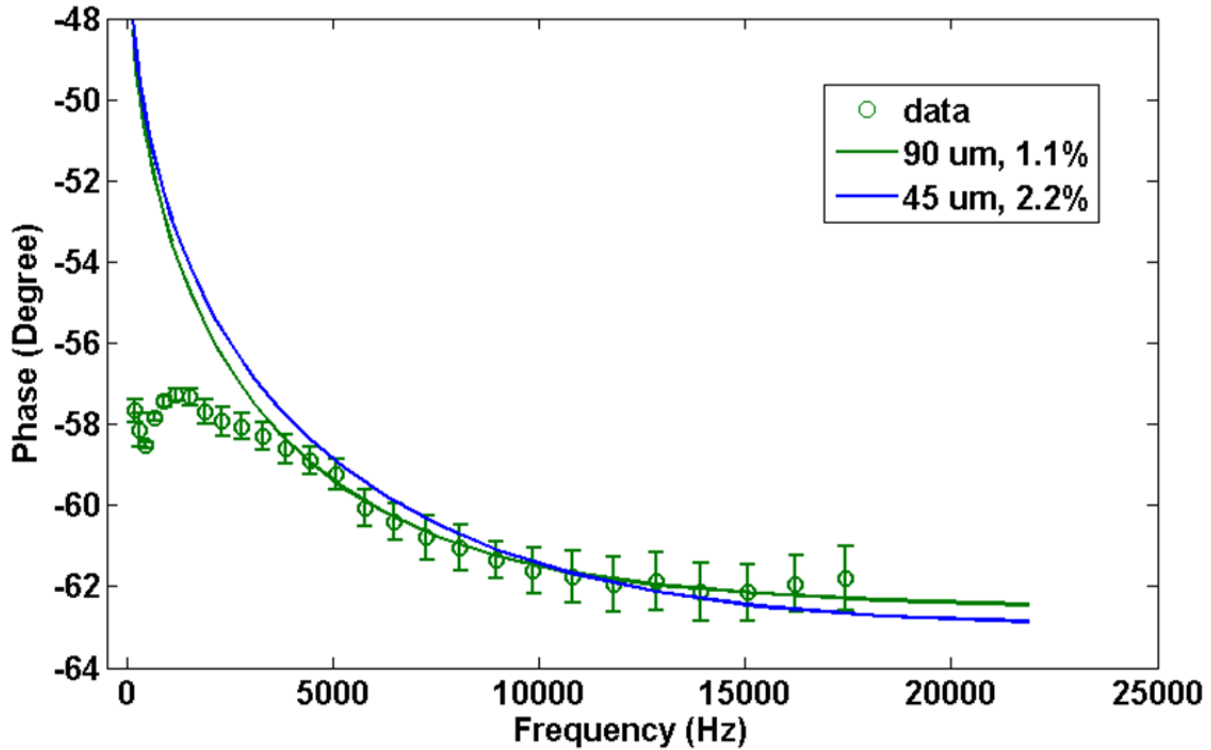


Figure 3.10. Phase response (circles) and the corresponding best-fit solutions with CNT array in 90 microns in length and 1.1% in volume fraction (green solid line) and with CNT array 45 microns in length and 2.2% in volume fraction (blue solid line).

3.4 Summary

In this chapter, the principle of phase sensitive photo thermal reflectance thermometry is described. This technique is based on the linear temperature dependent of reflectivity. The pump beam is used as the heating source and the probe beam is used as the temperature detector. The phase signal detected from the reflected probe beam is used to extract the thermal properties. The thermal properties are extracted by building a heat conduction model. The key factors to determine the dimensionality of the heat conduction system are the size of the pump beam compared to the thermal penetration depth; when the thermal penetration depth is much larger than the pump beam diameter, the system is close to one dimensional heat conduction. To measure the cross-plane thermal conductivity of CNT arrays and the contact conductance between a CNT array and the target substrate, the substrate is chosen to be glass due to its transparent properties, and the glass is coated with Cr and Au film at the boundary attached to CNT array to enhance the reflection of the probe beam and the absorption from the pump beam. The CNT array is attached to the Cr-Au coated glass with an indium film. Both the glass substrate and the glass-indium-CNT array structure are thermally characterized. The two samples have mismatch between the measured phase response and the modeled phase at low frequency region.

4 Thermal Transport Properties and Buckling Behavior of Carbon Nanotube Array

The thermal transport properties of CNT arrays are systematically examined. Firstly, the thermal contact conductance between CNT arrays and the target substrate is measured as a function of the target substrate surface roughness. This is important since the examination can provide a suitable range for the substrate surface roughness used for attaching the CNT array. Secondly, by fixing target substrate to be atomically flat, the thermal conductivity of the CNT array and the CNT array-target substrate thermal contact conductance is measured as a function of array volume fraction and array length. Thirdly, the buckling behavior of CNT arrays is measured systematically as a function of compressive stress. This is important since the buckling behavior may have an effect on the thermal transport properties of CNT array. Finally, the thermal transport properties of CNT arrays are measured systematically as a function of compressive stress. A heat conduction model based on the thermal resistance network is demonstrated to explain the correlation between the thermal transport properties and the buckling behavior of CNT array.

4.1 Effect of Surface Roughness on Thermal Contact Conductance of Copper-Carbon Nanotube Array Interfaces

The CNT arrays are grown on $1 \times 1 \text{ cm}^2$ Si chips by water-assisted chemical vapor deposition approach at ambient pressure. The resulting CNT arrays are vertically aligned with an average length of $100 \text{ }\mu\text{m}$. The volume fraction of the CNT array is 1.84 % on averaged.

10-nm Cr, 150-nm Au, and 2- μm Cu are sequentially deposited on a 500- μm glass wafer. The Cr combined with Au serve as heat absorption and thermal reflection layers. A surface profiler (Alpha-Step IQ surface profiler) is used to quantify the cross-plane root-mean-squared (rms) roughness of the Cu top surface. The rms roughness of the sputtered Cu is $0.005 \text{ }\mu\text{m}$, subsequent rms roughness of Cu are measured at 0.024, 0.065, and $0.192 \text{ }\mu\text{m}$ scratched by 3- μm , 15- μm , and 30- μm grit sand paper, respectively. Figure 4.1 shows the sputtered Cu top surface with rms roughness $0.005 \text{ }\mu\text{m}$ (Figure 4.1(a)) and the scratched Cu top surface with rms roughness $0.024 \text{ }\mu\text{m}$ (Figure 4.1(b)).

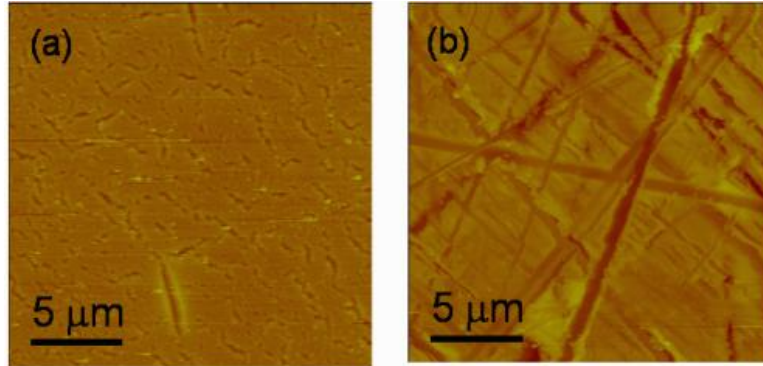


Figure 4.1. (a) Top view of the sputtered Cu surface. The rms roughness is 0.005 microns. (b) Top view of the Cu surface scratched by 3-micron grit. The rms roughness is 0.024 microns.

The CNT array top surface is sequentially coated with 10-nm Cr and 150-nm Au for adhesion. The SEM image of the Cr-Au coated CNT array top surface is shown in Figure 4.2. The out-of-plane rms roughness of the Cr-Au coated CNT array surface is measured to be 0.18 μm by the AFM topographic profile (Figure 4.3). The sample is prepared by bonding the Cr-Au coated CNT array to the Cu-coated side of the glass using a 2- μm In as bonding layer. The In bonding layer is initially deposited on the Cu-coated side of the glass, and the bonding process is performed at a nominal compressive stress of 392 kPa and temperature of 350°C.

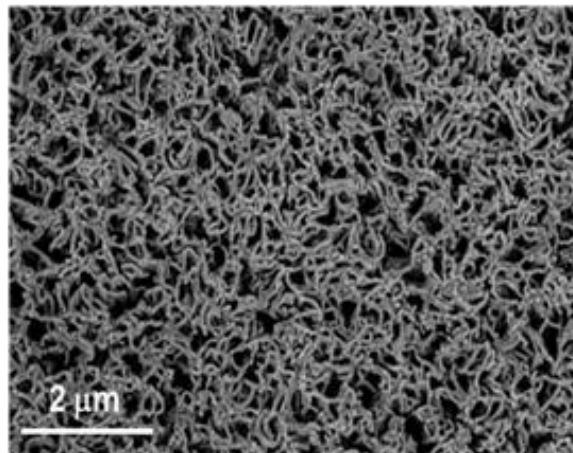


Figure 4.2. Top view SEM image of the CNT array sequentially coated with 10 nm-Cr and 150-nm Au.

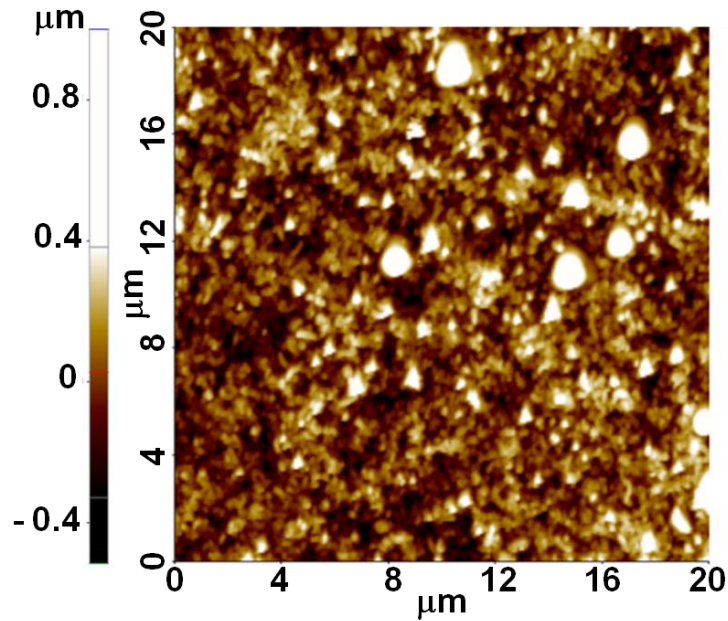


Figure 4.3. AFM topographic profile of the CNT array top surface sequentially coated with 10 nm-Cr and 150-nm Au.

The contact conductance between the Cu surface and the CNT array and the cross-plane thermal conductivity of the CNT array are measured using phase sensitive photo thermal reflectance thermometry. The principles of the thermometry and the experimental procedures are described in chapter 3.2. Figure 4.4 shows the sample structure and the pump and probe beam path. The pump and probe beam are focused at the Cr-Au-Cu coated side of the glass. A one dimensional transient heat conduction model is constructed based on the sample structure in Figure 4.4, where the glass substrate is considered as the first layer, the Cr-Au-copper is considered as the second layer, and In-Cr-Au-CNT array is considered as the third layer. Cr, Au, and, In are much thinner than the CNT array and thus are neglected in the heat conduction model. Table 4.1 lists the length, the thermal conductivity, and the volumetric heat capacity of glass, Cu, and the CNT array.

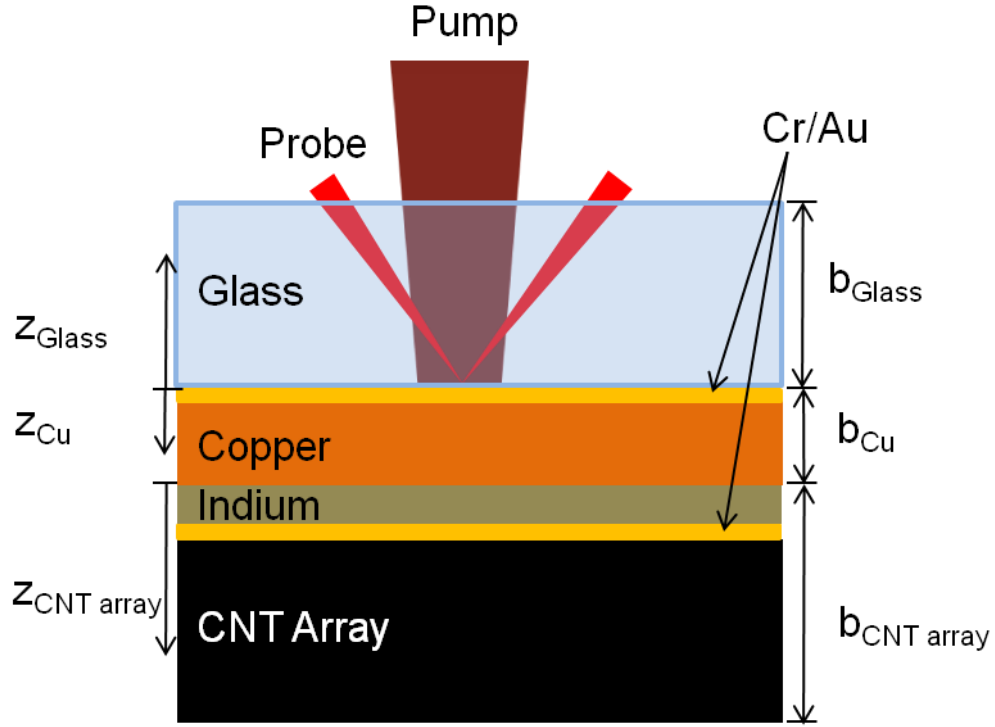


Figure 4.4. The sample structure and the pump and probe beam path.

Table 4.1. The length, the thermal conductivity, and volumetric heat capacity of glass, Cu, and the CNT array.

| | b (μm) | k (W/m-K) | C ($\text{kJ/m}^3\text{-K}$) |
|-----------|-----------------------|--------------|----------------------------------|
| Glass | 500 | 1.4 | 1625.0 |
| Cu | 2 | 401 | 3612.6 |
| CNT array | ~ 100 | undetermined | undetermined |

The governing equation for the glass-Cu-CNT array three-layer structure is

$$\frac{\partial T_j(z_j, t)}{\partial t} = \frac{k_j}{C_j} \frac{\partial^2 T_j(z_j, t)}{\partial z_j^2} \quad (4.1)$$

where the subscript j represents glass, Cu, and CNT array layers. The boundary conditions can be written as

$$-k_{\text{Glass}} \left. \frac{\partial T_{\text{Glass}}}{\partial z_{\text{Glass}}} \right|_{z_{\text{glass}}=0} = G_{\text{Glass-Cu}} (T_{\text{Cu}}(0) - T_{\text{Glass}}(0)) \quad (4.2)$$

$$q'' \exp(-i\omega t) = -k_{\text{Cu}} \left. \frac{\partial T_{\text{Cu}}}{\partial z_{\text{Cu}}} \right|_{z_{\text{Cu}}=0} + G_{\text{Glass-Cu}} (T_{\text{Cu}}(0) - T_{\text{Glass}}(0)) \quad (4.3)$$

$$-k_{Cu} \left. \frac{\partial T_{Cu}}{\partial z_{Cu}} \right|_{z_{Cu}=b_{Cu}} = G_{Cu-CNTarray} (T_{Cu}(b_{Cu}) - T_{CNTarray}(0)) = -k_{CNTarray} \left. \frac{\partial T_{CNTarray}}{\partial z_{CNTarray}} \right|_{z_{CNTarray}=0} \quad (4.4)$$

$$\left. \frac{\partial T_{Glass}}{\partial z_{Glass}} \right|_{z_{Glass}=b_{Glass}} = 0; \quad \left. \frac{\partial T_{CNTarray}}{\partial z_{CNTarray}} \right|_{z_{CNTarray}=b_{CNTarray}} = 0 \quad (4.5)$$

The temperature at $z_{Cu}=0$ can be analytically solved as a complex number and simply written as

$$T_{Cu}(0,t) = |T_{Cu}| \exp[-i(\omega t - \theta)] \quad (4.6)$$

where θ is the phase lag, and

$$\theta = f(\omega, k_j, C_j, b_j, G_{Glass-Cu}, G_{Cu-CNTarray}) \quad (4.7)$$

θ is plotted against ω to fit with the measured phase response.

$\phi_{CNTarray}$ is estimated to be 1.84% in equation (3.21); $b_{CNTarray}$, $G_{Cu-CNTarray}$, and $k_{CNTarray}$ are put into fitting parameters in the phase function. Figure 4.5 shows the measured phase responses with error bars (circles) and the corresponding best fit solutions (solid lines). $b_{CNTarray}$ are fitted to be 111 μm . The best fit solutions for the rest of the fitting parameters, $G_{Cu-CNTarray}$, and $k_{CNTarray}$, are listed in Table 4.2. The error bars of $G_{Cu-CNTarray}$ and $k_{CNTarray}$ are evaluated according to equation (3.22).

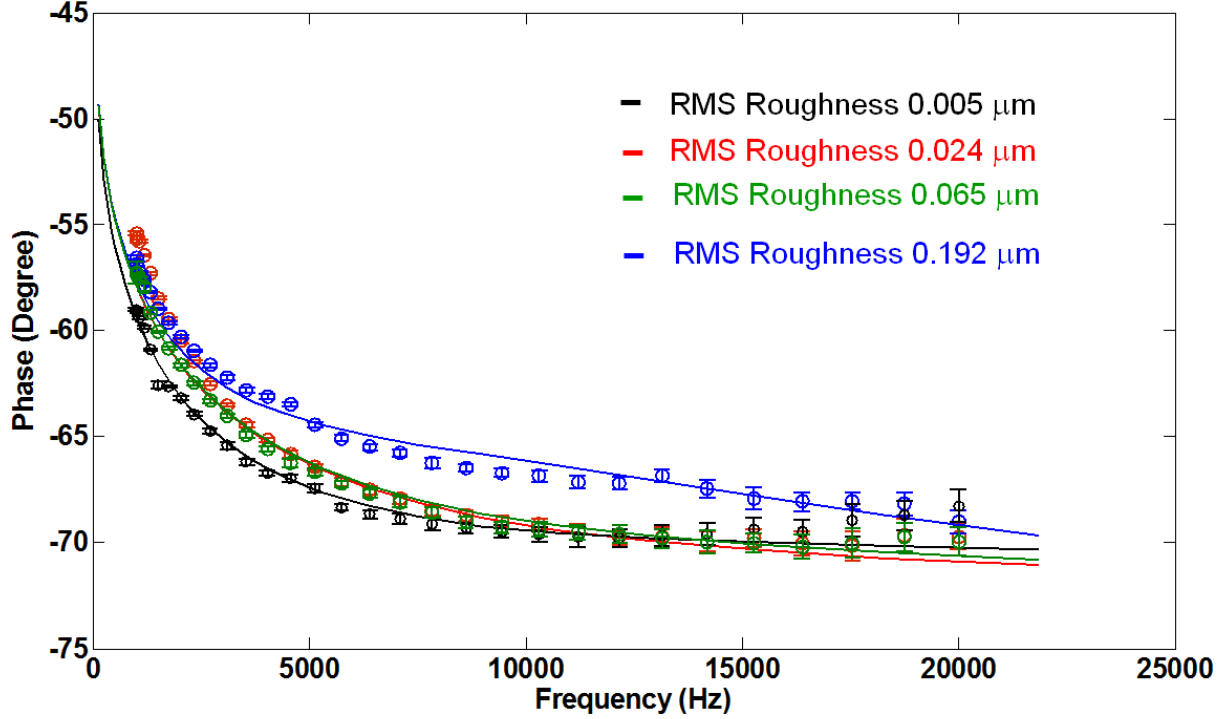


Figure 4.5. Measured phase responses and their standard deviations (circles) for various Cu surface roughness samples along with their best-fit solutions (solid lines).

Table 4.2. The best fit solutions of $G_{Cu-CNT\ array}$ and $k_{CNT\ array}$ corresponding to the Cu surface roughness.

| RMS Roughness (μm) | 0.005 | 0.024 | 0.065 | 0.192 |
|---|----------------|----------------|----------------|----------------|
| $G_{Cu-CNT\ array}$ ($\text{MW}/\text{m}^2\text{-K}$) | 2.00 ± 0.30 | 1.40 ± 0.60 | 1.20 ± 0.20 | 0.14 ± 0.02 |
| $k_{CNT\ array}$ ($\text{W}/\text{m-K}$) | 20 ± 1 | 18 ± 2 | 18 ± 2 | 18 ± 3 |

$G_{Cu-CNT\ array}$ and $k_{CNT\ array}$ are plotted against Cu surface roughness in Figure 4.6. $G_{Cu-CNT\ array}$ decreases by one order of magnitude as the Cu surface roughness increases from $0.065\ \mu\text{m}$ to $0.192\ \mu\text{m}$. The abrupt decrease of $G_{Cu-CNT\ array}$ at a Cu surface roughness $0.192\ \mu\text{m}$ could possibly be due to the drop in effective contact area between CNTs and Cu surface when the Cu surface roughness, $0.192\ \mu\text{m}$, starts to be comparable to the CNT array surface roughness, $\sim 0.18\ \mu\text{m}$. In other words, $G_{Cu-CNT\ array}$ is dependent on the Cu surface roughness only if the CNT array surface roughness is smaller than the Cu surface roughness. On the contrary, $k_{CNT\ array}$ has no significant variations as a function of Cu surface roughness. To explain this, it is possible that the number of thermally contacting carbon nanotubes in the CNT array to the Cu surface remains the same no matter the change of the Cu surface roughness. Such a decrease in $G_{Cu-CNT\ array}$ as a function of Cu surface roughness provides an insight on choosing the surface roughness of the target substrate especially for the case in which the CNT array surface roughness cannot be further decreases.

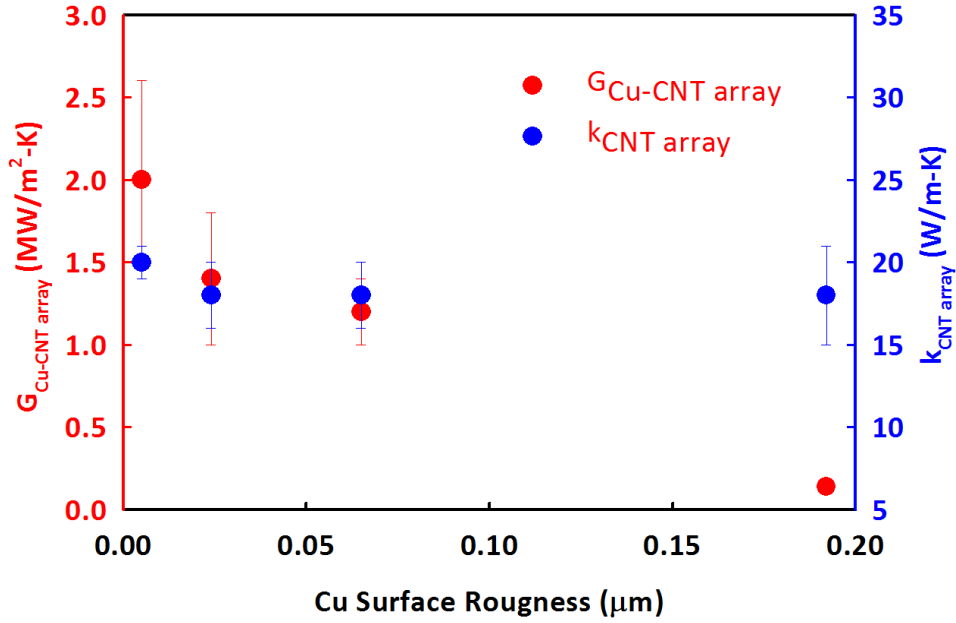


Figure 4.6. Cu-CNT array contact conductance and effective thermal conductivity of CNT array as a function of Cu surface roughness.

4.2 Density Dependent Thermal Transport Properties of Carbon Nanotube Array

In the previous section, the contact conductance between the CNT array and the target substrate decreases only when the surface roughness of the target substrate becomes larger than the surface roughness of the CNT array. In this section, the target substrate is chosen to be an atomically flat glass wafer while the mass density of the CNT array is varied. The thermal transport properties of the CNT arrays, including the contact conductance and the cross-plane thermal conductivity, are studied based on the variation of the CNT array mass density.

The mass density of the CNT array is controlled via the water-assisted CVD method described in chapter 2.2. The mass density and the corresponding volume fraction of the CNT array are listed in Table 2.1, where the volume fraction of the CNT array is 0.87%, 1.1%, 1.68%, 1.73%, or 1.84%. The CNT arrays are $\sim 100 \mu\text{m}$ in length. The CNT array top surface is coated with Cr-Au and bonded on the Cr-Au-In coated side of the glass at a nominal compressive stress of 196 kPa and temperature of 350°C. The details of the length of each layer are listed in Table 3.1.

A one dimensional transient heat conduction model is constructed based on the glass-In-CNT array, three-layer structure as shown in Figure 3.8. The heat conduction model for solving the phase function is described in equation (3.14)-(3.20). $\phi_{\text{CNT array}}$ is estimated at 0.87%, 1.1%, 1.68%, 1.73%, and 1.84% in equation (3.21). The fitting parameters in the phase function are $G_{\text{In-CNT array}}$, $k_{\text{CNT array}}$, $b_{\text{CNT array}}$, and b_{In} .

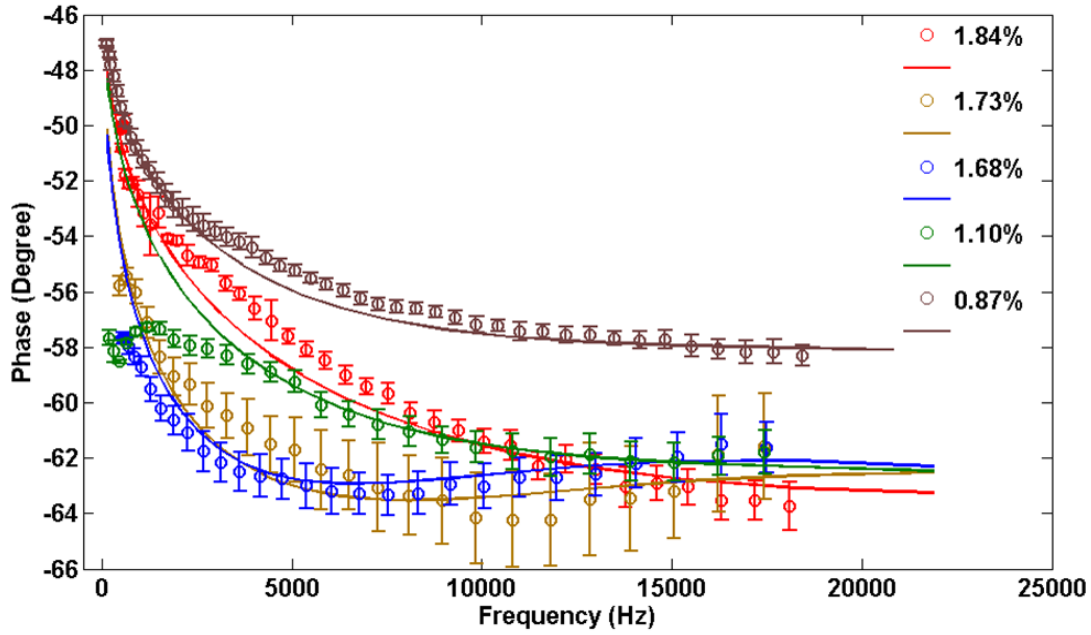


Figure 4.7. Phase responses with error bars (circles) with the corresponding best fit curve (solid lines) for each volume fraction (%) of CNT array.

Figure 4.7 shows the phase response with the corresponding best fit curve for each volume fraction of CNT array. The measured phase responses show no direct relation solely to volume fractions, which is due to the variations of CNT array length and the change in thickness of In film. The best fit solutions of the four fitting parameters corresponding to each volume fraction are listed in Table 4.3. The error of each parameter is calculated from equation (3.22).

Table 4.3. The best-fit-solution fitting parameters corresponding to the volume fraction of CNT arrays.

| Volume fraction (%) | $G_{In-CNTarray}$ (MW/m ² K) | $k_{CNTarray}$ (W/mK) | b_{In} (μm) | $b_{CNTarray}$ (μm) |
|---------------------|---|-----------------------|---------------|---------------------|
| 0.87 | 0.5±0.1 | 9±0.1 | 1 | 90 |
| 1.10 | 1.0±0.4 | 12±2 | 1.5 | 90 |
| 1.68 | 1.5±0.2 | 20±2 | 2.1 | 130 |
| 1.73 | 1.8±0.3 | 22±3 | 2 | 120 |
| 1.84 | 3.0±0.5 | 30±2 | 1 | 70 |

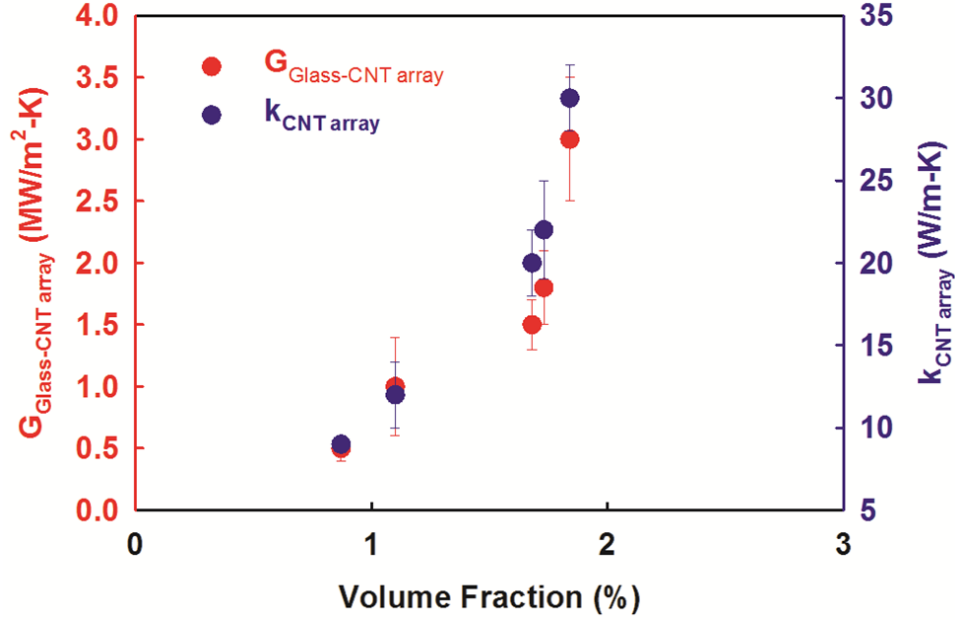


Figure 4.8. $G_{Glass-CNT\ array}$ and $k_{CNT\ array}$ versus volume fraction (%) of CNT arrays. Both $G_{Glass-CNT\ array}$ and $k_{CNT\ array}$ increase monotonically as the volume fraction increases.

In Figure 4.8, $G_{Glass-CNT\ array}$ and $k_{CNT\ array}$ are plotted against the CNT array volume fraction, where

$$G_{Glass-CNTarray} = ((G_{Glass-In})^{-1} + (G_{In-CNTarray})^{-1})^{-1}. \quad (4.8)$$

Since $G_{Glass-In}$ is much larger than $G_{In-CNTarray}$, $G_{Glass-CNTarray}$ is approximately $G_{In-CNTarray}$. Figure 4.8 shows that both $G_{Glass-CNTarray}$ and $k_{CNTarray}$ increase monotonically as the volume fraction of CNT array increases. The increasing trend of $G_{Glass-CNTarray}$ is possibly due to the increase of number of CNTs contacting the glass which could potentially increase the CNT array-glass contact area. The area fraction of the CNT array contacting to the In film can be estimated as

$$\phi_{area} \approx \frac{G_{In-CNTarray}}{G_{In-Graphite}} \quad (4.9)$$

where $G_{In-Graphite}$ is the contact conductance between indium and graphite which is estimated to be 10^8 W/m²-K according to the measured metal-dielectric contact conductance.⁷³ Divided by $G_{In-Graphite}$, the $G_{In-CNTarray}$ listed in Table 4.3 sequentially yields ϕ_{area} at 0.5%, 1%, 1.5%, 1.8%, and 3%. Except for the lowest volume fraction (0.87%) CNT array and the highest volume fraction (1.87%) CNT array, the estimated ϕ_{area} is close to $\phi_{CNTarray}$. When the area fraction is lower than the as-grown volume fraction of the CNT array, it could possibly due to the uneven length of the tubes which causes less than total number of tubes contacting to the In film. On the contrary, when the area fraction is higher than the as-grown volume fraction of the CNT array, it

could possibly be due to the higher degree of entanglement at the CNT array top surface which enhances the contact length of the tube.

Quantitatively, it has been determined that the increasing rate of $k_{CNT\ array}$ is larger than the increasing rate of the CNT array volume fraction. If each tube in the CNT array is vertically aligned, the cross-plane thermal conductivity of the CNT array is

$$k_{CNTarray} = \phi_{CNTarray} k_{CNT} \quad (4.10)$$

where k_{CNT} is the thermal conductivity of the individual CNT. Divided by volume fractions of the as-grown vertically aligned CNT arrays at 0.87%, 1.1%, 1.68%, 1.72%, and 1.84%, the thermal conductivity of CNT array, $k_{CNT\ array}$, yield the thermal conductivity of individual CNT, k_{CNT} , with values at 1035 ± 12 , 1091 ± 182 , 1191 ± 119 , 1272 ± 173 , and 1630 ± 109 W/m-K. The decreasing trend of k_{CNT} as the volume fraction decrease indicates either an intrinsic decrease in the thermal conductivity of the individual CNT or a breaking down of equation (4.10) or some oversimplified assumption. Both cases could be due to the higher degree of deformation for CNT array with lower volume fraction resulting from the bonding process. The degree of deformation has been verified experimentally. The highest volume fraction array, 1.84% (Figure 4.9 (a)), and the lowest volume fraction array, 0.87% (Figure 4.9 (b)), are both subjected to a nominal compression stress, 196 kPa, applied on the top surface. Before compression, the two arrays are at the same height, averaging 130 μm in length. After compression, it was determined that the array with volume fraction of 0.87% decreased more than a factor of 3 in length (Figure 4.9 (c)) compared to the array with volume fraction of 1.84% (Figure 4.9 (d)). Moreover, there are layered structures caused by buckling of the CNT array in Figure 4.9 (d), where the number of layers in the image is approximately 3 layers.

However, it has been experimentally shown that the intrinsic thermal conductivity of individual CNT has only small variations (within 10%) by buckling the individual tube unless the tube is broken.⁷⁵ The chance of the intrinsically decrease in the thermal conductivity of individual tube is low and thus can be negligible. Since certain CNT arrays are no longer vertically aligned after compression (as shown in Figure 4.9 (d)), the cross-plane thermal conductivity of the CNT array could no longer equal to the volume fraction times the thermal conductivity of the individual CNT; that is, equation (4.10) is invalid when the CNT array is buckling.

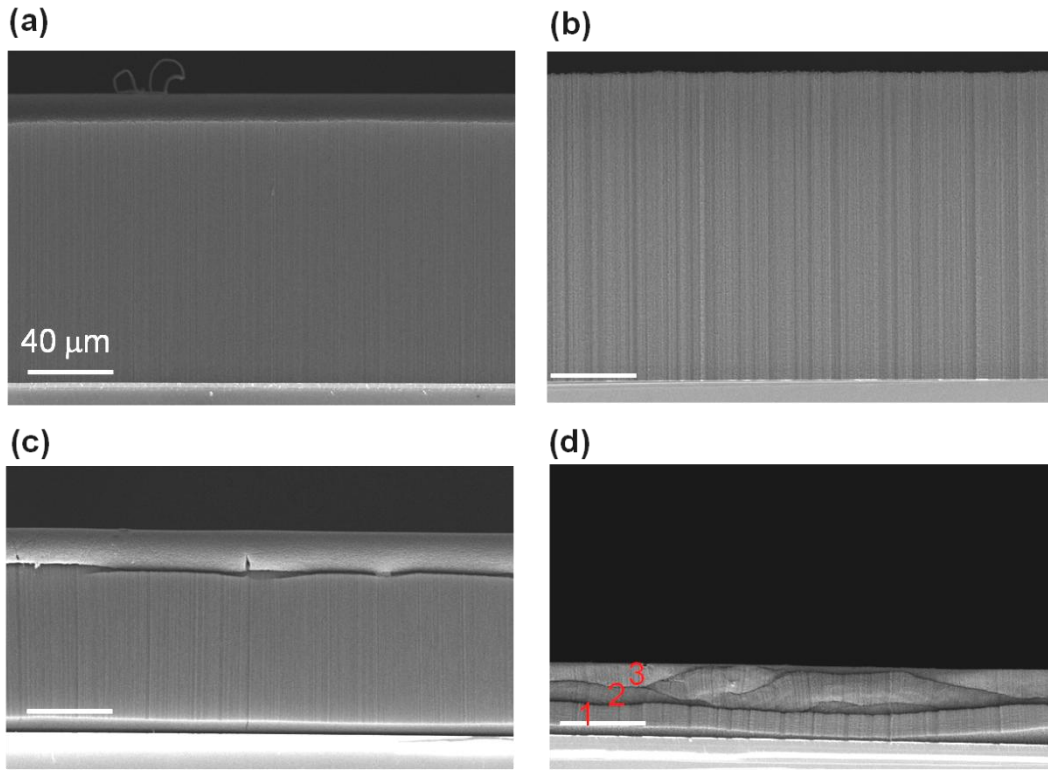


Figure 4.9. Side views SEM images of the CNT array with (a) 1.84% and (b) 0.87% in volume fraction before compression. Both the CNT arrays are ~ 130 microns in length. After compression, the CNT array with initially (c) 1.84% in volume fraction decreases 30 microns in length while the CNT array with initially (d) 0.87% in volume fraction decreases 100 microns in length. The scale bar in image (a)-(d) is 40 microns.

The heat conduction in the buckled CNT array is analyzed to explain the correlation between the cross-plane thermal conductivity of the CNT array and the intrinsic thermal conductivity of the individual tube. It is considered that the CNT array consists of N tubes contacting to the target substrate and that the CNT array is initially vertically aligned (as shown in Figure 4.10 (a)). When the CNT array is buckled, the CNT array consists of n layers which divide the CNT array into $2n-1$ packets along cross-plane direction (as shown in Figure 4.10 (b)). The yellow box points out a single packet between two tubes, where one of the tube is at the edge of the CNT array. A closer view for the single packet at the edge of the CNT array is shown in Figure 4.10 (c). There are three kinds of resistance in the packet namely: the thermal resistance between one folded tube, R_{Van_e} ; the thermal resistance of the individual tube, R_{CNT} ; and the thermal resistance between two folded tubes, R_{Van_i} .

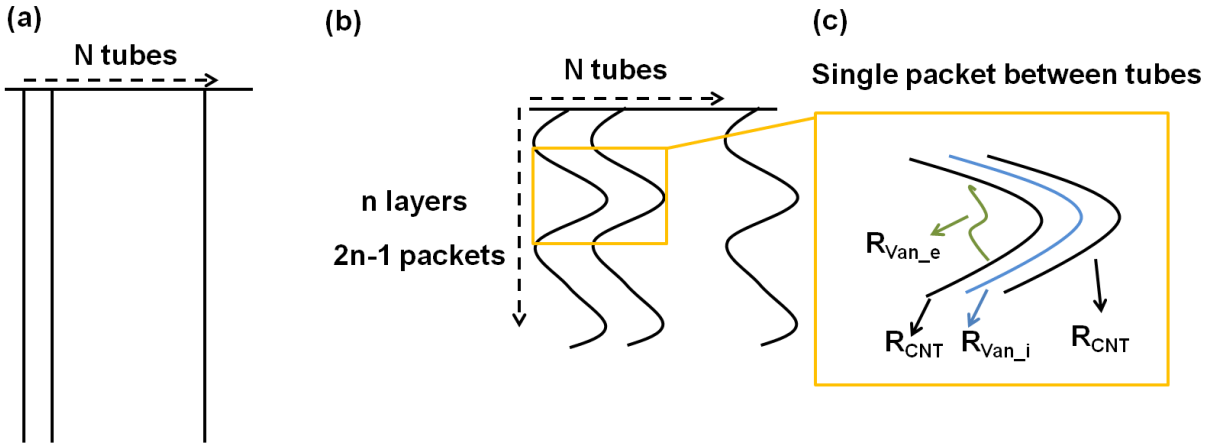


Figure 4.10. Schematic cross view of (a) the vertically aligned CNT array and (b) the CNT array with layered structure. Both the CNT arrays in (a) and (b) include N number of tubes. While the CNT array with (b) layered structure has n number of layers and $2n-1$ number of packets. Schematic (c) shows the single packet between two tubes.

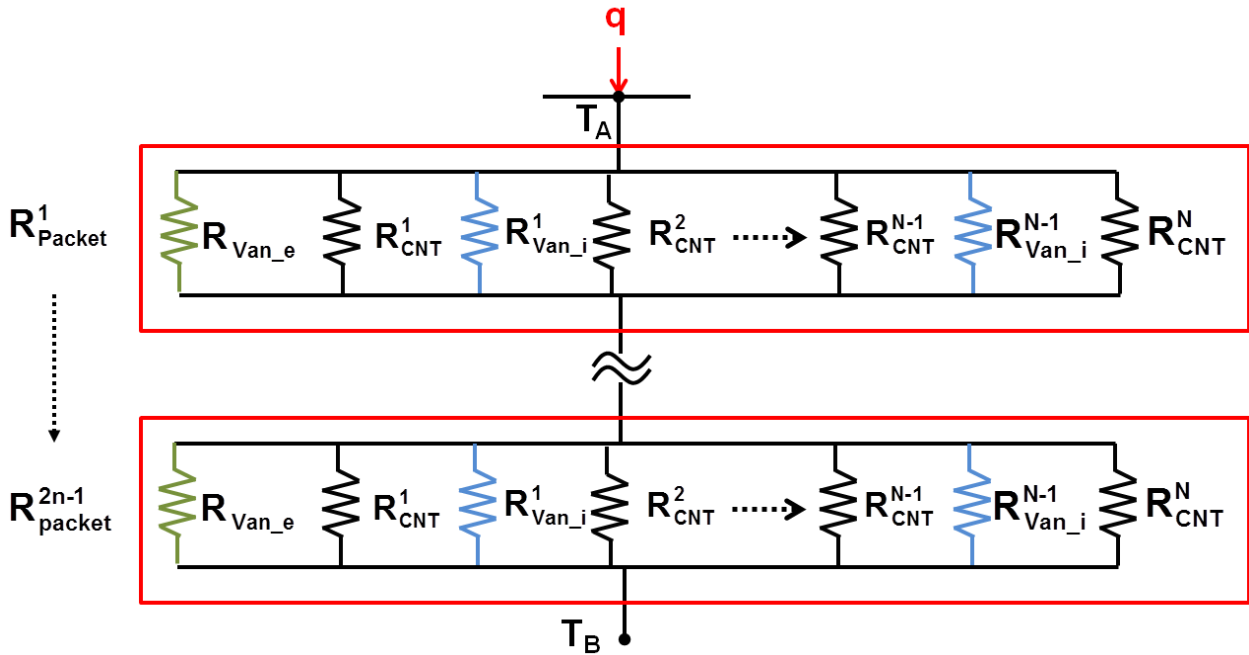


Figure 4.11. Thermal resistance network modeling the heat conduction in the CNT array with layered structure.

The modeling of the heat conduction in the buckled CNT array is built based on the thermal resistance network composed of R_{Van_e} , R_{CNT} ; and R_{Van_i} (as shown in Figure 4.11). Fourier's law is applied to the heat conduction model assuming that the heat conduction is one dimensional with heat, q (with unit [W]) and is injected on top of the CNT array. In addition, it is assumed that the temperature is uniformly distributed in the in-plane direction with the temperature at the top of the CNT array is T_A and the temperature at the bottom of the CNT array is T_B . If the CNT array is considered as a film, the total heat, q , is equal to

$$q = \frac{k_{CNTarray} A_{film} (T_A - T_B)}{L_{film}} \quad (4.11)$$

where A_{film} is the apparent area at top of the CNT array and L_{film} is the apparent length of the CNT array.

If the CNT array is considered to be composed by N tubes and $2n-1$ packets, the thermal resistance of the tube, between the tubes, and between the packets should be considered. R_{Van_e} , R_{CNT} , and R_{Van_i} , are parallel in each packet, where the number of R_{Van_e} , R_{CNT} , and R_{Van_i} are 1, N , and $N-1$, respectively, in each packet. The thermal resistance of each packet is then

$$R_{packet} = (NR_{CNT}^{-1} + (N-1)R_{Van_i}^{-1} + R_{Van_e}^{-1})^{-1}. \quad (4.12)$$

If there are $2n-1$ packets in the CNT array and the thermal resistance of the packets are in series, the total heat, q , is equal to

$$q = \frac{(T_A - T_B)}{(2n-1)R_{packet}} = \frac{(T_A - T_B)}{(2n-1)(NR_{CNT}^{-1} + (N-1)R_{Van_i}^{-1} + R_{Van_e}^{-1})^{-1}}. \quad (4.13)$$

Equation (4.11) and equation (4.13) can be combined into

$$\frac{(T_A - T_B)}{(2n-1)(NR_{CNT}^{-1} + (N-1)R_{Van_i}^{-1} + R_{Van_e}^{-1})^{-1}} = \frac{k_{CNTarray} A_{film} (T_A - T_B)}{L_{film}} \quad (4.14)$$

where each thermal resistance in the left side of the equation is the inverse of the thermal conductance

$$R_j^{-1} = U_j \quad (4.15)$$

U stands for the thermal conductance in each packet; it is an intensive property with unit [W/K]. The subscript j stands for CNT , Van_i , or Van_e . Combining equations (4.15) and (4.14) yields

$$k_{CNTarray} = \frac{L_{film} (NU_{CNT} + (N-1)U_{Van_i} + U_{Van_e})}{(2n-1)A_{film}}. \quad (4.16)$$

A_{film} equals to the total number of tubes in the CNT array times the averaged cross area of the individual tube at top of the CNT array, divided by the area fraction of the CNT array at the top surface

$$A_{film} = \frac{NA_{CNT}}{\phi_{area}}. \quad (4.17)$$

Assuming that the averaged cross section of the individual tube at the top of the CNT array is the cross sectional area of the tube

$$A_{CNT} = \frac{\pi}{4} d_{CNT}^2 \quad (4.18)$$

where d_{CNT} is the averaged diameter of the individual tube. The thermal conductivity of the CNT array can now be expressed as

$$k_{CNTarray} = \frac{L_{film} (NU_{CNT} + (N-1)U_{Van_i} + U_{Van_e}) \phi_{area}}{(2n-1)NA_{CNT}} \quad (4.19)$$

where the number of tubes in the CNT array contacting the target substrate, N , is approximately 10^{10} estimated from the number of catalyst particles in chapter 2. Since $N \gg 1$, the last term in the numerator of equation (4.19) is negligible

$$\frac{L_{film} U_{Van_e} \phi_{CNTarray}}{(2n-1)NA_{CNT}} \approx 0 \quad (4.20)$$

and

$$N-1 \approx N \quad (4.21)$$

The thermal conductivity of the CNT array can now be simplified to

$$k_{CNTarray} \approx \frac{L_{film} U_{CNT} \phi_{area}}{(2n-1)A_{CNT}} + \frac{L_{film} U_{Van_i} \phi_{area}}{(2n-1)A_{CNT}} \quad (4.22)$$

This indicates that the thermal conduction in the buckled CNT array is contributed by the thermal conductance of the tubes in the packet, U_{CNT} , and the thermal conductance between the tubes in the packet, U_{Van_i} . U_{CNT} equals to the intrinsic thermal conductivity of the individual CNT per actual length of the tube in each packet times the cross section area of the tube

$$U_{CNT} = \frac{k_{CNT}}{L_{CNT} (2n-1)^{-1}} A_{CNT} \quad (4.23)$$

L_{CNT} is the actual length of the tube, which is equal to the original length of the CNT array if each tube in the CNT array has the same length. U_{Van_i} equals to tube-tube thermal contact conductance times the contact length between tubes in each packet times the circumference of the tube

$$U_{Van_i} = G_{Van_i} \frac{L_{CNT}}{(2n-1)} \pi d_{CNT} \quad (4.24)$$

where G_{Van_i} is the tube-tube thermal contact conductance, which is an extensive property with unit of W/m^2K . Combining equations (4.23), (4.24), and (4.22), the final expression for the thermal conductivity of a buckled CNT array is

$$k_{CNTarray} \approx \frac{L_{film} k_{CNT} \phi_{area}}{L_{CNT}} + \frac{4L_{film} G_{Van_i} L_{CNT} \phi_{area}}{(2n-1)^2 d_{CNT}}. \quad (4.25)$$

One can verify equation (4.25) using the measured cross-plane thermal conductivity of the CNT array with buckled structure. The cross-plane thermal conductivity of the CNT array with initially 0.87% in volume fraction is measured to be 9 W/m-K (listed in Table 4.3) after buckling of the CNT array (as shown in Figure 4.9 (d)).

The cross-plane thermal conductivity of the buckled CNT array contributed by the thermal conductance of CNT is ~ 1.9 W/m-K according to equation (4.25), where k_{CNT} is approximately 1630 W/m-K, L_{Film} is ~ 30 μm measured in the SEM image (Figure 4.9 (d)), ϕ_{area} is $\sim 0.5\%$, and L_{CNT} is ~ 130 μm . In the above estimation, k_{CNT} is estimated from the cross-plane thermal conductivity of the CNT array with initially 1.84% in volume fraction using equation (4.10) since the CNT array with 1.84% in volume fraction keeps the alignment structure during thermal conductivity measurement. The cross-plane thermal conductivity of the buckled CNT array contributed by the thermal conductance of CNT is less than the measured CNT array thermal conductivity, 9 W/m-K. This indicates that the tube-tube contact conductance, G_{Van_i} , also plays an important role in contributing the thermal conductivity of the buckled CNT array. One can calculate $k_{CNTarray}$ contributed by G_{Van_i} from the second term in equation (4.25). If $k_{CNTarray}$ is 7 W/m-K with the number of layers in the buckling structure, $n=3$ (according to the SEM image in Figure 4.9 (d)), then G_{Van_i} is $\sim 1 \times 10^4$ W/m²-K. The value of G_{Van_i} is in reasonable order agreement with reported data obtained by molecular dynamics simulation.⁷⁶

4.3 Buckling Behavior of Carbon Nanotube Array

Previous sections have shown that the thermal transport properties of a CNT array are dependent on the density of the array. Both the glass-CNT array contact conductance and the thermal conductivity of a CNT array increase monotonically as a function of CNT array volume fraction. Quantitatively, it has been determined that the increasing rate of the cross-plane thermal conductivity is larger than the increasing rate of the CNT array volume fraction. Such increasing rate is due to the uneven deformation of the CNT arrays resulting from the bonding stress. It has been verified under SEM analysis that the lowest volume fraction CNT array is mechanically buckled while the highest volume fraction CNT array is vertically aligned under same nominal compressive stress. A heat conduction model based on the thermal resistance network shows that the buckling structure of CNT array further decreases the cross-plane thermal conductivity of CNT array. In the work of this section, the buckling behavior of CNT array is measured systematically as a function of nominal compressive stress which provides comprehensive information for analyzing the thermal transport properties of CNT array.

The stress-strain diagram of CNT array under compression is first tested in order to find out the buckling strength of CNT array. A group of CNT arrays is grown on 5×5 mm² Si substrates, where the CNT arrays are grown 290 ± 30 μm in length and 0.4%, 0.6%, 0.8% in

volume fraction. Figure 4.12 shows the system for measuring the loading and the displacement of CNT array. The measurement system consists a load cell, (with output voltage $0.4 \mu\text{V/g}$ and sensitivity down to 2.5 g) to measure the applied compressive force on CNT array, and a translational stage with controlled step size $1 \mu\text{m}$ to measure the displacement of CNT array. The calibration of output voltage as a function loading is in Appendix B. An iron flat plate, which has $10 \times 5 \text{ cm}^2$ in in-plane area, is attached on the translational stage and uniformly compresses the CNT array. The CNT array is considered as a film which has an apparent in-plane area: $5 \times 5 \text{ mm}^2$. Note that the elastic modulus of the iron plate, the Si substrate, and the load cell are much larger than the reported elastic modulus of CNT array⁷ so that the displacement measured from the translational stage is approximately the displacement of CNT array. The nominal applied compressive stress on the CNT array is calculated as the applied force over the apparent in-plane area of the CNT array, and the strain is calculated as the displacement of the CNT array over original length of the CNT array.

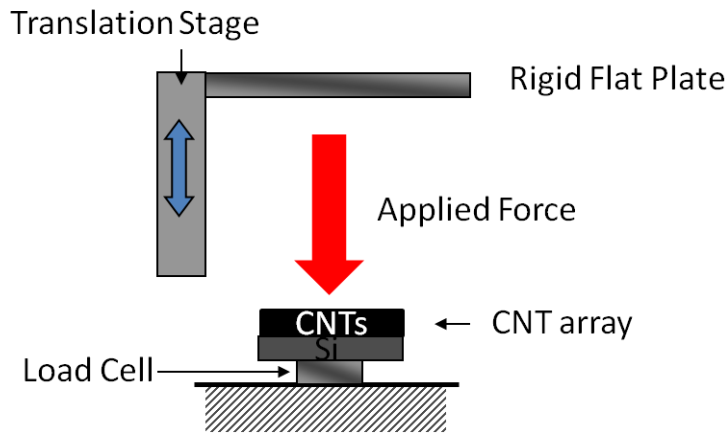


Figure 4.12. Measurement system for compressive test.

The stress-strain diagram of CNT arrays with initially 0.6% in volume fraction is shown in Figure 4.13. At least three samples with the same condition are verified to have the repeating stress-strain diagram. The stress is measured after 10 seconds at each displacement to wait until the stress is stabilized. The stress-strain diagram is a nonlinear curve which can be divided into three regions by two turning points, where the 1st turning point occurs approximately at 0.2 in strain and 50 kPa, and the 2nd turning point occurs approximately at 0.7 in strain and 70 kPa (see Figure 4.14). The ex-situ SEM images were taken in different region of the diagram to monitor the response of the CNT array. The SEM images at a given stress of the CNT array in Figure 4.14 are shown in Figure 4.15 (a)-(d). At 42 kPa, the CNT array is vertically aligned, while from 58 kPa-189 kPa, the CNT array is buckled. This indicates that the start of the plateau region (second region) in the stress-strain diagram is the start of the buckling of CNT array due to the instability of the structure,³ where the nominal buckling strength of the CNT array can be estimated from the 1st turning point in the stress-strain diagram to be 50 kPa.

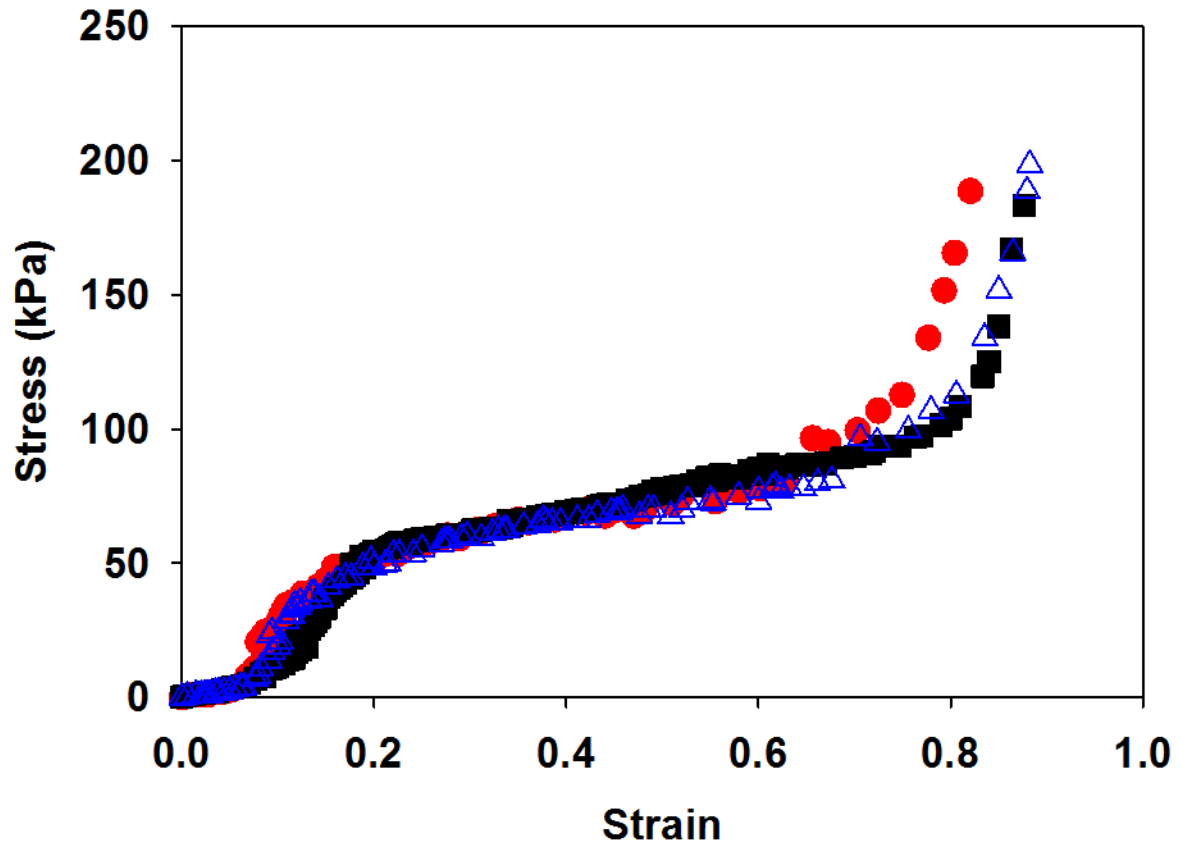


Figure 4.13. Stress-strain diagram of 0.6% volume fraction CNT arrays.

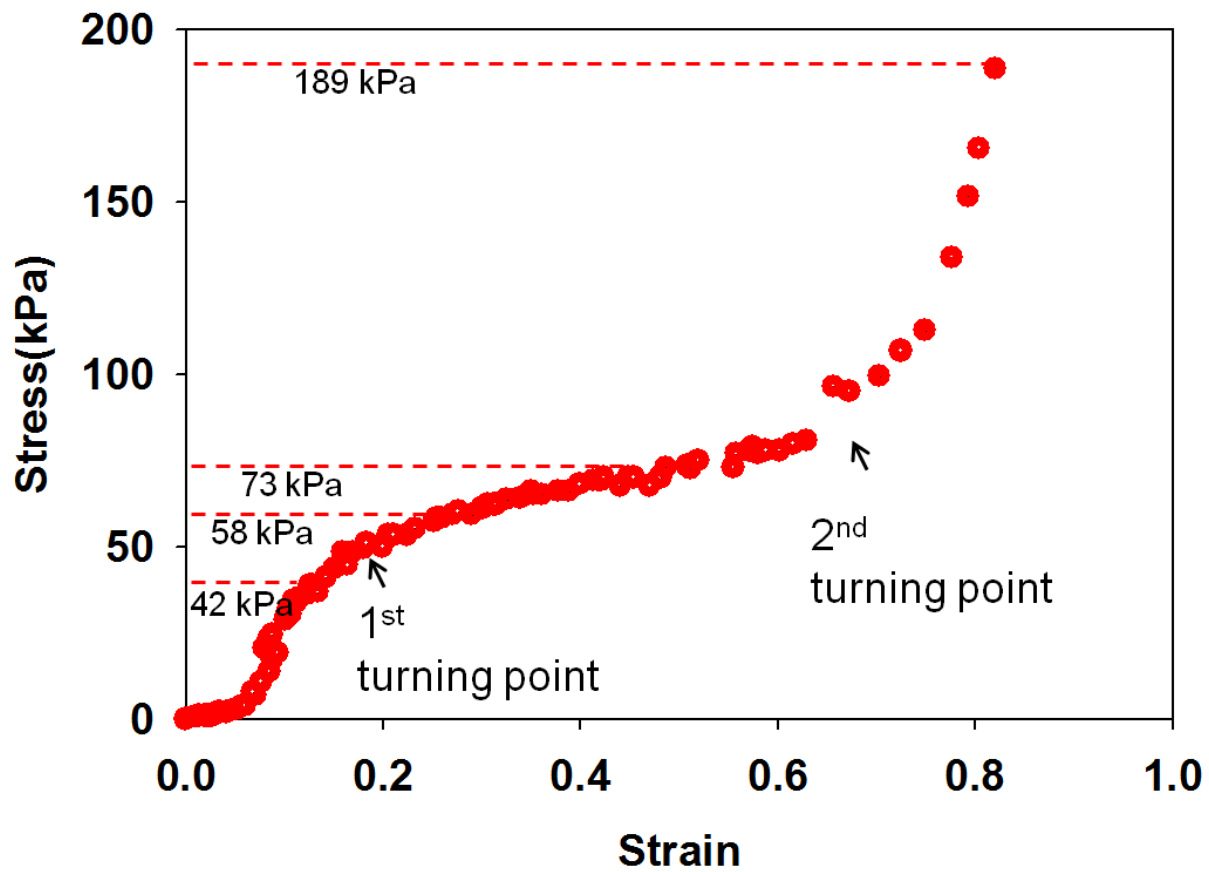


Figure 4.14. Turning points in the stress-strain diagram of 0.6% volume fraction CNT array.

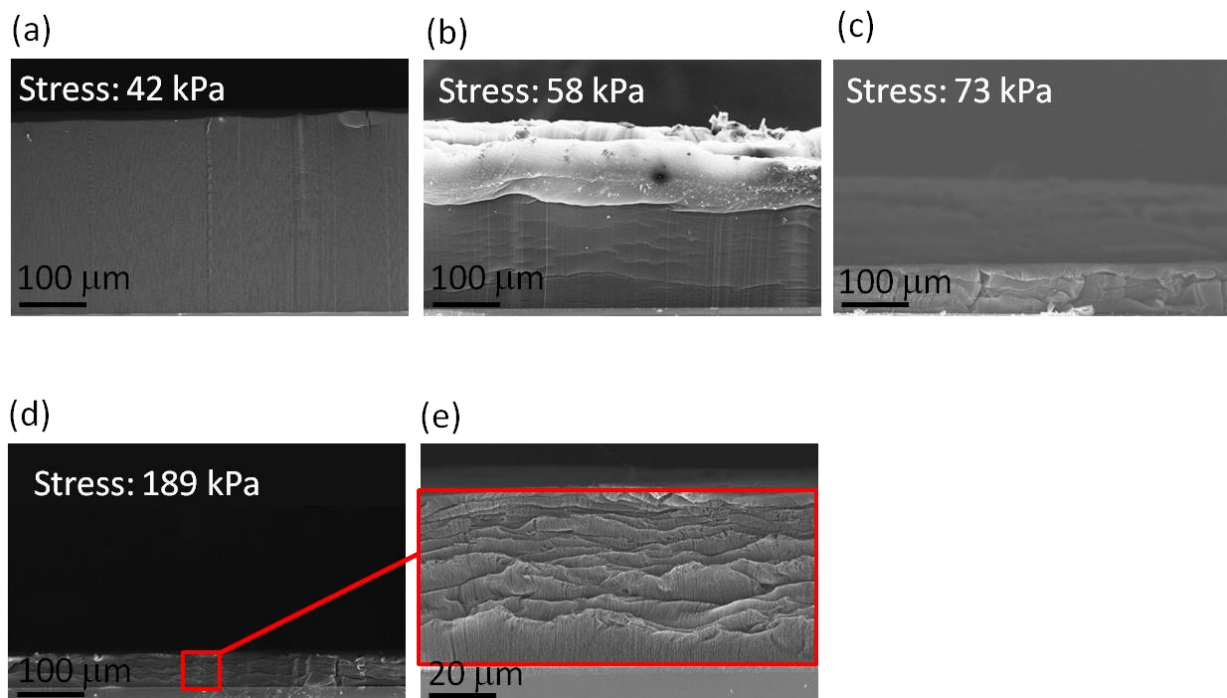


Figure 4.15. SEM images of the 0.6% volume fraction CNT array after compression, where the compressions were stopped at (a) 42 kPa, (b) 58 kPa, (c) 73 kPa, and (d) 189 kPa. Image (e) shows the higher resolution of image (d).

As shown in the SEM images (Figure 4.15 (b) and Figure 4.15(c)), the CNT array has more significant decrease in length in the second region of the stress-strain diagram. Until the third region, the CNT array becomes more compact which rapidly increases the stress as the strain increases in Figure 4.14. There are approximately 10 layers in the buckling structure of the CNT array at nominal stress 189 kPa (see Figure 4.15 (e)). It is possible that the layers in the buckling structure have already formed at the initial stage of the buckling structure (as shown in the light ripples in the CNT array in Figure 4.15 (b)), and that the number of layer does not change from the initial stage till the final stage of the buckling structure. What changes the buckling structure is the distance between the layers.

The above stress-strain diagram was measured under steady state; however, it was found that the nominal stress relaxes within 10 seconds at each displacement. The relaxation of nominal stress was measured within 10 seconds to find the instability of the buckling structure. As show in Figure 4.16, when the initial stress of the CNT array is 35 kPa, which is in the first region of the stress-strain diagram shown in Figure 4.14, the stress fluctuates within 2% of the initial stress along the time axis. When the CNT array is at stress 50 kPa, which is right at the first turning point in the stress-strain diagram, the stress drops significantly for 8% within 1 second. As the initial stress increases from 50 kPa to 74 kPa, which is in the second region of the stress-strain diagram, the stress relaxation curve keeps changing and the drop rate of the stress also decreases. Once the strain reaches the third region of the stress-strain diagram, 74 kPa and 112 kPa, the stress relation is unchanged, although the fluctuations decrease significantly. At 189 kPa, where the CNT array is fully packed, the drop rate of the stress decreases again and the fluctuations also drop significantly. With the stress-strain diagram in Figure 4.14 and the SEM images in Figure 4.15, one can tell that the highest degree of instability of the CNT array occurs

whenever the buckling structure starts and that the degree of instability of the buckling structure decreases as the CNT array becomes more compact.

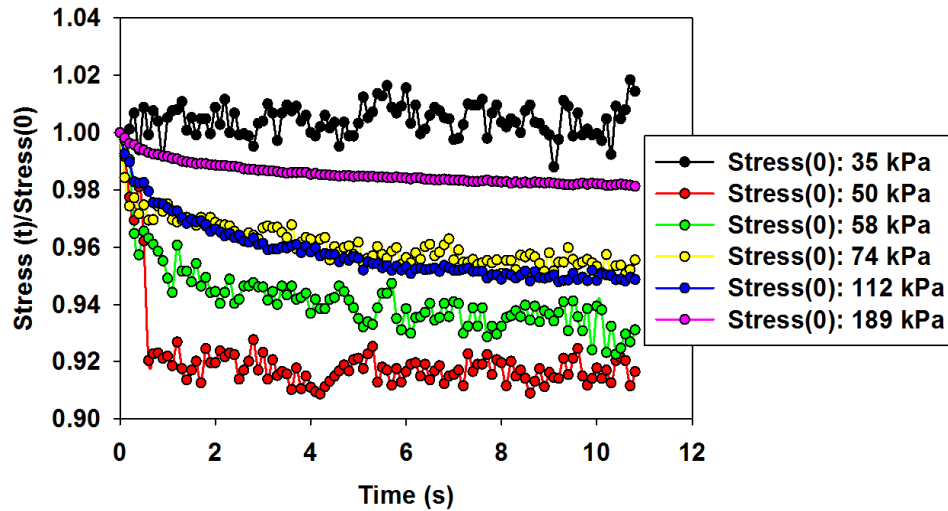


Figure 4.16. Stress relaxation curve of the 0.6% volume fraction CNT array corresponding to the initial stress.

Cyclic compression was applied to the CNT array with 0.6% in volume fraction. As shown in the steady-state stress-strain diagram in Figure 4.17, the CNT array is permanently deformed starting from the first region (see Figure 4.17). The diagram shows that the CNT array assembly deforms plastically. There is energy loss during the cyclic compression, and the loss of energy could be possibly stored in the van der Waals bonding among CNTs.

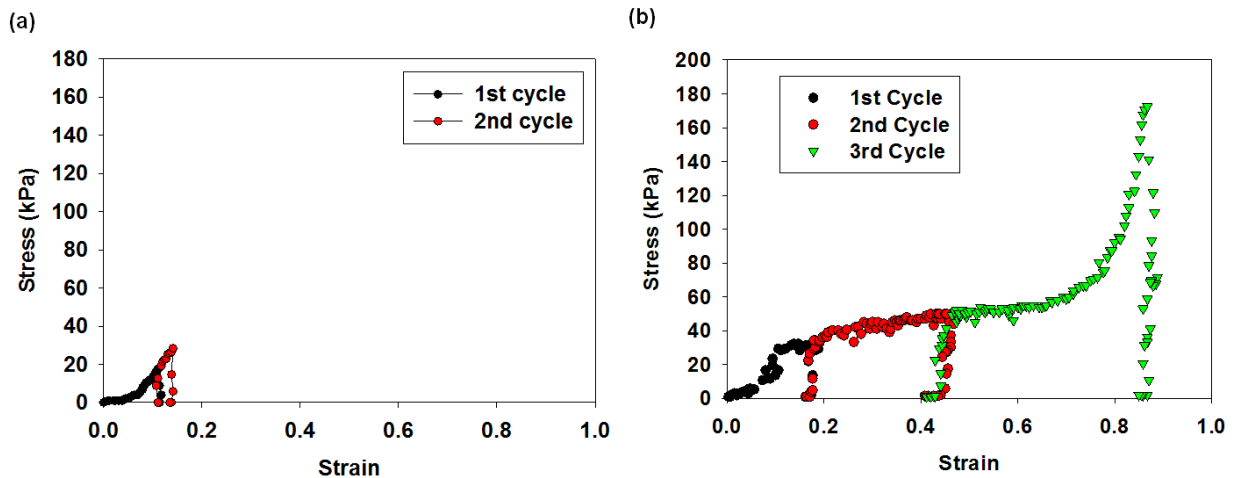


Figure 4.17. The stress-strain diagram of the 0.6% volume fraction CNT array under cyclic compression. Figure (a) shows the cyclic compression is within first region (1st and 2nd cycle) and (b) shows the cyclic compression is at the turning point (1st cycle), within the second region (2nd cycle), and at the end of the third region (3rd cycle).

Finally, the steady-state stress-strain diagram corresponding to the CNT array with different volume fractions is measured. As shown in Figure 4.18, the nominal buckling strength increases from 25 kPa, 50 kPa, to 100 kPa as the array volume fraction increases from 0.4%, 0.6%, to 0.8%. By assuming that the initial volume fraction of the CNT array is the area fraction of the CNT array, one can calculate the actual buckling strength of the CNT array by dividing the

nominal strength over the initial volume fraction of the CNT array. The actual buckling strengths are calculated to be 6.25 MPa, 8.33 MPa, and 12.5 MPa at 0.4%, 0.6%, and 0.8% in volume fraction. If there is no tube to tube interaction, the actual buckling strength of the CNT array should be the same regardless of the change in CNT array packing density. However, the result shows that the actual buckling strength increases as the CNT array density increases which could possibly be due to the stronger van der Waals bonding between tubes in higher density CNT array.

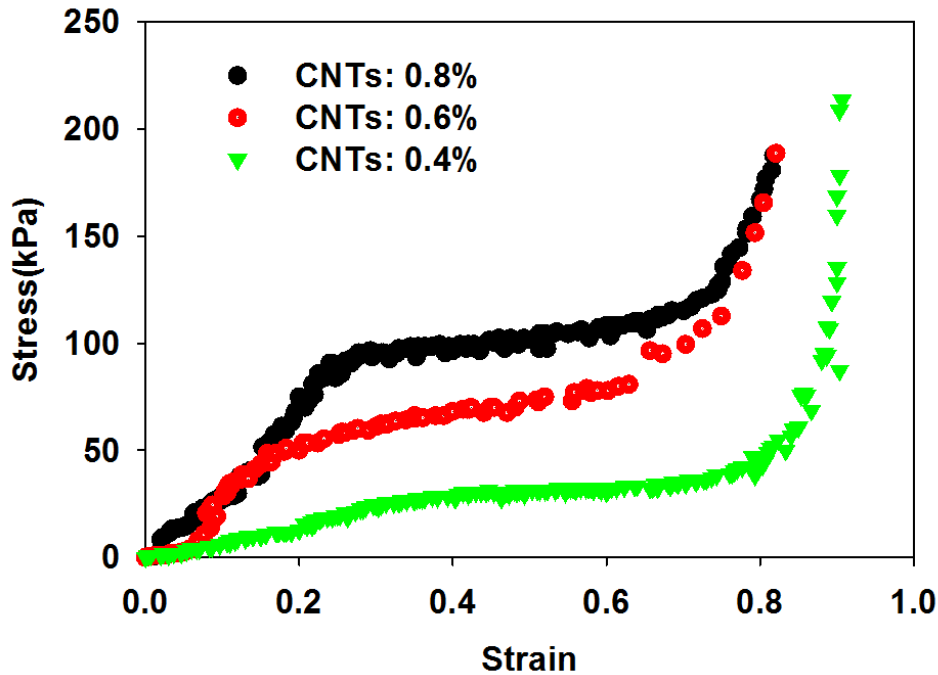


Figure 4.18. The stress strain diagram corresponds to the CNT array with 0.4%, 0.6%, and 0.8% in volume fraction.

4.4 Effect of Buckling on Thermal Transport Properties of Carbon Nanotube Array

It has been shown in previous sections that the thermal conductivity of a CNT array decreases as a result of the buckling structure. The correlation between the thermal conductivity of CNT array and the buckling structure is built based on the heat conduction through thermal resistance network. In this section, the thermal conductivity of CNT array is systematically measured as a function of applied compressive stress and analyzed by the resulting structure of the CNT array. The number of buckling layers in the CNT array can be referred from the SEM image. And the distance between layers can be referred from the strain of the CNT array according to the stress-strain diagram.

A batch of CNT arrays were grown with of volume fraction of $\sim 0.6\%$ and $\sim 165 \mu\text{m}$ in length. The strain-stress diagram of the $165\text{-}\mu\text{m}$ CNT array is testified to approximately conform to the stress-strain diagram of the $290\text{-}\mu\text{m}$ CNT array with the same volume fraction (see Figure

4.19). This indicates that the number of buckling layers may be close to the number of layers shown in Figure 4.15(e).

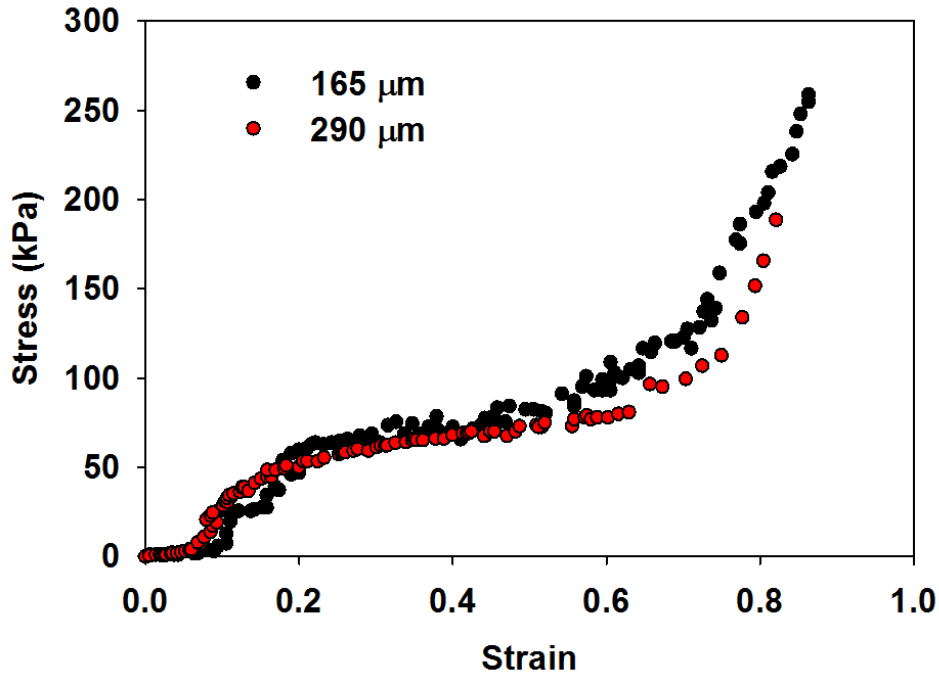


Figure 4.19. The stress-strain diagram of the 165-micron CNT array and the 290-micron CNT array. Both the CNT arrays are initially 0.6% in volume fraction.

The CNT arrays are bonded on glass substrate with nominal compressive stresses of 28 kPa, 46 kPa, 72 kPa, 105 kPa, 172 kPa, 245 kPa, 452 kPa, and 560 kPa. Since the CNT array is permanently deformed according to the cyclic compression test shown in Figure 4.17, the corresponding strain of the CNT array is estimated to be 0.16, 0.19, 0.37, 0.64, 0.77, 0.85, 0.86, and 0.86, respectively, from the stress-strain diagram in Figure 4.19. The length of the In layer for thermal compression bonding is reduced to ~ 100 nm in order to decrease the bulk resistance. Other details of sample preparation for thermal properties measurement are described in chapter 3.3. The thermal conductivity of CNT arrays and glass-CNT array contact conductance are measured using phase sensitive photo thermal reflectance thermometry. The heat conduction model for solving the phase function is described in equation (3.14) to equation (3.20). The $\phi_{\text{CNT array}}$ used to evaluate the volumetric heat capacity of the CNT array in equation (3.21) is $\sim 0.6\%$. The fitting parameters in the phase function are $k_{\text{CNT array}}$ and $G_{\text{In-CNT array}}$.

Table 4.4 shows the best fit solutions of $k_{\text{CNT array}}$ and $G_{\text{In-CNT array}}$. According to equation (4.8), $G_{\text{In-CNT array}}$ equals approximately to $G_{\text{Glass-CNT array}}$. Therefore, $G_{\text{Glass-CNT array}}$ and $k_{\text{CNT array}}$ are plotted as a function of compressive stress (see Figure 4.20) and the corresponding strain of the CNT array (see Figure 4.21) according to the best fit solutions listed in Table 4.4.

Table 4.4. The best fit solutions of $k_{CNT\ array}$, $G_{In-CNT\ array}$ corresponding to the compressive stress and strain of the CNT array.

| Stress (kPa) | Strain | $k_{CNT\ array}$ (W/m-K) | $G_{In-CNT\ array}$ (MW/m ² -K) |
|--------------|--------|--------------------------|--|
| 28 | 0.16 | 12±2 | 0.09±0.01 |
| 46 | 0.19 | 7±1 | 0.20±0.07 |
| 72 | 0.37 | 7±2 | 0.18±0.02 |
| 105 | 0.64 | 7±1 | 0.30±0.05 |
| 172 | 0.77 | 13 ±1 | 0.50±0.01 |
| 245 | 0.85 | 11±2 | 0.10±0.01 |
| 452 | 0.86 | 10±1 | 0.22±0.01 |
| 560 | 0.86 | 12±3 | 0.10±0.01 |

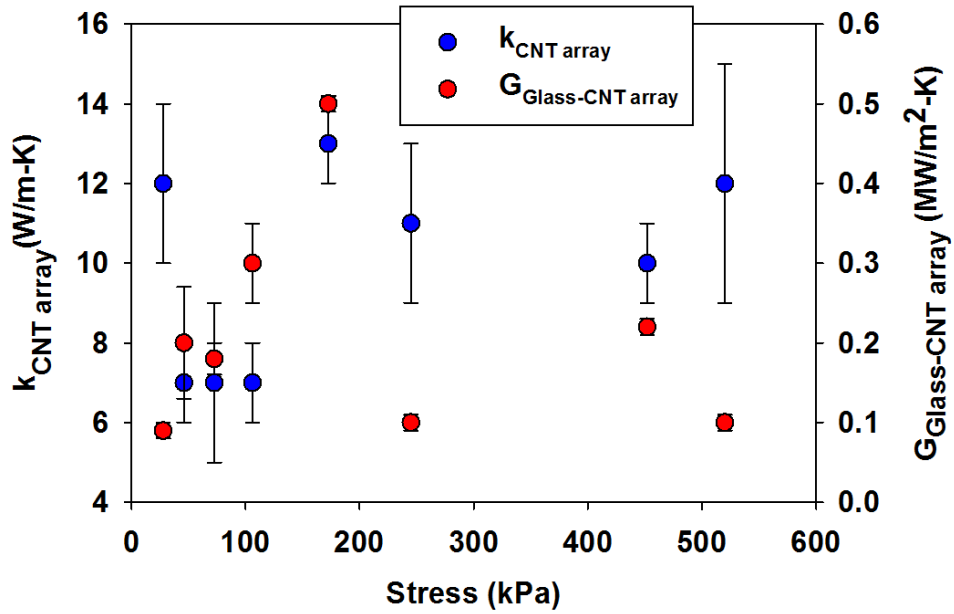


Figure 4.20. Thermal conductivity of CNT array and glass-CNT array contact conductance plotted as a function of applied compressive stress.

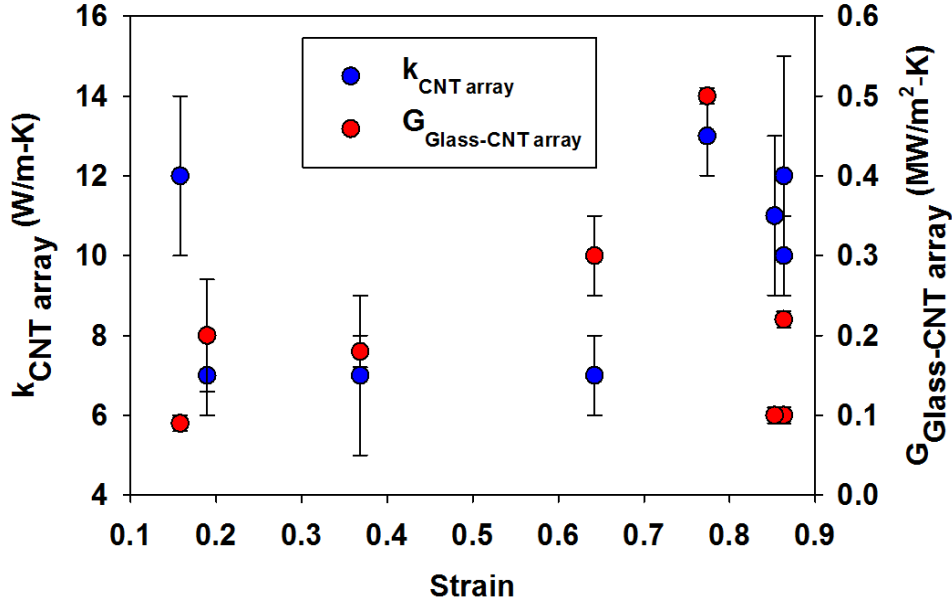


Figure 4.21. Thermal conductivity of CNT array and glass-CNT array contact conductance plotted as a function of strain of the CNT array.

$G_{In-CNT\ array}$ is 0.09 MW/m²-K at stress of 28 kPa. Divided by $G_{In-Graphite}$, $G_{In-CNT\ array}$ yields the area fraction of the tubes contacting to the In film, ϕ_{area} , at 0.09% with $G_{In-CNT\ array}$ of 0.09 MW/m²-K according equation (4.9). As mentioned in the earlier sections, a possible reason for lower ϕ_{area} comparing to $\phi_{CNT\ array}$ is that less than total number of the tubes in the CNT array is contacting to the target substrate. The low ϕ_{area} causes low $G_{In-CNT\ array}$. However, another reason for the low $G_{In-CNT\ array}$ could be the lower value of $G_{In-Graphite}$. To evaluate the possibility of low $G_{In-CNT\ array}$ caused by the two reasons, one should verify the intrinsic thermal conductivity of the individual tube. Since the CNT array is in vertically aligned region when the stress is at 28 kPa according to Figure 4.15(a), one can divide the corresponding $k_{CNT\ array}$, 12 W/m-K, by 0.09%, which yields k_{CNT} to be over 10000 W/m-K. The value of k_{CNT} is much higher than the reported data. This indicates that the over estimation of $G_{In-Graphite}$ is the possible reason for low $G_{In-CNT\ array}$. Therefore, ϕ_{area} is assumed to be the initial as-grown $\phi_{CNT\ array}$ throughout the whole range of compressive stress.

$G_{In-CNT\ array}$ increases monotonically from 0.09 MW/m²-K to 0.5 MW/m²-K as the compressive stress increases from 28 kPa to 172 kPa; the increasing trend is possibly due to the stronger bonding between CNT and In which increases $G_{In-Graphite}$. As the compressive stress further increases to 245 kPa-560 kPa, $G_{In-CNT\ array}$ decreases back to ~0.1 MW/m²-K, this shows that there could be fatigue failure between the bonding of CNT which decreases the $G_{In-Graphite}$.

$k_{CNT\ array}$ decreases from 12 W/m-K to 7 W/m-K as the stress increases from 28 kPa to 46 kPa. It is possible that at 46 kPa, the CNT array is buckled, and the thermal conductivity of the CNT array with buckling structure is expressed in equation (4.25). It is assumed that the area fraction of the CNT array contacting to the In film in equation (4.25) is approximately the initial volume fraction of the CNT array

$$\phi_{area} = \phi_{CNTarray}. \quad (4.26)$$

Equation (4.25) can now be expressed as

$$k_{CNTarray} \approx \frac{L_{film} k_{CNT} \phi_{CNTarray}}{L_{CNT}} + \frac{4L_{film} G_{Van_i} L_{CNT} \phi_{CNTarray}}{(2n-1)^2 d_{CNT}} \quad (4.27)$$

since

$$\frac{L_{film}}{L_{CNTarray}} = 1 - \varepsilon \quad (4.28)$$

where ε is the strain of CNT array, the final expression for the thermal conductivity of buckled CNT array is

$$k_{CNTarray} \approx (1 - \varepsilon) k_{CNT} \phi_{CNTarray} + \frac{4L_{film} G_{Van_i} L_{CNT} \phi_{CNTarray}}{(2n-1)^2 d_{CNT}} \quad (4.29)$$

In this work, $\phi_{CNTarray}$ is initially 0.6%. The intrinsic thermal conductivity of CNT can be calculated from the thermal conductivity of CNT array at stress of 28 kPa using equation (4.10) since the structure of the CNT array remains vertically aligned. k_{CNT} is \sim 2000 W/m-K with $k_{CNTarray}$ of 12 W/m-K and the $\phi_{CNTarray}$ of 0.6%. It is assumed that k_{CNT} stays the same throughout the whole range of compressive stress.

At stress of 46 kPa and strain of 0.19, the CNT array is buckled and its thermal conductivity is measured to be 7 ± 1 W/m-K. In this case, it is possible that the thermal conductivity of buckled CNT array contributed by G_{Van_i} is much smaller than the thermal conductivity contributed by k_{CNT} , so that

$$k_{CNTarray} \approx (1 - \varepsilon) k_{CNT} \phi_{CNTarray}. \quad (4.30)$$

$k_{CNTarray}$ is calculated to be ~ 9 Wm-K with ε of 0.19, k_{CNT} of 2000 W/m-K, and $\phi_{CNTarray}$ of 0.6% using equation (4.30). This value is close the measured value, 7 ± 1 W/m-K.

As stress increases from 105 kPa to 560 kPa and strain increases from 0.64 to 0.86, it is possible that the thermal conductivity of buckled CNT array contributed by G_{Van_i} becomes comparable or larger than the thermal conductivity contributed by k_{CNT} . Table 4.5 lists the thermal conductivity contributed by k_{CNT} ($k_{CNTarray_k}$) and the thermal conductivity contributed by G_{Van_i} ($k_{CNTarray_G}$) with the corresponding structure, strain (ε), $k_{CNTarray}$, number of packet (n), and G_{Van_i} . $k_{CNTarray}$ is the measured thermal conductivity of the CNT array, which is also the summation of $k_{CNTarray_k}$ and $k_{CNTarray_G}$

$$k_{CNTarray} = k_{CNTarray_k} + k_{CNTarray_G} \quad (4.31)$$

where k_{CNT_k} is calculated by

$$k_{CNTarray_k} = (1 - \varepsilon)k_{CNT}\phi_{CNTarray}. \quad (4.32)$$

Then $k_{CNTarray_G}$ is

$$k_{CNTarray_G} = k_{CNTarray} - k_{CNTarray_k}. \quad (4.33)$$

G_{Van_i} is calculated as

$$G_{Van_i} = \frac{(2n-1)^2 k_{CNTarray_G} d_{CNT}^2}{4L_{film}L_{CNT}\phi_{CNTarray}} \quad (4.34)$$

where $n=10$ according to the layer structured shown in Figure 4.15(e).

Table 4.5. $k_{CNTarray}$, $k_{CNTarray_k}$, $k_{CNTarray_G}$, and G_{Van_i} with the corresponding structure and strain of the CNT array.

| Structure | strain | $k_{CNTarray}$ (W/m-K) | $k_{CNTarray_k}$ (W/m-K) | $k_{CNTarray_G}$ (W/m-K) | n | G_{Van_i} (W/m ² -K) |
|--------------------|--------|---------------------------|------------------------------|------------------------------|-----|---------------------------------------|
| vertically aligned | 0.16 | 12 | 12.00 | negligible | | |
| buckled | 0.19 | 7 | 9.72 | negligible | 10 | |
| buckled | 0.37 | 7 | 7.56 | negligible | 10 | |
| buckled | 0.64 | 7 | 4.32 | 2.68 | 10 | 51682 |
| buckled | 0.77 | 13 | 2.76 | 10.24 | 10 | 197470 |
| buckled | 0.85 | 11 | 1.80 | 9.20 | 10 | 177415 |
| buckled | 0.86 | 10 | 1.68 | 8.32 | 10 | 160444 |
| buckled | 0.86 | 12 | 1.68 | 10.32 | 10 | 199013 |

Plotted as a function of strain (see Figure 4.22), $k_{CNTarray_k}$ has a decreasing trend as strain increases from ~0.19 to 0.86 while $k_{CNTarray_G}$ has an increasing trend as strain increases from 0.64 to 0.77. The increasing trend of $k_{CNTarray_G}$ is resulted from the increase of G_{Van_i} as the layered structure becomes more compact. It is interesting and comforting to note that the thermal conductivity of the buckled CNT array with fully compacted structure is close to the cross-plane thermal conductivity of graphite ~ 12 W/m-K. In summary, the summation of the two trend ($k_{CNTarray_G}$ and k_{CNT_k}) is close to the trend of the measured thermal conductivity of CNT array which indicates that the heat conduction model built by the thermal resistance net work explains well to the thermal transport in the buckled CNT array.

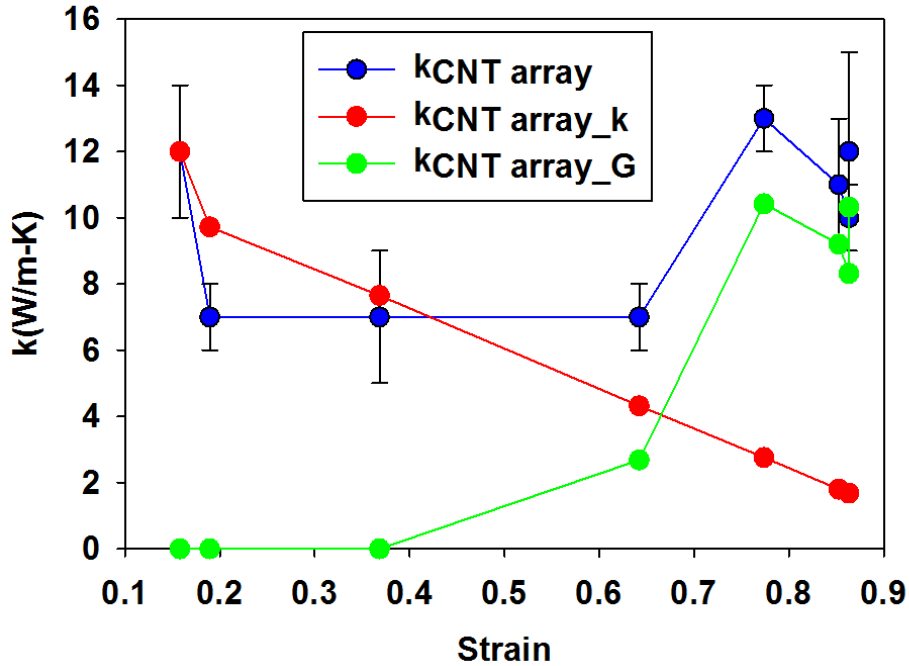


Figure 4.22. $k_{CNT\ array}$, $k_{CNT\ array_k}$, and $k_{CNT\ array_G}$ plotted as a function of strain of the CNT array.

4.5 Summary

In this chapter, the thermal transport properties of CNT arrays are measured as a function of various conditions under the precondition of In-assisted bonding between CNT array and target substrate.

The thermal contact conductance between a CNT array and a copper substrate becomes dependent on the copper surface roughness once the copper surface roughness becomes larger than the CNT array surface roughness, and the contact conductance has one order of magnitude drop. This provides a range for the surface roughness of target substrates when the CNT array surface roughness cannot be further decreased.

To ensure the performance of thermal contact conductance between the CNT array and target substrate, the CNT array is attached to an atomically flat glass substrate, and the thermal properties are measured as a function of the volume fraction of CNT array. Both the thermal contact conductance between the CNT array and glass substrate and the thermal conductivity of the CNT array increase monotonically as the volume fraction increases. The increase of the number of tube-glass contacts can potentially increase thermal contact conductance and the thermal conductivity. However, it has been quantitatively found that the increasing trend of the thermal conductivity is larger than the increasing trend of the volume fraction. The larger increasing trend of the thermal conductivity is due to the buckling of CNT array with lower volume fraction. The highest volume fraction CNT array is verified to be vertically aligned while the lowest volume fraction CNT array is verified to be buckled under the same nominal compressive stress. A heat conduction model is built based on the thermal resistance network to explain the decrease of CNT array thermal conductivity due to the buckling structure.

The thermal transport properties are measured as a function of the length of CNT array. The CNT array is kept at the highest volume fraction. The thermal conductivity of the CNT array and the thermal contact conductance between the CNT array and glass substrate are measured to be approximately independent of the length of the CNT array. The length-independent thermal conductivity is possible due to the vertically aligned structure of the CNT arrays after compression bonding. This indicates that, instead of the length, the volume fraction and the structure of CNT array are the key factors to determine the thermal transport properties of CNT array.

The structure and the strain of CNT arrays were examined systematically as a function of nominal compressive stress. The nominal buckling strength of the CNT array increases as the volume fraction of CNT array increases while the nominal buckling strength stays at constant as the length of CNT array increases.

Finally, the thermal transport properties of CNT arrays were measured as a function of nominal compressive stress and analyzed systematically as a function of the strain and the array structure. The thermal contact conductance between the CNT array and glass increases as the compressive stress increases from 28 kPa to 172 kPa and decreases by further increasing the compressive stress. The increasing trend of the contact conductance may be due to the stronger bonding between CNTs and In, while the decreasing trend could possibly due to the certain degree of failure at CNTs-In boundary. The CNT array thermal conductivity decreases once the structure of the CNT array is buckled; however, it gradually increases as the strain increases and as the structure becomes more compact. The rise of the CNT array thermal conductivity with buckling structure is due to the stronger bonding between the folded tubes as the distance between the tubes decreases. The heat conduction model based on the thermal resistance network (the resistance of tube and the resistance between the tubes) confirms the trend of the thermal conductivity of CNT array.

5 Conclusions and Future Works

In this work, the thermal transport and mechanical properties of CNT array are systematically examined. The CNT arrays were grown using water-assisted CVD synthesis. The CNT arrays were attached to the substrate using In-assisted thermal compression bonding. Phase sensitive photo thermal reflectance thermometry was used to measure the thermal properties of CNT array. The mechanical properties of CNT arrays were measured under compressive stress by considering the CNT array as a macroscopic film. A heat conduction model based on the thermal resistance network was demonstrated to explain the correlation between the thermal transport properties of the buckling behavior of CNT arrays.

The results presented here lead to the following conclusions: (1) The thermal contact conductance between the CNT array and copper substrate is dependent on the copper surface roughness when the surface roughness of copper becomes larger than the surface roughness of CNT array. (2) The thermal conductivity of a CNT array and the thermal contact conductance between a CNT array and glass increase monotonically as the CNT array volume fraction increases while stays approximately constant as the CNT array length varies. (3) The buckling strength of the CNT array is dependent on the volume fraction of CNT array while independent on the length of CNT array. (4) The thermal conductivity decreases due to the initial buckling of CNT array while gradually rises back by the thermal contact conductance between tubes resulted from the van der Waals interactions.

However, the above areas of works still have opportunities for continued research. In the area of CNT array synthesis, the volume fraction of a CNT array is controlled by the annealing time and H_2 flow rate prior to the CNTs growth while the length of CNT array is controlled by the exposure duration of C_2H_4 . The maximum volume fraction of a CNT array can only reach ~ 2% and the minimum length of the CNT array is ~ 65 μm . Since the length of CNT array is the geometry effect of the bulk resistance while the volume fraction of CNT array affects the intensive properties of CNT array, it is important to create a dense, short CNT array. Recent reports have shown that the CNT array can be densified to ~20%-70% using several methods: (1) apply compressive stress at the sides of CNT array;⁷⁷ (2) shrink the CNT array with solution;³² (3) cyclic deposit and anneal the iron catalyst film using CVD method to increase the catalyst particles which increases the tube density.⁷⁸ However, the length scale of these highly packed CNT array are all in the millimeter scale. It is possible that the length of CNT array may be cut down through engineering method such as, oxygen plasma etching. However, there are difficulties for controlling the length of CNT array through an etching method: (1) a change of morphology at the CNT array top surface, (2) a decrease in the uniformity of length. In future works, systematic length control on highly packed CNT array should be studied, in addition, it would be interesting to study the effect of the morphology and non-uniformity on the thermal transport properties of CNT array.

In the area of packaging, the CNT arrays were attached to the glass substrate through In-assisted thermal compression bonding. In future work, it would be interesting to study the thermal contact conductance between a CNT array and the target substrate with different bonding layers. For example, Au has much higher thermal conductivity than In, the heat transfer from Au to Au should be more efficient than the heat transfer from Au to In, which can potentially increase the thermal contact conductance.

References

- (1) Prasher, R. Thermal Interface Materials: Historical Perspective, Status, and Future Directions. *Proceedings of the IEEE* **2006**, *94*, 1571–1586.
- (2) Viswanath, R.; Wakharkar, V.; Watwe, A.; Lebonheur, V. Thermal Performance Challenges from Silicon to Systems. *Intel Technology Journal* **2000**, *Q3*, 1–16.
- (3) Cao, A.; Dickrell, P. L.; Sawyer, W. G.; Ghasemi-Nejhad, M. N.; Ajayan, P. M. Super-Compressible Foamlike Carbon Nanotube Films. *Science* **2005**, *310*, 1307–1310.
- (4) Zhao, Y.; Tong, T.; Delzeit, L.; Kashani, A.; Meyyappan, M.; Majumdar, A. Interfacial energy and strength of multiwalled-carbon-nanotube-based dry adhesive. *Journal of Vacuum Science & Technology B: Microelectronics and Nanometer Structures* **2006**, *24*, 331.
- (5) Qu, L.; Dai, L.; Stone, M.; Xia, Z.; Wang, Z. L. Carbon Nanotube Arrays with Strong Shear Binding-On and Easy Normal Lifting-Off. *Science* **2008**, *322*, 238–242.
- (6) Suhr, J.; Victor, P.; Ci, L.; Sreekala, S.; Zhang, X.; Nalamasu, O.; Ajayan, P. M. Fatigue resistance of aligned carbon nanotube arrays under cyclic compression. *Nature Nanotechnology* **2007**, *2*, 417–421.
- (7) Tong, T.; Zhao, Y.; Delzeit, L.; Kashani, A.; Meyyappan, M.; Majumdar, A. Height Independent Compressive Modulus of Vertically Aligned Carbon Nanotube Arrays. *Nano Lett.* **2008**, *8*, 511–515.
- (8) Berber, S.; Kwon, Y.-K.; Tománek, D. Unusually High Thermal Conductivity of Carbon Nanotubes. *Phys. Rev. Lett.* **2000**, *84*, 4613–4616.
- (9) Fujii, M.; Zhang, X.; Xie, H.; Ago, H.; Takahashi, K.; Ikuta, T.; Abe, H.; Shimizu, T. Measuring the Thermal Conductivity of a Single Carbon Nanotube. *Phys. Rev. Lett.* **2005**, *95*, 065502.
- (10) Pop, E.; Mann, D.; Wang, Q.; Goodson, K.; Dai, H. Thermal Conductance of an Individual Single-Wall Carbon Nanotube above Room Temperature. *Nano Lett.* **2005**, *6*, 96–100.
- (11) Kim, P.; Shi, L.; Majumdar, A.; McEuen, P. L. Thermal Transport Measurements of Individual Multiwalled Nanotubes. *Phys. Rev. Lett.* **2001**, *87*, 215502.
- (12) Hannemann, R. J. Thermal control of electronics: Perspectives and prospects. **2003**.
- (13) Xu, J.; Fisher, T. S. Enhancement of thermal interface materials with carbon nanotube arrays. *International Journal of Heat and Mass Transfer* **2006**, *49*, 1658–1666.
- (14) <http://www.intel.com/support/processors/pentium/sb/cs-011035.htm>.
- (15) Chiu, C.-P.; Maveety, J. G.; Tran, Q. A. Characterization of solder interfaces using laser flash metrology. *Microelectronics Reliability* **2002**, *42*, 93–100.
- (16) Iijima, S. Helical Microtubules of graphitic carbon. *Nature* **1991**, *354*, 56–58.
- (17) Salvetat, J. P.; Kulik, A. J.; Bonard, J. M.; Briggs, G. A. D.; Stöckli, T.; Méténier, K.; Bonnamy, S.; Béguin, F.; Burnham, N. A.; Forró, L. Elastic modulus of ordered and disordered multiwalled carbon nanotubes. *Advanced Materials* **1999**, *11*, 161–165.
- (18) Merkoçi, A. Carbon Nanotubes in Analytical Sciences. *Microchimica Acta* **2005**, *152*, 157–174.
- (19) Dai, H. Carbon Nanotubes: Synthesis, Integration, and Properties. *Acc. Chem. Res.* **2002**, *35*, 1035–1044.

- (20) Hata, K. Water-Assisted Highly Efficient Synthesis of Impurity-Free Single-Walled Carbon Nanotubes. *Science* **2004**, *306*, 1362–1364.
- (21) Futaba, D. N.; Hata, K.; Namai, T.; Yamada, T.; Mizuno, K.; Hayamizu, Y.; Yumura, M.; Iijima, S. 84% Catalyst Activity of Water-Assisted Growth of Single Walled Carbon Nanotube Forest Characterization by a Statistical and Macroscopic Approach. *J. Phys. Chem. B* **2006**, *110*, 8035–8038.
- (22) Nessim, G. D.; Hart, A. J.; Kim, J. S.; Acquaviva, D.; Oh, J.; Morgan, C. D.; Seita, M.; Leib, J. S.; Thompson, C. V. Tuning of Vertically-Aligned Carbon Nanotube Diameter and Areal Density through Catalyst Pre-Treatment. *Nano Lett.* **2008**, *8*, 3587–3593.
- (23) Overney, G.; Zhong, W.; Tomanek, D. Structural rigidity and low frequency vibrational modes of long carbon tubules. *Zeitschrift für Physik D Atoms, Molecules and Clusters* **1993**, *27*, 93–96.
- (24) Treacy, M. M. J.; Ebbesen, T. W.; Gibson, J. M. Exceptionally high Young's modulus observed for individual carbon nanotubes. *Nature* **1996**, *381*, 678–680.
- (25) Jensen, K.; Mickelson, W.; Kis, A.; Zettl, A. Buckling and kinking force measurements on individual multiwalled carbon nanotubes. *Phys. Rev. B* **2007**, *76*, 195436.
- (26) Rodney, S. R.; Tersoff, J.; Lorents, D. C.; Subramoney, S.; Chan, B. Radial deformation of carbon nanotubes by van der Waals forces. *Nature* **1993**, *364*.
- (27) Hertel, T.; Walkup, R. E.; Avouris, P. Deformation of carbon nanotubes by surface van der Waals forces. *Physical Review B* **1998**, *58*, 13–13.
- (28) Salvétat, J. P.; Briggs, G. A. D.; Bonard, J. M.; Bacsá, R. R.; Kulik, A. J.; Stöckli, T.; Burnham, N. A.; Forró, L. Elastic and shear moduli of single-walled carbon nanotube ropes. *Physical Review Letters* **1999**, *82*, 944–947.
- (29) Deck, C. P.; Flowers, J.; McKee, G. S. B.; Vecchio, K. Mechanical behavior of ultralong multiwalled carbon nanotube mats. *Journal of Applied Physics* **2007**, *101*, 023512–023512–9.
- (30) Zhang, Y. Q.; Liu, G. R.; Wang, J. S. Small-scale effects on buckling of multiwalled carbon nanotubes under axial compression. *Phys. Rev. B* **2004**, *70*, 205430.
- (31) Zbib, A. A.; Mesarovic, S. D.; Lilleodden, E. T.; McClain, D.; Jiao, J.; Bahr, D. F. The coordinated buckling of carbon nanotube turfs under uniform compression. *Nanotechnology* **2008**, *19*, 175704.
- (32) Zhang, L.; Zhang, G.; Liu, C.; Fan, S. High-Density Carbon Nanotube Buckypapers with Superior Transport and Mechanical Properties. *Nano Letters* **2012**, 120828101800001.
- (33) Dresselhaus, M. S.; Dresselhaus, G.; Eklund, P. C. Science of fullerenes and carbon nanotubes. *Academic Press* **1996**.
- (34) Hone, J.; Whitney, M.; Piskoti, C.; Zettl, A. Thermal conductivity of single-walled carbon nanotubes. *Phys. Rev. B* **1999**, *59*, R2514–R2516.
- (35) Yi, W.; Lu, L.; Dian-lin, Z.; Pan, Z. W.; Xie, S. S. Linear specific heat of carbon nanotubes. *Phys. Rev. B* **1999**, *59*, R9015–R9018.
- (36) Heremans, J.; Beetz, C. P. Thermal conductivity and thermopower of vapor-grown graphite fibers. *Phys. Rev. B* **1985**, *32*, 1981–1986.
- (37) Che, J.; Çagin, T.; Goddard, W. A. Thermal conductivity of carbon nanotubes. *Nanotechnology* **2000**, *11*, 65–69.
- (38) Osman, M. A.; Srivastava, D. Temperature dependence of the thermal conductivity of single-wall carbon nanotubes. *Nanotechnology* *12*, 21.

- (39) Choi, S. U. S.; Zhang, Z. G.; Yu, W.; Lockwood, F. E.; Grulke, E. A. Anomalous thermal conductivity enhancement in nanotube suspensions. *Applied Physics Letters* **2001**, *79*, 2252–2254.
- (40) Biercuk, M. J.; Llaguno, M. C.; Radosavljevic, M.; Hyun, J. K.; Johnson, A. T.; Fischer, J. E. Carbon nanotube composites for thermal management. *Applied Physics Letters* **2002**, *80*, 2767–2769.
- (41) Guthy, C.; Du, F.; Brand, S.; Winey, K. I.; Fischer, J. E. Thermal Conductivity of Single-Walled Carbon Nanotube/PMMA Nanocomposites. *J. Heat Transfer* **2007**, *129*, 1096–1099.
- (42) Bonnet, P.; Sireude, D.; Garnier, B.; Chauvet, O. Thermal properties and percolation in carbon nanotube-polymer composites. *Applied Physics Letters* **2007**, *91*, 201910–1–201910–3.
- (43) Gojny, F. H.; Wichmann, M. H. G.; Fiedler, B.; Kinloch, I. A.; Bauhofer, W.; Windle, A. H.; Schulte, K. Evaluation and identification of electrical and thermal conduction mechanisms in carbon nanotube/epoxy composites. *Polymer* **2006**, *47*, 2036–2045.
- (44) Prasher, R. S.; Hu, X. J.; Chalopin, Y.; Mingo, N.; Lofgreen, K.; Volz, S.; Cleri, F.; Keblinski, P. Turning Carbon Nanotubes from Exceptional Heat Conductors into Insulators. *Phys. Rev. Lett.* **2009**, *102*, 105901.
- (45) Huxtable, S. T.; Cahill, D. G.; Shenogin, S.; Xue, L.; Ozisik, R.; Barone, P.; Usrey, M.; Strano, M. S.; Siddons, G.; Shim, M.; Keblinski, P. Interfacial heat flow in carbon nanotube suspensions. *Nature Materials* **2003**, *2*, 731–734.
- (46) Marconnet, A. M.; Yamamoto, N.; Panzer, M. A.; Wardle, B. L.; Goodson, K. E. Thermal Conduction in Aligned Carbon Nanotube–Polymer Nanocomposites with High Packing Density. *ACS Nano* **2011**, *5*, 4818–4825.
- (47) Tong, T.; Zhao, Y.; Delzeit, L.; Kashani, A.; Meyyappan, M.; Majumdar, A. Dense Vertically Aligned Multiwalled Carbon Nanotube Arrays as Thermal Interface Materials. *IEEE Transactions on Components and Packaging Technologies* **2007**, *30*, 92–100.
- (48) Cola, B. A.; Xu, J.; Cheng, C.; Xu, X.; Fisher, T. S.; Hu, H. Photoacoustic characterization of carbon nanotube array thermal interfaces. *Journal of Applied Physics* **2007**, *101*, 054313–1–054313–9.
- (49) Panzer, M. A.; Zhang, G.; Mann, D.; Hu, X.; Pop, E.; Dai, H.; Goodson, K. E. Thermal Properties of Metal-Coated Vertically Aligned Single-Wall Nanotube Arrays. *J. Heat Transfer* **2008**, *130*, 052401–9.
- (50) Hone, J.; Llaguno, M. C.; Nemes, N. M.; Johnson, A. T.; Fischer, J. E.; Walters, D. A.; Casavant, M. J.; Schmidt, J.; Smalley, R. E. Electrical and thermal transport properties of magnetically aligned single wall carbon nanotube films. *Applied Physics Letters* **2000**, *77*, 666–668.
- (51) Yang, D. J.; Zhang, Q.; Chen, G.; Yoon, S. F.; Ahn, J.; Wang, S. G.; Zhou, Q.; Wang, Q.; Li, J. Q. Thermal conductivity of multiwalled carbon nanotubes. *Phys. Rev. B* **2002**, *66*, 165440.
- (52) Liu, X.; Zhang, Y.; Cassell, A. M.; Cruden, B. A. Implications of catalyst control for carbon nanotube based thermal interface materials. *Journal of Applied Physics* **2008**, *104*, 084310–084310–5.
- (53) Guo, T.; Nikolaev, P.; Thess, A.; Colbert, D. T.; Smalley, R. E. Catalytic growth of single-walled nanotubes by laser vaporization. *Chemical Physics Letters* **1995**, *243*, 49–54.

- (54) Jose Yacaman, M.; Miki Yoshida, M.; Rendon, L.; Santiesteban, J. G. Catalytic growth of carbon microtubules with fullerene structure. *Applied physics letters* **1993**, *62*, 202–204.
- (55) Journet, C.; Bernier, P. Production of carbon nanotubes. *Applied Physics A: Materials Science & Processing* **1998**, *67*, 1–9.
- (56) See, C. H.; Harris, A. T. A review of carbon nanotube synthesis via fluidized-bed chemical vapor deposition. *Industrial & engineering chemistry research* **2007**, *46*, 997–1012.
- (57) Zhu, W. Z.; Miser, D. E.; Chan, W. G.; Hajaligol, M. R. Characterization of multiwalled carbon nanotubes prepared by carbon arc cathode deposit. *Materials chemistry and physics* **2003**, *82*, 638–647.
- (58) Dupuis, A. The catalyst in the CCVD of carbon nanotubes—a review. *Progress in Materials Science* **2005**, *50*, 929–961.
- (59) Charlier, J.-C.; Iijima, S. Growth mechanisms of carbon nanotubes. *Top. Appl. Phys.* **2001**, *80*, 55–81.
- (60) Dai, H.; Rinzler, A. G.; Nikolaev, P.; Thess, A.; Colbert, D. T.; Smalley, R. E. Single-wall nanotubes produced by metal-catalyzed disproportionation of carbon monoxide. *Chemical Physics Letters* **1996**, *260*, 471–475.
- (61) Nikolaev, P.; Bronikowski, M. J.; Bradley, R. K.; Rohmund, F.; Colbert, D. T.; Smith, K. A.; Smalley, R. E. Gas-phase catalytic growth of single-walled carbon nanotubes from carbon monoxide. *Chemical physics letters* **1999**, *313*, 91–97.
- (62) Vinciguerra, V.; Buonocore, F.; Panzera, G.; Occhipinti, L. Growth mechanisms in chemical vapour deposited carbon nanotubes. *Nanotechnology* **2003**, *14*, 655.
- (63) Hofmann, S.; Cantoro, M.; Kleinsorge, B.; Casiraghi, C.; Parvez, A.; Robertson, J.; Ducati, C. Effects of catalyst film thickness on plasma-enhanced carbon nanotube growth. *Journal of applied physics* **2005**, *98*, 034308–034308.
- (64) Yamada, T.; Namai, T.; Hata, K.; Futaba, D. N.; Mizuno, K.; Fan, J.; Yudasaka, M.; Yumura, M.; Iijima, S. Size-selective growth of double-walled carbon nanotube forests from engineered iron catalysts. *Nature nanotechnology* **2006**, *1*, 131–136.
- (65) Amama, P. B.; Pint, C. L.; McJilton, L.; Kim, S. M.; Stach, E. A.; Murray, P. T.; Hauge, R. H.; Maruyama, B. Role of water in super growth of single-walled carbon nanotube carpets. *Nano Letters* **2008**, *9*, 44–49.
- (66) Ghosh, A. P.; Gerenser, L. J.; Jarman, C. M.; Fornalik, J. E. Thin-film encapsulation of organic light-emitting devices. *Applied Physics Letters* **2005**, *86*, 223503–223503–3.
- (67) Lu, Q.; Keskar, G.; Ciocan, R.; Rao, R.; Mathur, R. B.; Rao, A. M.; Larcom, L. L. Determination of Carbon Nanotube Density by Gradient Sedimentation. *J. Phys. Chem. B* **2006**, *110*, 24371–24376.
- (68) Tong, X. C. *Advanced Materials for Thermal Management of Electronic Packaging*; Springer, 2011.
- (69) Hu, X. J.; Panzer, M. A.; Goodson, K. E. Infrared Microscopy Thermal Characterization of Opposing Carbon Nanotube Arrays. *Journal of Heat Transfer* **2007**, *129*, 91.
- (70) Ujihara, K. Reflectivity of Metals at High Temperatures. *Journal of Applied Physics* **1972**, *43*, 2376–2383.
- (71) Incropera, F. P.; De Witt, D. P. Fundamentals of heat and mass transfer. **1985**.
- (72) Ohsone, Y.; Wu, G.; Dryden, J.; Zok, F.; Majumdar, A. Optical Measurement of Thermal Contact Conductance Between Wafer-Like Thin Solid Samples. *J. Heat Transfer* **1999**, *121*, 954–963.

- (73) Gundrum, B. C.; Cahill, D. G.; Averback, R. S. Thermal conductance of metal-metal interfaces. *Phys. Rev. B* **2005**, *72*, 245426.
- (74) Mizel, A.; Benedict, L. X.; Cohen, M. L.; Louie, S. G.; Zettl, A.; Budraa, N. K.; Beyermann, W. P. Analysis of the low-temperature specific heat of multiwalled carbon nanotubes and carbon nanotube ropes. *Phys. Rev. B* **1999**, *60*, 3264–3270.
- (75) Chang, C. W.; Okawa, D.; Garcia, H.; Majumdar, A.; Zettl, A. Nanotube Phonon Waveguide. *Phys. Rev. Lett.* **2007**, *99*, 045901.
- (76) Zhong, H.; Lukes, J. R. Interfacial thermal resistance between carbon nanotubes: Molecular dynamics simulations and analytical thermal modeling. *Physical Review B* **2006**, *74*, 125403.
- (77) Wardle, B. L.; Saito, D. S.; García, E. J.; Hart, A. J.; De Villoria, R. G.; Verploegen, E. A. Fabrication and Characterization of Ultrahigh-Volume-Fraction Aligned Carbon Nanotube–Polymer Composites. *Advanced Materials* **2008**, *20*, 2707–2714.
- (78) Esconjauregui, S.; Fouquet, M.; Bayer, B. C.; Ducati, C.; Smajda, R.; Hofmann, S.; Robertson, J. Growth of Ultrahigh Density Vertically Aligned Carbon Nanotube Forests for Interconnects. *ACS Nano* **2010**, *4*, 7431–7436.

Appendix A Temperature Field Derivation

The governing equation of one-dimensional three-layered transient heat conduction model is

$$\frac{\partial T_j(z_j, t)}{\partial t} = \frac{k_j}{C_j} \frac{\partial^2 T_j(z_j, t)}{\partial z_j^2} \quad (\text{A.1})$$

where j indicates 1st, 2nd, or 3rd layer. The boundary conditions are

$$-k_1 \left. \frac{\partial T_1}{\partial z_1} \right|_{z_1=0} = G_{1-2} (T_2(0, t) - T_1(0, t)) \quad (\text{A.2})$$

$$q'' \exp(-i\omega t) = -k_2 \left. \frac{\partial T_2}{\partial z_2} \right|_{z_2=0} + G_{1-2} (T_2(0, t) - T_1(0, t)) \quad (\text{A.3})$$

$$-k_2 \left. \frac{\partial T_2}{\partial z_2} \right|_{z_2=b_2} = G_{2-3} (T_2(b_2, t) - T_3(0, t)) = -k_3 \left. \frac{\partial T_3}{\partial z_3} \right|_{z_3=0} \quad (\text{A.4})$$

$$\left. \frac{\partial T_1}{\partial z_1} \right|_{z_1=b_1} = 0; \quad \left. \frac{\partial T_3}{\partial z_3} \right|_{z_3=b_3} = 0. \quad (\text{A.5})$$

Let $V_j(z_j, s)$ be the Laplace transform of $T_j(z_j, t)$, the Laplace transform of equation (A.1) is

$$\int_{t=0}^{t=\infty} \frac{\partial}{\partial t} T_j e^{-st} dt = \frac{k_j}{C_j} \frac{\partial^2}{\partial z_j^2} \int_{t=0}^{t=\infty} T_j e^{-st} dt \quad (\text{A.6})$$

where

$$\frac{k_j}{C_j} = \alpha_j, \quad (\text{A.7})$$

and α_j is the thermal diffusivity of j^{th} layer. Combining equation (A.7) and (A.6) yields

$$\frac{\partial^2 V_j}{\partial z_j^2} - \frac{s}{\alpha_j} V_j = 0. \quad (\text{A.8})$$

The general solution for the Laplace transform of temperature field is

$$V_j = A_j \cos h(\eta_j z_j) + B_j \sinh(\eta_j z_j) \quad (\text{A.9})$$

where

$$\eta_j = \sqrt{\frac{s}{\alpha_j}}. \quad (\text{A.10})$$

The Laplace transform of the boundary conditions (equation (A.2) to equation (A.5)) are

$$-k_1 \left. \frac{\partial V_1}{\partial z_1} \right|_{z_1=0} = G_{1-2}(V_2(0) - V_1(0)) \quad (\text{A.11})$$

$$\frac{\ddot{q}}{(s + i\omega)} = -k_2 \left. \frac{\partial V_2}{\partial z_2} \right|_{z_2=0} + G_{1-2}(V_2(0) - V_1(0)) \quad (\text{A.12})$$

$$-k_2 \left. \frac{\partial V_2}{\partial z_2} \right|_{z_2=b_2} = G_{2-3}(V_2(b_2) - V_3(0)) \quad (\text{A.13})$$

$$G_{2-3}(V_2(b_2) - V_3(0)) = -k_3 \left. \frac{\partial V_3}{\partial z_3} \right|_{z_3=0} \quad (\text{A.14})$$

$$\left. \frac{\partial V_1}{\partial z_1} \right|_{z_1=b_1} = 0; \quad \left. \frac{\partial V_3}{\partial z_3} \right|_{z_3=b_3} = 0 \quad (\text{A.15})$$

To satisfy boundary condition (A.15), the general solution of V_1 , and V_3 become

$$V_1 = A_1 \cos h(\eta_1(b_1 - z_1)) \quad (\text{A.16})$$

$$V_3 = A_3 \cos h(\eta_3(b_3 - z_3)). \quad (\text{A.17})$$

The general solution of V_2 is kept at

$$V_2 = A_2 \cos h(\eta_2 z_2) + B_2 \sinh(\eta_2 z_2). \quad (\text{A.18})$$

Combining equation (A.16), (A.18) and equation (A.11), (A.14) yields

$$(G_{1-2}C_1 + k_1\eta_1S_1)A_1 - G_{1-2}A_2 = 0 \quad (\text{A.19})$$

$$-G_{1-2}C_1A_1+G_{1-2}A_2-k_2\eta_2B_2=\frac{q''}{s+i\omega} \quad (\text{A.20})$$

$$-G_{2-3}C_3A_3+(G_{2-3}+k_2\eta_2S_2)A_2+k_2\eta_2C_2B_2=0 \quad (\text{A.21})$$

$$(-G_{2-3}C_3-k_3\eta_3S_3)A_3+G_{2-3}A_2=0 \quad (\text{A.22})$$

Where

$$C_j = \cosh(\eta_j b_j) \quad (\text{A.23})$$

$$S_j = \sinh(\eta_j b_j). \quad (\text{A.24})$$

The coefficient A_1, A_2, B_2, A_3 can be solved from equation (A.19) to (A.22). The solution for $V_2(0)$ is

$$V_2(0) = A_2, \quad (\text{A.25})$$

and

$$A_2 = \frac{q''}{s+i\omega} (G_{1-2}C_1+k_1\eta_1S_1)C_2(G_{2-3}C_3+k_3\eta_3S_3)\xi(s) \quad (\text{A.26})$$

Where

$$\xi(s) = (G_{1-2}k_2\eta_2S_2C_1G_{2-3}C_3+G_{1-2}G_{2-3}C_1k_3\eta_3S_3+G_{1-2}C_2k_1\eta_1S_1G_{2-3}C_3+h_1C_2k_1\eta_1S_1k_3\eta_3S_3+G_{1-2}k_2\eta_2S_2C_1k_3\eta_3S_3+k_2\eta_2S_2k_1\eta_1S_1G_{2-3}C_3+G_{2-3}k_1\eta_1S_1k_3\eta_3S_3+k_2\eta_2S_2k_1\eta_1S_1k_3\eta_3S_3)$$

$T_2(0,t)$ can be calculated using inverse of Laplace transform of $V_2(0)$

$$T_2(0,t) = q'' e^{-i\omega t} (G_{1-2}C_1+k_1\eta_1S_1)C_2(G_{2-3}C_3+k_3\eta_3S_3)\xi(s) \Big|_{s=-i\omega} \quad (\text{A.27})$$

Appendix B Load Cell Calibration

As shown in Figure B.1, the power supply applies DC voltage to the load cell, as load cell is applied with compressive stress, which causes strain in the load cell, the electrical resistance of load cell change. The change of resistance causes change of output voltage. To find out the correlation between output voltage and applied force, one can apply different weights with known mass on top of the load cell (see Figure B.2) and plot the output voltage as a function of loading (see Figure B.3). The output voltage linearly increases as a function loads with slope of $0.4 \mu\text{V/g}$.



Figure B.1. Image of power supply and voltmeter.

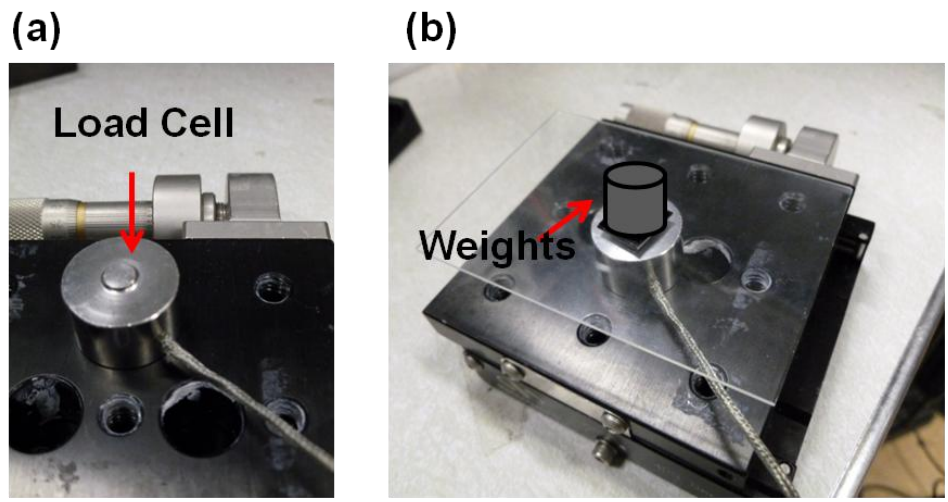


Figure B.2. Image of (a) a load cell and (b) weights on top of the load cell.

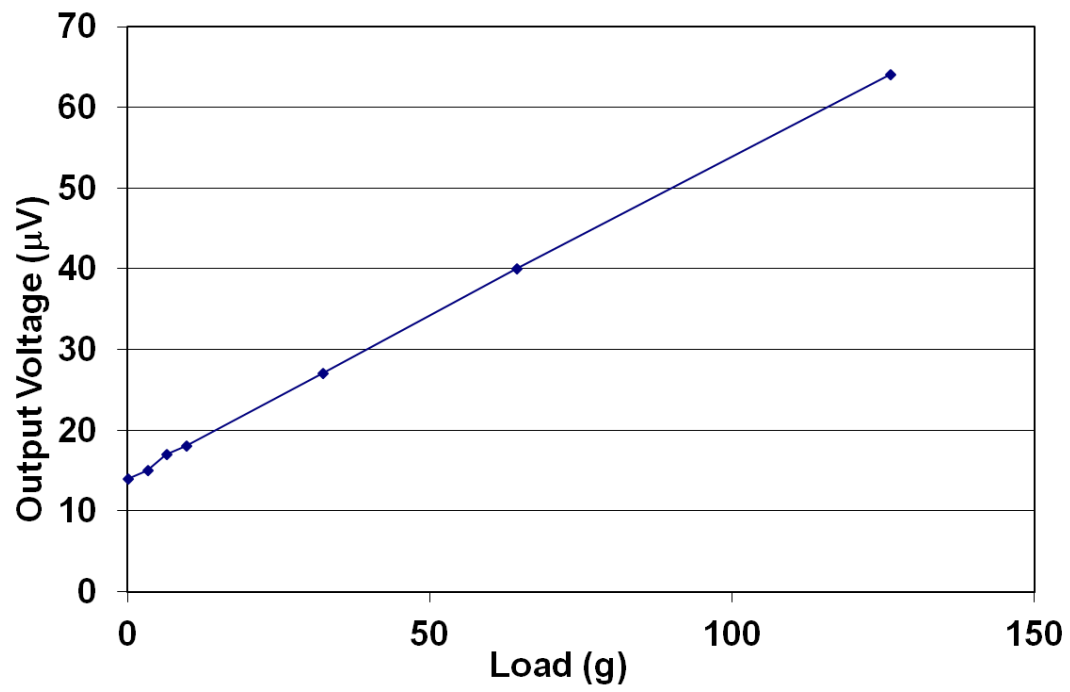


Figure B.3. Output voltage plotted as a function of load.